ROBUST CONTROL OF FLEXIBLE STRUCTURES: THEORY AND EXPERIMENTS

Thesis by

Gary John Balas

In Partial Fulfillment of the Requirements
for the Degree of
Doctor of Philosophy

California Institute of Technology
Pasadena, California

1990

(Submitted November 30, 1989)

To My Parents

Acknowledgements

I would like to thank my advisor and friend, John Doyle, for his enthusiasm and guidance in this research. He has great insight into the application and future direction of control theory and helped keep my research at the cutting edge. He provided me with freedom and support to pursue my own research ideas. My education has been enhanced because of him. I would like to thank the late Charles Babcock, my first advisor, for providing a role model with impeccable morals and standards which I strive to emulate. He encouraged me to think before leaping and to set my expectations high. I sorely miss him. My education would not be complete without the influence of Andy Packard. We spent countless hours discussing control theory, experiments, careers, business and relationships. His work ethic and pursuit of knowledge is unmatchable. He is a friend and collegue I greatly admire.

Many people have influenced and contributed to my broad education through my years at Caltech. I thank Manfred Morari for his constructive comments on my research and his friendship, Tom Caughey for opening my eyes to the field of dynamics, and Wolfgang Knauss for putting up with me and making my tenure in the aeronautics department a very enjoyable one. Roy Smith and Lane Dailey helped round out my eduation with their support and friendship. No less important are Kemin Zhou, Bobby Bodenheimer, Harold Stalfors, Al Moser and Matt Newlin. I would also like to thank the solid mechanics group, too numerous to mention by name, for the variety of issues discussed at the weekly Wednesday luncheons. My stay at Caltech was greatly enhanced by their friendship and the friendship of Paul and Linda Nowak, whom I met my first day on campus. Many a fowl has given their life for our dinners together.

Thanks are in order for the people who kept me sane and put my research into a real world perspective. The group at Le Studio, Chip, Phip, Cindy, Patrick, and many others, who made me realize that I should stay in school since a ballet career was out of the question. I appreciate the close friends, Janet, Aleta and Mellisa, who tolerated my complaining and warped sense of humor. To my old friends, Phil, Randy and Joe, thanks for still being my old friends. I thank all who entered and left my life in the past years; it's been a wonderful growing experience.

Abstract

Stringent requirements envisioned for the pointing and shape accuracy of future space missions necessitate advances in the control of large flexible structures. These structures will be extremely flexible, with little natural damping and modes densely packed throughout the frequency domain. Due to their size and complexity, testing of these structures will lead to system models that are inaccurate for control purposes. Therefore, control design methods must be developed to account for model inaccuracies or *uncertainties*. Such methods should optimize the robustness and performance characteristics of control laws based on the accuracy of the design model.

This thesis focuses on incorporating knowledge of the mismatch between the physical system and its mathematical models into the control design process. Control design models are developed to fit into the structured singular value (μ) framework that is used in the analysis and synthesis of control laws. To validate and verify theoretical developments, a flexible structure experiment is developed to investigate large flexible control problems in a laboratory environment. The Caltech experiment has a number of their attributes: closely spaced, lightly damped modes, collocated and noncollocated sensors and actuators combined with numerous modes in the controller crossover (roll off) region.

The experimental structure is used to investigate several important issues related to control of flexible structures: tradeoffs between robustness and performance associated with uncertainty modeling for flexible structures, robust control of flexible modes in the controller crossover region and benefits and limitations of collocated versus noncollocated control design. A consistent trend in the results indicates that an accurate description of the flexible structure <u>and</u> model errors is required to synthesize high performance, robust control laws for flexible structures.

Contents

List of Figures

List of Tables

Chapter 1

Introduction

Stringent requirements envisioned for the pointing and shape accuracy of future space missions necessitate advances in the control of large flexible structures. These structures will be extremely flexible, with little natural damping and modes densely packed throughout the frequency domain. Due to their size and complexity, ground testing of these structures in earth's environment will lead to system models that are inaccurate for operation in a zero-g environment. Even with on-orbit identification of the structure, discrepancies between their mathematical models and the "real" structure would still exist, though to a lesser extent. Therefore, control design methods must be developed to account for model inaccuracies or *uncertainties.* Such methods should optimize the robustness and performance characteristics of control laws based on the accuracy of the design model.

Robust control design methods optimize control laws based on knowledge of how model error enters into the problem description. Optimization is based on the mathematical system descriptions; therefore, accurate accounting and characterization of the variations between "real" flexible structures and their mathematical models is essential. Such variations are due to non-physically based assumptions, including neglected nonlinearities, unmodeled dynamics and errors associated with model parameters (e.g. mode shapes, natural frequencies, and damping values). The differences due to the first two assumptions can generally be approximated as a bounded-frequency domain error (referred to as *unstructured* uncertainty) when the nonlinearities are small. As the nonlinearities become more dominant, frequency domain descriptions of the nonlinearities is a poor modeling method, and more intelligent means need to be employed. The variations in the natural frequencies, damping values and mode shapes can be handled more systematically. These errors are highly *structured* and often cannot be treated as norm-bounded uncertainties without substantially increasing the conservativeness of the models. The additional conservativeness can severely limit the performance of the control design. Variation in the model parameters is defined as *parametric* uncertainty. The combination of unstructured and parametric uncertainty leads to *structured* uncertainty in the problem formulation. Similarly, uncertainty that is unstructured at the component level results in structured, though not parametric, uncertainty when viewed at the system level. Mathematical models of structured and unstructured uncertainties need to be included in the control problem formulation to optimize performance objectives.

This research focuses on incorporating knowledge of the mismatch between the physical system and its mathematical models into the control design process. Control design models of flexible structures are developed to fit into the structured singular value (μ) framework, used in the analysis and synthesis of control laws. The design model is based on a nominal or base plant model, uncertainty descriptions, and additive noise models. It defines a family or set of uncertain plant models in which the "real" structure is assumed to reside. μ-synthesis methods are applied to the model sets to generate control laws for the flexible structure. Since the "real" structure is assumed to lie inside the model set, measures of robustness and performance characteristics of the control laws can be evaluated and predicted when implemented on the "real" flexible structure.

μ-synthesis techniques for control design and analysis were first applied to a truss structure at TRW to determine their applicability to flexible structures [BalLDD, DailLuk1]. The TRW truss is a single-story structure whose top platform is supported by four vertical longerons. It has four voice-coil actuators placed along the diagonals, which are used for control, two actuators on the top platform used for disturbance and four displacement sensors on the top platform. The first 3 modes to be controlled are at approximately 1 Hz (two bending, one torsional) with the next set of modes at 18 Hz. The performance objective is to reduce the root mean square (RMS) response of the structure, as measured by the sensors, due to a band limited noise disturbance, and subject to constraints on the control actuator force levels.

A high fidelity mathematical model of the 4-input/4-output system was provided by TRW engineers for control design. Actuator and additive uncertainty models were developed to account for the mode shape variations and the flexible modes not included in the model. Control laws based on these models were designed with μ-synthesis methods, that attenuated the RMS response of the structure by a factor of 37:1. Control laws which attained higher performance were synthesized using additional information about the effects of the input disturbances on the system response. These attenuated the RMS sensor response by 48:1. The highest performance achieved by the TRW engineers using the characteristic loci methods was 28:1 [BalLDD, LukTun, DailLuk2].

The results obtained on the TRW truss structure confirmed the applicability of the μ-framework to control design for flexible structures. The knowledge gained from this experiment is used to design a flexible structure experiment at Caltech. The objective for the Caltech structure is to develop an experiment that exhibits large space structure (LSS) characteristics in a laboratory environment to investigate LSS control problems. The Caltech experiment has a number of their attributes: closely spaced, lightly damped modes, collocated and noncollocated sensors and actuators, and numerous modes in the controller crossover (roll off) region. The initial experimental structure (phase I design), consists of two stories, three longerons (columns) and three noncollocated sensors and actuators. The actuators are voice-coil type devices that output force along the diagonal members of the structure. The sensors are accelerometers, placed on the second platform. The structure has six flexible modes between 1.2 and 4.5 Hz, with the first group of local modes between 37 and 42 Hz. The phase II design incorporates a third story and additional actuators and sensors. The new actuators, mounted on the third story, are proof mass types that apply inertial forces to the structure by moving masses. Three accelerometers are placed on the second story and three are collocated with the proof mass actuators on the third story. The phase II structure has nine flexible modes between 0.90 and 6.3 Hz. These experiments are used to investigate several important issues related to control of flexible structures: tradeoffs associated with uncertainty modeling of flexible structures, robust control of flexible modes in the controller crossover region, and the design of noncollocated versus collocated control laws.

Motivation for the research has been touched on in this introduction. The first chapters provide background on control design issues for flexible structures and the methods employed in this research. Chapter 2 is a background on control design for flexible structures. It addresses important issues in this research, past research and current research in the field. Chapter 3 is an overview of the μ-analysis and synthesis techniques including information on H_∞ control design methods. Chapter 4 details the phase I and II flexible structure experiments developed at Caltech. Information on the actuators (voice coil, air and proof mass) and sensors (accelerometers, and linear voltage displacement transducers) is presented along with a finite element analysis of the structures. System identification techniques, used to develop a more accurate model of the flexible structure experiment, are presented in chapter 5. Chapter 6 motivates the need for uncertainty modeling n the description of physical systems and develops applicable uncertainty descriptions for flexible structures. Chapters 7, 8, and 9 detail theoretical and experimental results of the application of μ-techniques to the Caltech flexible structure. Chapter 7 investigates the tradeoffs associated with uncertainty modeling for flexible structures. Section 8 addresses design of control laws that cross over in a region of numerous, lightly damped modes, and chapter 9 examines the limitations associated with noncollocated sensors and actuators as compared with collocated control laws. A summary of results is presented in chapter 10 and a discussion of future research directions is offered.

Chapter 2

Background on Flexible Structures

Many of the proposed future space missions are advanced, complex experiments which require large structures for support. Strength requirements for these missions are minimal due to their operation in a zero-g environment. Limitations on the structural design are therefore dictated by launch loads and control systems requirements. The high cost associated with placing payloads into space puts a premium on weight and size. This combination leads to extremely flexible, large structures. Performance requirements associated with these missions necessitate control of a number of closely spaced, lightly damped structural modes whose characteristics will be poorly known. A major focus of the spacecraft control systems is on attenuation of vibration from on-board disturbances due to cryogenic coolers, repositioning of the spacecraft, docking, and crew movements.

Verification and refinement of models for spacecraft has always required pre-launch testing. However, testing of large space structures, designed for operation in zero-g, will present many difficulties in earth's environment. A complex suspension system is required to off load the effects of gravity on the structure and its joints. The suspension system will interact with the dynamics of the spacecraft, further complicating the system identification. This leads to errors in identification of natural frequencies, mode shapes and damping of the structure, which is compounded by the operation of the joints. The stringent pointing requirements associated with the mission's objectives dictate a high bandwidth control system requiring a number of flexible modes to be controlled. The performance objective combined with the limitations of modeling lead to a difficult control design problem.

There are many difficulties in the control design process inherent in large space structures. LSS are represented in mathematical terms via models that have a number of assumptions based on a linear behavior. Often, in spite of the fact that the structural engineer knows these assumptions to be highly idealized, the finite element method is used to develop linear, time-invariant, second-order models with classical damping. These models are mathematically easy to work with but do not represent the actual structure. Besides non-physically based assumptions and neglected nonlinearities, the model is inaccurate due to the errors in parameters used in the finite element description, leading to further errors in the natural frequencies and mode shapes. Damping coefficients for the subsequent control design model are poorly modeled or guessed at. The structural engineer truncates this "high fidelity" finite element model and provides the control designer with a state space representation describing the natural frequencies, damping values, and modal coefficients of the system. These known and unknown limitations of the model need to be accounted for by the control designer to achieve the performance objectives of the mission without destabilizing the system.

LSS will have numerous sensors with a limited number of actuators on board. Actuator and sensor placement is often dictated by structural or packaging requirements rather than performance objectives. These performance objectives include attenuating vibration of the entire spacecraft combined with tighter specifications on select points of the structure critical to the mission. Ideally, sensors would be located at points critical to the mission objectives. The actuators are either collocated with the sensors or due to other requirements on the spacecraft, noncollocated. The noncollocation of the actuators and sensors lead to performance limitations on the control system and introduces potential stability problems.

Performance requirements for these large flexible spacecraft include tight control of the position and vibration at extremity points on the structure. Position or vibration can be measured very accurately (e.g. with optical sensors or accelerometers) at these the points. However, it's impossible or structurally infeasible to mount actuators at each location. The difficulty of the design is further compounded by variations in the physical parameters over the life of the space mission.

The most common approaches to active vibration suppression include: direct output feedback, linear quadratic Gaussian (LQG) optimal control, LQG with loop transfer recovery (LQG/LTR), positivity, Maximum Entropy/Optimal Projection (MEOP), pole placement, and eigenvalue/eigenvector assignments. A brief discussion of LSS control problems follows.

2.1 Control System

A large body of research has addressed aspects of control design unique to the large space structures control problem. The structural characteristics of the LSS are dictated by the dynamic response at prescribed locations in the structure to applied torques and forces [NurRSS]. The "real" structure is often described by a mathematical model based on a finite element model of the form (neglecting damping)

$$M\ddot{q} + Kq = R \quad \rightarrow \quad M\ddot{q} + Kq = B'u \tag{2.1}$$

where q is an n-dimensional vector of generalized element displacements, u is an l-dimensional vector of actuators, R is the generalized force vector, B' is the $n \times l$ actuator influence coefficient matrix u, and M and K are $n \times n$ symmetric mass and stiffness matrices, respectively. A similarity transformation is performed, such that (2.1) is written as

$$I\ddot{\eta} + \Omega^2\eta = \Phi R \tag{2.2}$$

where Φ is an $n \times n$ matrix whose columns are the structural mode shapes and Ω is an $n \times n$ diagonal matrix of natural frequencies. Equation (2.2) can be written in a state space form by defining $x = (\eta, \dot{\eta})^T$

$$\dot{x} = Ax + Bu + B_d v \tag{2.3}$$

with

$$A = \begin{pmatrix} 0 & I \\ -\Omega^2 & 0 \end{pmatrix} \qquad B = \begin{pmatrix} 0 \\ \Phi B' \end{pmatrix} \tag{2.4}$$

where v is a disturbance vector and B_d is the influence coefficients of the disturbances. The measurements of the system are taken at a finite number of position, velocity, or acceleration sensors. The measurement vector y is given by

$$y = Cx + Du + v_m \tag{2.5}$$

where y is an $r \times l$ vector, C is $r \times n$, D is $r \times l$ and v_m is the measurement noise. In the implementation of control laws there are often dynamics associated with the sensors and actuators which need to be included in the design model. The noise levels can have spectral content that is accounted for via coloring filters on the set of input signals. The design problem is to synthesize a control law that achieves the performance objectives and does not destabilize the structure.

2.1.1 Collocated Rate Feedback

In the collocated case, the sensors and actuators are located at m select points on the structure. Taking into account a scaling factor, α, these components have identical influence or sensitivity coefficients. In the state space model, this is equivalent to the B_i components being scalar multiples of C_i. Ignoring disturbances, measurement noise, and reference signals:

$$B_i = \sum_{k=1}^{m} b_{ik} u_k(t) \quad i = 1, 2, \ldots, n \tag{2.6}$$

$$y_k = \sum_{i=1}^{n} \alpha_i b_{ki} \dot{\eta}_i(t) = \sum_{i=1}^{n} c_{ik} \dot{\eta}_i(t) \quad k = 1, 2, \ldots, m \tag{2.7}$$

with the outputs taken to be rate or velocity quantities at the k^{th} location. Equivalently, displacement or acceleration quantities could be defined but desirable properties of rate feedback would disappear. A transfer function representation of the structure is

$$y(s) = G(s)u(s) \tag{2.8}$$

$$G(s) \doteq \sum_{i=1}^{n} b_i b_i^T g_i(s), \qquad g_i(s) = \frac{s}{s^2 + 2\zeta_i \omega_i s + \omega_i^2} \tag{2.9}$$

with y, u, and b_i as described previously. An advantageous property of rate feedback is that the transfer function $G(s)$ is confined to the right half plane in the Nyquist plot, or equivalently the phase angle associated with this transfer function is confined to the range $-\frac{\pi}{2} \leq \phi \leq \frac{\pi}{2}$ for all frequencies.

A common approach to vibration attenuation is to feedback the measured rate information y to inputs u using a negative definite symmetric gain matrix

$$K = -V diag(\xi_i) V^T \tag{2.10}$$

thereby augmenting the damping in the structure [BalMJ1, BalMJ2, SteinG]. Ignoring rigid body modes and assuming all other modes are observable and controllable from a given collocated actuator/sensor pair, this feedback scheme is stable for all choices of $VV^T > 0$ and $\xi_i > 0, \; i = 1, ..., m$. This is similar to the addition of damping to each mode of the structure. The inclusion in the analysis of finite bandwidth actuators and sensors, time delays, and unmodeled dynamics requires the designer to roll off the control law to gain stabilize high frequency modes of the structure.

Collocated feedback provides a straightforward means for attenuating vibration at the point of collocation. The control laws are designed as single-input/single-output (SISO) and exhibit nice robustness properties. The main limitation is that often it is not possible to locate sensor/actuator pairs at all positions on the structure with performance requirements. There are also no performance improvement guarantees associated with locations without sensor/actuator pairs. Design methods applicable to noncollocated control are often required to achieve all the performance objectives.

2.1.2 LQG, LQG/LTR, and Pole Placement Control Design Methods

Numerous approaches have been proposed to design control laws for the noncollocated, multivariable active vibration attenuation problem. These methods include: LQG, LQG/LTR, pole placement and eigenvalue/eigenvector assignment. The basis for these control design methods is the design of a steady-state Kalman-Bucy filter and/or an observer. Given the plant in state variable form, one calculates the optimal filter for

$$\dot{x} = Ax + Bu + K(y - Cx) \tag{2.11}$$

$$u = -F_1 x - F_2 p + u_0 \tag{2.12}$$

where K is the filter gain and F_1, F_2 are the regulator gains. Equation (2.11) represents either a Kalman filter or a Luenberger observer. The feed forward bias term (u_0) in the regulator equation (2.12) allows the controller to track reference signals. For the Kalman filter design, the equations are recast as

$$\dot{x} = Ax + Bu + B_d v \tag{2.13}$$

$$y = Cx + v_m \tag{2.14}$$

where v and v_m model random input disturbances and measurement noise, respectively. For filter design, these are assumed to be uncorrelated zero-mean white noise processes with intensities given by

$$\begin{bmatrix} v \\ v_m \end{bmatrix} \sim \begin{bmatrix} v_1 & 0 \\ 0 & \rho_1 v_2 \end{bmatrix} \tag{2.15}$$

The measurement noise intensity is parameterized by the scalar quantity ρ_1. Large values of ρ_1 indicate considerable uncertainty in the measurement noise resulting in a slowing filter (i.e., low bandwidth control law). The scaling of ρ_1 is used to tune the filter.

The gains (F_1, F_2) in the regulator equation (2.12) are determined by minimizing a cost functional of the form

$$\int_0^\infty (x'^T R_1 x' + \rho_2 u'^T u')\, dt \tag{2.16}$$

where $x' = x - x_0$ and $u' = u - u_0$. The output weighting matrix R_1 is chosen by the designer and often reflects the relative scaling of the individual modes to be controlled. The optimal solution is obtained by solving for the steady state solution of a matrix Ricatti equation. As before, the scalar ρ_2 is introduced here to tune the bandwidth of the regulator.

One method used for control design is to synthesize a number of control laws by varying ρ_1 and ρ_2 and selecting the "best" combination of filter and regulator to form a control law [YuanSt]. One can see that this method is quite ad hoc, and little physical insight is gained about the control design by varying the two noise ρ_1 and ρ_2. This technique provides the engineer with no methodical way to exploit knowledge of the plant uncertainty or of the size of the variation of the parameters in the control design problem.

The eigenvalue/eigenvector assignment method requires, as a performance and robustness specification, that the designer select a set of desired eigenvalues (λ_i) and corresponding set of eigenvectors ϕ_i [Wonham, SobL]. A feedback law K is found such that the eigenvalues of $A - BKC$ contain (λ_i) as a subset and the corresponding eigenvectors are close to (ϕ_i). In addition, the state vectors are shaped to satisfy some performance characteristics. Often the eigenvectors are selected to be the open-loop eigenvectors and the closed-loop poles are selected to be damped versions of the open-loop poles. There is no *a priori* way of choosing the eigenvectors to be the so called "optimal" set of vectors for performance and robustness properties [JuangLJ]. A major drawback is that robustness is based on a specific evaluation model; thus no conclusions can be drawn regarding destabilization due to variations from the design model.

To include robustness measures in the control problem formulation, the loop transfer recovery methods (LQG/LTR) was developed [DoySt]. First, a full state feedback compensator based on the steady-state Kalman-Bucy filter is designed. Robustness to uncertainty is then characterized in terms of a frequency dependent bound, with weighting functions developed to describe multiplicative input/output uncertainty measures and additive uncertainty descriptions. Points in the feedback loop are broken and their robustness characteristics evaluated against the design specification. Sufficient conditions in the frequency domain, based on singular values, are used to test the robustness of the control design in the presence of uncertainty. The filter design is iterated on by varying the noise values ρ_1 and ρ_2 until the closed loop frequency response meets the robustness specifications at high frequencies and bandwidth specifications at low frequencies.

One limitation of LQG/LTR is the conservativeness of the singular value tests. The robustness bounds specified by singular values on the inputs and outputs can severely restrict the performance of the control designs [YuanSt, SunJA]. Another shortcoming is that the designer is not readily able to include knowledge about the physical system, (i.e. model errors and parameter variations) into the control problem. This knowledge must be translated into robustness measures associated with different locations in the control loop. The main advantage of LQG/LTR is that it provides robustness guarantees at points in the feedback loop at which the singular value tests are satisfied, though at no other points in the loop.

These methods and others have been applied to the vibration attenuation control problem for large space structures. Both collocated and noncollocated examples have been addressed, via theoretical results and to a lesser extent, with experimental investigations. Results often discuss performance levels achieved, with no mention of the robustness of the control laws. Overall, there is a lack of results in the literature regarding the limitations of control with respect to quantitative performance and robustness levels for flexible structures with model error.

The methods discussed are based on designing a KBF filter or observer/regulator. A limitation of these approaches is the control designs are entirely dependent on the starting values of the "tuning" parameters used in the selection of measurement noise intensity and the control input cost weighting function. The designer must tweak these parameters in order to arrive at the design desired. Often these values have little or no physical relationship to the actual noise levels and actuator limitations in the control problem formulation.

A numerous amount of work has been published about collocated sensors and actuators ('collocated control') for which stability can be guaranteed with simple control laws, provided actuator and sensor dynamics are taken into account [BalMJ1, SteinG, BalMJ2]. The SISO problem was investigated in the late 1970s by a number of researchers [LinHK, BalMJ1]. They addressed the theoretical question of control design for unmodeled dynamics (observer and controller spillover) using output feedback. These methods did not address the issue of parameter variation in the models, for which stability is not guaranteed. A significant amount of control research in the past ten years has focused on noncollocated control design for large space structures. The SISO noncollocated problem was investigated by Cannon and Rosenthal [CanRos] both theoretically and experimentally. They remarked on the stability and performance limitations of noncollocated control design for lightly damped, flexible structures with significant parameter variations. Control designs for the system were developed using classical root-locus methods and LQG synthesis techniques. They show that flexible structures employing noncollocated control are extremely sensitive to parameter variations, with LQG control designs providing good performance only when the plant parameter values were well known. Performance degraded significantly as the structure being controlled was varied.

A change in parameter values of 25% leads to unstable control laws. The sensitivity of these designs to modal frequencies and damping values variation was also noted as was the destabilization of high frequency modes by the control laws.

All the methods discussed fail to integrate explicit knowledge of model errors, robustness bounds and performance specifications into a common framework. Recently H_∞ control design techniques, based entirely on frequency domain measures, have been applied to LSS control problems [DailLuk1, BalLDD, SafChF]. H_∞ control design provides a unified framework for addressing uncertainty measures and performance but the robustness bounds can be overly conservative. Knowledge of the mismatch between the physical system and its mathematical models can be incorporated into the control problem formulation via μ-analysis and synthesis methods. The μ-framework greatly reduces the conservativeness associated with H_∞ methods. A more complete discussion of this is presented in the next section.

Three major issues associated with the synthesis of control laws for vibration attenuation in LSS are addressed in this thesis. First, the tradeoffs between uncertainty descriptions and performance/robustness objectives in control design for flexible structures is addressed. A direct connection is presented between accurate uncertainty modeling and performance. Theoretical and experimental results are provided in chapter 7. The design of control laws that cross over in a region of numerous flexible modes is presented in chapter 8 and the importance of uncertainty descriptions for unmodeled modes is discussed. The final topic addressed is the limitations of noncollocated versus collocated control design in the presence of uncertainty. Discussion of the formulation of the control design problem and results from implementation on the Caltech flexible structure experiments are presented.

Chapter 3

Structured Singular Value (μ) Framework

This section briefly reviews frequency domain methods for analyzing the performance and robustness properties of feedback systems using the structured singular value (μ) [Doy1, Doy2, Pack, PackFanDoy]. The general framework, shown in figure 3.1, is based on linear fractional transformations (LFTs). Any linear interconnection of inputs, outputs, and commands along with perturbations and a controller can be viewed in this context and rearranged to match this diagram. P represents the system interconnection structure,

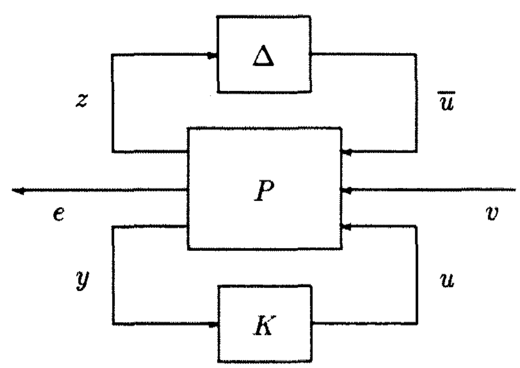

Figure 3.1: General Interconnection Structure

Δ the uncertainties, and K the control law. v is a vector of exogenous inputs and disturbances, e is a vector of errors to be kept small, y is a vector of measurement

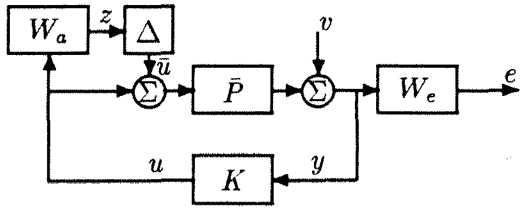

Figure 3.2: Example Control Problem Formulation

signals provided to the control design, u is a vector of inputs from the control law, z and $\bar{u}$ are outputs to and from the uncertainty block.

To see how one rearranges a block diagram into this framework, consider the control problem in figure 3.2. The control objective is to minimize the weighted output error, e, due to an input disturbance v, using feedback K. The model has uncertainty associated with the input signals, which is described by a multiplicative weighted uncertainty, W_a. The weighting function, W_e, reflects the inverse shape of the desired closed-loop sensitivity transfer function, $S \doteq (I - \bar{P}K)^{-1}$. The sensitivity function, S, relates the external disturbances, v, to the errors e. It is used to gauge the performance of a control law K. In this context, it is desired to make S as "small" as possible.

The block diagram in figure 3.2 can be rewritten as a LFT, figure 3.3, which fits into the general framework by defining the transfer function matrix to be P. The transfer function matrix, between the inputs and outputs, is given by:

$$\begin{bmatrix} z \\ e \\ y \end{bmatrix} = \underbrace{\begin{bmatrix} 0 & 0 & W_a \\ W_e\bar{P} & W_e & W_e\bar{P} \\ \bar{P} & I & \bar{P} \end{bmatrix}}_{P} \begin{bmatrix} \bar{u} \\ v \\ u \end{bmatrix}$$

As one can see, it is a straightforward exercise to develop LFT descriptions of block diagrams.

The following sections provide a background on H_∞ control theory, μ-analysis methods and μ-synthesis techniques. These represent the tools employed herein to address control design issues in flexible structures. The H_∞ control theory section is based mostly on Bruce Francis's book, **A Course in H_∞ Control Theory** [Francis] and Doyle & Chu's Honeywell Systems and Research **AFOSR Technical Report** [DoyChu1]. It

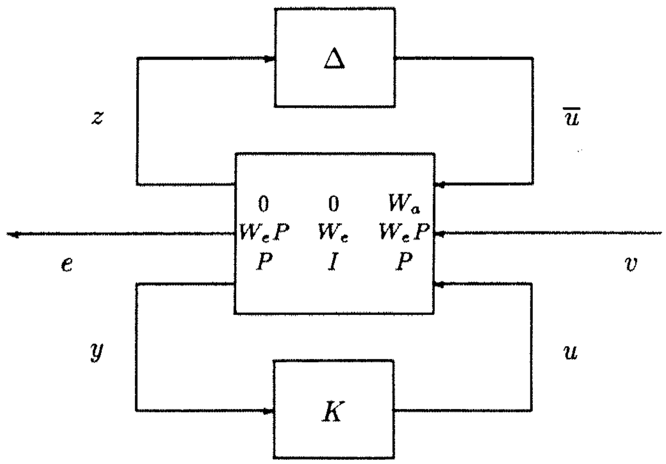

Figure 3.3: Linear Fractional Transformation of Example Problem

describes robustness and performance measures consistent with H_∞ theory and presents several examples of their use. The structured singular value (μ) analysis methods are discussed in section 3.3 along with their relation to H_∞ control theory. The structured singular value, μ, is used as a measure of the robustness of systems to structured and unstructured uncertainties. μ is a generalization of H_∞ analysis methods limited to unstructured uncertainty. H_∞ control design and μ analysis methods are combined to form the μ-synthesis technique for control design. Its advantages and limitations are expounded on in the last section. A step-by-step procedure is provided for the application of μ-synthesis methods.

3.1 Definitions

Following is a list of terms used extensively in this chapter.

Nominal Stability (NS) The nominal plant model has to be stabilized by the controller design. This is a minimum requirement.

Nominal Performance (NP) In addition to nominal stability, the nominal closed-loop response should satisfy some performance requirements. In the synthesis problem, performance is defined in terms of the weighted H_∞-norms for the closed-loop system transfer function between the exogenous inputs (disturbances) and "errors" (sensor outputs). This norm describes the "worst-case" closed-loop response, over frequency, to disturbances.

Robust Stability (RS) The closed-loop system must remain stable for all possible plants as defined by the uncertainty descriptions.

Robust Performance (RP) The closed-loop system must satisfy the performance requirement for all possible plants as defined by the uncertainty description.

Most modern control design methods only address the problem of nominal stability and nominal performance. Stability margins used in classical frequency domain methods attempt to address the robust stability problem, but they may be misleading for multivariable systems. These margins neglect the interaction and cross coupling present in multivariable systems. One method that deals with the robust performance question, in a multivariable framework, is μ-based analysis and synthesis techniques.

3.2 H_∞ Control Theory

H_∞ control design is concerned with meeting frequency-domain performance criteria. The Hardy space H_∞ consists of all complex-valued function $F(s)$ of a complex variable s which are analytic and bounded in the open right half plane (**rhp**). For real-rational functions, $F \in \Re H_\infty$, the infinity norm is given by

$$\|F\|_\infty = \sup_\omega \bar{\sigma}(F(j\omega)) \quad \forall \omega \in \Re \tag{3.1}$$

where $\bar{\sigma}$ denotes the maximum singular value. In single-input/single-output (SISO) systems equation (3.1) states that $\| F \|_\infty$ is the distance from the origin to the farthest point on the Nyquist plot of $F(s)$. Throughout this section, we will restrict ourselves to SISO linear, time-invariant, finite dimensional systems.

3.2.1 Nominal Performance

The H_∞-norm appears as a performance measure in many input/output systems. Consider the performance in terms of bounds on the output e in the presence of uncertain bounded inputs v. Bounds for both v and e can be expressed in terms of power, energy, or magnitude norms. The signals are assumed to be scalars so spatial, (i.e., n-dimensional vector), norms are not an issue.

Consider the following alternative assumptions about the signals: they are bounded in either "average power," "total energy," or "magnitude." The power and energy terms indicate that the integrals of the square of the signals are involved. Let v be a function of time such that on any finite interval it is square integrable. The three different types of bounds on u are defined as:

$$\text{1.) } \textit{Power} \qquad \mathbf{BP} = \{v \mid \lim_{T\to\infty} \frac{1}{2T}\int_{-T}^{T} \mid v(t) \mid^2 dt \; < \; 1\} \tag{3.2}$$

$$\text{2.) } \textit{Energy} \qquad \mathbf{BL_2} = \{v \mid \|v\|_2^2 = \int_{\infty}^{\infty} \mid v(t) \mid^2 dt \; < \; 1\} \tag{3.3}$$

$$\text{3.) } \textit{Magnitude} \qquad \mathbf{BL_\infty} = \{v \mid \|v\|_\infty = \sup_t \mid v(t) \mid \; < \; 1\} \tag{3.4}$$

The prefix $\mathbf{B}$ denotes the unit ball. The input signals are fed into the transfer function F and the properties of the output signals are evaluated. Sinusoids bounded in magnitude by 1 are also used as inputs. The norms are scaled to 1 because any scaling can be absorbed into the transfer function F. Similarly, any weighting due to filtering can be absorbed into F. Therefore, only unweighted signals need be considered. The weights associated with v and e reflect the spectral or frequency content of the input signals and performance specifications. All signals are assumed to be complex. The H_2 and H_∞ norms are defined as:

$$\|F\|_2 = \left(\frac{1}{2\pi}\int_{-\infty}^{\infty} F(\jmath\omega)^* F(\jmath\omega) \; d\omega\right)^{\frac{1}{2}} \tag{3.5}$$

$$\|F\|_\infty = \max_{\omega} \bar{\sigma}(F(\jmath\omega)) \tag{3.6}$$

The H_∞ norm is the induced norm from the following sets of input and output signals.

Input Signal	Output Signal
Power	Power
Energy	Energy
Magnitude	Power
Sinusoids	Power
Sinusoids	Magnitude

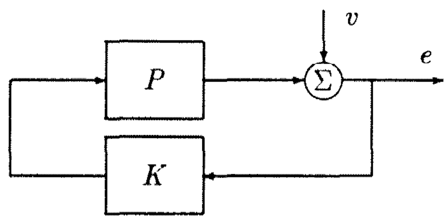

Figure 3.4: H_∞ Disturbance Attenuation Problem

The assumptions leading to $||F||_\infty$ are that either the input, v has a fixed power spectrum and the output, $e \in$ **BP** or v, is a stochastic process with fixed power spectral density and the output performance is measured in terms of the variance of e. The $||F||_2$ norm arises when v is a fixed signal and $e \in \mathbf{BL_2}$. Note that the induced norm from magnitude to power is approximated by a scalar multiple of the H_∞-norm.

Frequency dependent weighting functions can be used to shape the spectral content of signals and performance specifications. Often the physical process is modeled as composed of inputs of bounded power rather than perfectly known signals of fixed power spectrum, leading to the $|| \cdot ||_\infty$ norm [DoyChu1]. Modeling of uncertainties with the $|| \cdot ||_\infty$ norm is motivated by the types of model errors, whereas modeling performance objectives as a $|| \cdot ||_\infty$ norm instead of the $|| \cdot ||_2$ often isn't physically motivated. The benefit of transforming performance measures into the $|| \cdot ||_\infty$ norm becomes apparent when robustness and performance objectives are included in the control problem formulation [Zames, Doy1]. In addition, one can find weights that transform the problem in terms of the $|| \cdot ||_2$ norm into one involving only the $|| \cdot ||_\infty$ [Sideris].

The system shown in figure 3.4 is an example of the application of the H_∞ norm to the disturbance attenuation problem. The objective is to attenuate the effect of v on the output e in a suitably defined sense. The transfer function from v to e is the sensitivity function, S. Suppose z is any signal such that $z \in \mathbf{BL_2}$ with some frequency weighting function W, where W, $W^{-1} \in H_\infty$, and $v = Wz$. That is, the disturbance signal class consists of all z in $\mathbf{BL_2}$ such that $||W^{-1}v||_\infty \leq 1$. This can be interpreted as a constraint on the weighted energy of v with the energy density spectrum $|v(\jmath\omega)|^2$ weighted by the factor $|W(\jmath\omega)|^2$ or $\max_{z \in \mathbf{BL_2}} || WSz ||_\infty$. This set of signals has its

Figure 3.5: (a) Additive Uncertainty Model and (b) Additive Noise Model

energy concentrated in the frequency band where $|W(j\omega)|$ is relatively large.

The disturbance attenuation objective is to minimize the energy of e for the worst input signal v , or equivalently, the H_∞ norm of the weighted sensitivity function, $||WS||_\infty$, is to be minimized. In the H_∞ synthesis problem, P and W would be given and K would be chosen to minimize $||WS||_\infty$ subject to internal stability of the closed-loop system. Without any uncertainty in the model, the control design optimizes the *nominal performance* of the system.

3.2.2 Robust Stability

The infinity norm, $||\cdot||_\infty$, lends itself to analyzing systems for stability in the presence of uncertainty. Uncertainty is often described as norm-bounded variations from a nominal model. The uncertainty can vary across frequency, which is reflected in a weighting function associated with the norm-bound. Plants described by a nominal model and a perturbation of the model are very different from systems described by a nominal model and an additive noise process. The difference lies in the fact that plant perturbations can destabilize a nominally stable plant whereas an additive noise process cannot destabilize a plant. This is apparent when the eigenvalues of the system are analyzed. Consider the block diagram in figure 3.5. In figure 3.5(b), the eigenvalues of P remain the same regardless of the input noise process. In figure 3.5(a), treat ΔP as a norm-bounded perturbation. Depending on the size of the norm bound, ΔP can destabilize the system P. It is even more apparent when feedback is introduced. This is a fundamental difference in the two plant descriptions.

Models of real systems are never exact, because there is always some variation between the physical system and the mathematical model. Describing the model by a nominal plant P and norm-bounded perturbations or uncertainties, ΔP, one is able to define a rich class of models. This type of description allows the inclusion of destabi-

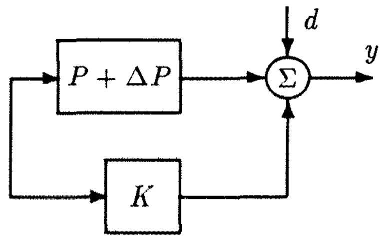

Figure 3.6: Robust Stability Control Problem Formulation

lizing perturbations, therefore, the issue of ***robust stability*** must be addressed. That is, we desire a set of plant models, defined by $P + \Delta P$, to be stabilized by a controller, K, in the presence of the perturbation ΔP. Stability is taken to mean that the perturbed system has no closed right half plane poles. This is where the infinity norm, $|| \cdot ||_\infty$, is of use.

A couple of example problems are formulated to show how H_∞ norm constraints appear as control objectives. First, an example of the small gain theorem. Consider figure 3.4; let P and K be transfer functions that are real-rational, proper, and stable. The transfer function from v to e is $(1 - PK)^{-1}$. The Nyquist criterion states that this system is stable if and only if the Nyquist contour of PK doesn't pass through or encircle the point $s = 1$. A sufficient condition for stability is the small gain condition $|| \, PK \, ||_\infty < 1$.

Now the problem of robust stabilization. Let the plant be a transfer function defined as $P + \Delta P$ and the controller is K shown in figure 3.6. P is the nominal plant model and ΔP is an unknown perturbation. Suppose the system is nominally stable, that is the feedback system is stable for $\Delta P = 0$. Robust stabilization answers the question, "How large can $| \, \Delta P \, |$ be while maintaining system stability?"

From the physics of the problem, the perturbation of the plant model, ΔP, can be bounded across frequency by a function $W \in \Re H_\infty$, such that for all $\omega \in [0, \infty)$

$$| \, \Delta P(\jmath\omega) \, | \; < \; | \, W(\jmath\omega) \, | \tag{3.7}$$

W is a weighting function describing the uncertainty in the model as a function of frequency. It is formulated to be a proper, stable, real-rational, minimum phase transfer

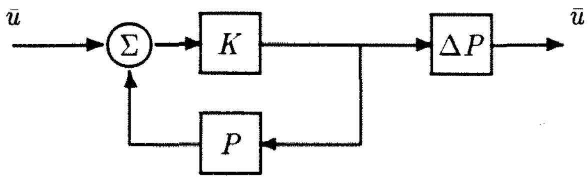

Figure 3.7: Reformulation of Robust Stability Control Problem

function. This uncertainty description is unstructured, because the only assumption made about the model error is that it is magnitude bounded.

The new question is, "How large can $|W|$ be while maintaining stability?" Redrawing the block diagram, figure 3.7, and noting that $K(1-PK)^{-1} \in \Re H_\infty$, the small gain theorem gives that the system will be stable if

$$\| \Delta PK(1-PK)^{-1} \|_\infty < 1 \tag{3.8}$$

A sufficient condition is

$$\| WK(1-PK)^{-1} \|_\infty \leq 1 \tag{3.9}$$

Thus, the H_∞-norm bound of a weighted closed-loop transfer function provides a sufficient condition for robust stability.

The H_∞ control methodology provides a common framework in which to analyze and design for robustness characteristics and performance requirements of a system. One is able to incorporate knowledge of the modeling limitations, in terms of frequency response data, into the control analysis and design problem. For SISO systems, H_∞ analysis is comparable with the Nyquist criteria, providing a connection between modern techniques and classical control methods, which has been the backbone of control for the last fifty years. A shortcoming of the H_∞ methodology is its inability to handle *structure* associated with robustness bounds and performance measures. The stability or performance analyses involve a singular value test, which often is inappropriate and leads to conservative results. The structured singular value (μ) was developed to address this limitation.

3.3 μ-Analysis Methods

μ-analysis methods are used in the analysis of systems with structured and unstructured uncertainty. For the purpose of analysis, the controller may be thought of as just another system component. The inclusion of the controller into the plant reduces the diagram in figure 3.1 to that in figure 3.8-(a). The analysis problem involves determining

Figure 3.8: General Framework: (a) Analysis and (b) Synthesis Problem

whether the error e remains in a desired set for sets of input v and perturbation Δ. The uncertainty in v and Δ as well as the performance specifications on e are normalized to 1. This requires all weighting functions and scalings be absorbed into the interconnection structure G. Furthermore, G can be partitioned so that the input-output map from v to e is expressed as the following linear fractional transformation

$$e = F_u(G,\Delta)v \tag{3.10}$$

where $$F_u(G,\Delta) = G_{22} + G_{21}\Delta(I - G_{11}\Delta)^{-1}G_{12}\ , \qquad G = \begin{bmatrix} G_{11} & G_{12} \\ G_{21} & G_{22} \end{bmatrix}$$

The nominal performance objective is simply

$$\| G_{22} \|_\infty = \sup_{\omega}\ \overline{\sigma}\,(G_{22}(jw)) \tag{3.11}$$

This is the transfer function from v to e with the uncertainty, Δ, set to zero. Robust stability for unstructured uncertainty (assuming $\overline{\sigma}(\Delta) \leq 1$ known) depends only on $\| G_{11} \|_\infty$. Nominal performance and robust stability tests of uncertainty descriptions can be evaluated based on independent elements of G. Unfortunately, norm bounds are inadequate for dealing with robust performance and realistic models of structured plant uncertainty. To handle these questions, the structured singular value, μ is used.

μ analyzes linear fractional transformations when Δ has structure. A more complete background on μ is found in [Doy1, Doy2, DoyWSt, Pack].

First we assume that Δ belongs to the set

$$\underline{\Delta} = \{\text{diag}(\delta_1 I_{r1}, \ldots, \delta_s I_{rs}, \Delta_1, \ldots, \Delta_k) : \ \delta_i \in C, \ \Delta_j \in C^{m_j \times m_j}\} \subset C^{n \times n} \quad (3.12)$$

$$with \ \sum_{i=1}^{s} r_i + \sum_{j=1}^{k} m_j = n \quad \text{and} \quad B\underline{\Delta} = \{\Delta \in \underline{\Delta} \mid \overline{\sigma}(\Delta) \leq 1\}$$

and I_i is an identity matrix of size i. For $M \in C^{n \times n}$, $\mu(M)$ is defined as

$$\mu(M) := \frac{1}{\min\{\overline{\sigma}(\Delta) : \ \Delta \in \ \underline{\Delta}, \ \det(I + M\Delta) = 0\}} \quad (3.13)$$

unless no $\Delta \in \underline{\Delta}$ makes $I + M\Delta$ singular, then $\mu(M) = 0$. The function μ has the property $\mu(\alpha M) = \mid \alpha \mid \mu(M)$.

Obviously, μ is a function of M, which depends on the structure of $\underline{\Delta}$. For this discussion, the structure should be clear from the context. Let

$$\underline{U} = \{\text{diag}(e^{j\Theta_1} I_{r1}, \ldots, e^{j\Theta_s} I_{rs}, U_1, \ldots, U_n) | U_i^* U_i = I, \ \ \Theta_i \in \mathbb{R}\}$$

$$\underline{D} = \{\text{diag}(D_{r1}, \ldots, D_{rs}, d_1 I_1, d_2 I_2, ..., d_n I_n) \mid D_i = D_i^* > 0, d_i \in \mathbb{R}_+\}$$

where the set $\underline{U}$ and $\underline{D}$ match the structure of $\underline{\Delta}$. Note that $\underline{U}$ and $\underline{D}$ leave Δ invariant in the sense that $\Delta \in \underline{\Delta}$ and $D \in \underline{D}$ implies that $\overline{\sigma}(\Delta U) = \overline{\sigma}(U\Delta)$ and $D\Delta D^{-1} = \Delta$. The sets $\underline{U}$ and $\underline{D}$ can be used to obtain the bounds

$$\sup_{U \in \underline{U}} \rho(MU) \ \ \leq \ \ \mu(M) \ \ \leq \ \ \inf_{D \in \underline{D}} \overline{\sigma}(DMD^{-1}) \quad (3.14)$$

where ρ denotes the spectral radius.

Key theorems regarding μ prove that the lower bound is always an equality and the upper bound is an equality for three or fewer full blocks [Doy1]. Unfortunately, the optimization problem implied by the lower bound has multiple local maxima and therefore does not immediately yield a reliable computational approach. A lower bound algorithm, based on the power method for eigenvalues, has been developed and provides a better estimate than the spectral radius condition [PackFanDoy] but is not guaranteed to converge to μ. The upper bound $\overline{\sigma}(DMD^{-1})$ can be reformulated as convex in $\ln(D)$ (so that the infimum can be found by searching over $n - 1$ real parameters), although the infimum is not necessarily equal to μ. Extensive experimentation [Doy2] indicates that the upper bound is close to μ in general. This result is simply a conjecture and hasn't been proven. The worst case ratio of the lower bound to the upper bound, for nonrepeated blocks found to date is on the order of 0.85. Although we do not directly calculate μ, tight bounds on it are available.

In the frequency domain μ test, which is used extensively, the upper bound consists of finding the optimal D scaling at each frequency. The calculation of the upper bound for μ of the transfer function G across frequency is given by equation (3.15).

$$\mu(G(j\omega)) \leq \inf_{D(j\omega)\in\underline{D}} \bar{\sigma}(D(j\omega)G(j\omega)D(j\omega)^{-1}) \qquad \forall\omega \tag{3.15}$$

The importance of μ in studying robustness of feedback systems is due to two theorems that characterize in terms of μ, the robust stability and robust performance of a system in the presence of structured uncertainty. In figure 3.8(a), uncertainty is fed back from z to $\overline{u}$ through a structured $\Delta \in \underline{\Delta}$. Hence, the input-output map from v to e can be expressed as

$$e = F_u(G,\Delta)v \; = \; (G_{22} + G_{21}\Delta(I - G_{11}\Delta)^{-1}G_{12})u \tag{3.16}$$

If $\sup_\omega \; \mu(G_{11}(j\omega))$ is less than 1 for all frequency, then $(I - G_{11}\Delta)$ is invertible and non-singular. This is similar to the small gain theorem, with the gain around the loop always less than 1. Therefore, the input-output map is stable for all the plants defined by the set $F_u(G,\Delta)$. A more formal statement of robust stability follows.

Theorem: Robust Stability (R.S.)

$$F_u(G,\Delta) \text{ stable} \, \forall\Delta \in B\underline{\Delta} \;\; \textbf{iff} \;\; \sup_\omega \; \mu(G_{11}(jw)) \leq 1 \qquad 0 \leq \omega \leq \infty$$

This reduces to $\sup_\omega \; \bar{\sigma}(G_{11}(j\omega)) \leq 1$ when Δ is a full block, unstructured uncertainty. Hence the connection with the H_∞ norm. When Δ has structure, the $\|\cdot\|_\infty$ provides an upper bound which is a more conservative measure of robustness.

For control design, one is really interested in *robust performance*. That is, achieving the performance required in the presence of uncertainty. We will characterize performance in terms of the $\|\cdot\|_\infty$ of the transfer function from disturbance (v) to error (e) in figure 3.8(a). The robust performance question can be formulated as a robust stability question, by associating a full block uncertainty, Δ_{k+1}, with the performance norm.

Δ_{k+1} is of size (number of disturbances v), by (number of error outputs e). Thus, robust performance is equivalent to robust stability with respect to a different block structure. Formally stated:

Theorem: Robust Performance (R.P.)

$$F_u(G,\Delta)\,\text{stable}, \quad and \quad \| F_u(G,\Delta) \|_\infty \leq 1 \;\; \forall \Delta \in B\underline{\Delta} \;\; \textbf{iff} \;\; \sup_\omega \mu(G(jw)) \leq 1.$$

$$\text{with} \quad \| F_u(G,\Delta) \|_\infty \equiv \| G_{11} + G_{12}\Delta(I - G_{22}\Delta)^{-1}G_{21} \|_\infty \quad 0 \leq \omega \leq \infty$$

(where μ in Theorem **R.P.** is computed with respect to the structure $\underline{\Delta} = \{\mathrm{diag}(\Delta, \Delta_{k+1})\}$, Δ_{k+1} is the performance block and $\Delta \in \underline{\Delta}$.)

3.4 H_∞ Synthesis

For the purpose of synthesis, the maximum singular value of the perturbation Δ can be assumed to be bounded in magnitude by 1. This results in the synthesis problem presented in figure 3.8-(b). Hence, the synthesis problem involves finding a stabilizing controller K such that the performance requirements are satisfied with the inclusion of uncertainties. The interconnection structure P is partitioned so that the input-output map from v' to e' is expressed as the following linear fractional transformation

$$e' = F_l(P,K)v' \quad \text{where} \quad F_l(P,K) = P_{11} + P_{12}K(I - P_{22}K)^{-1}P_{21}\,. \tag{3.17}$$

For a H_∞ optimal control problem, the objective is to find a stabilizing controller K, which minimizes $\| F_l(P,K) \|_\infty$.

The H_∞ optimization problem has been the subject of an enormous amount of research in the past 10 years. Recently, new state-space formulas have become available, which make this problem numerically tractable [DGKF, GlovDoy1, GlovDoy2]. These algorithms involve a search method and the solution of two Ricatti equations. For control design, a value γ is selected and checked as to whether a controller, K, can be generated which satisfies $\| F_l(P,K) \|_\infty < \gamma$ and the closed-loop system is internally stable. If either of these tests fails, the γ value is increased and control design is reformulated. In the limit as $\gamma \to \infty$, the control law approaches the $\| \cdot \|_2$ optimal solution. Assuming the weighting functions have been selected to normalize the desired $\| \cdot \|_\infty$ to 1, then,

$\| F_l(P, K) \|_\infty < 1$ indicates the formulation of a control law K that satisfies the specified criteria. The H_∞ control design methods are used in the μ-synthesis design methodology.

3.5 μ-Synthesis Methodology

The μ-synthesis methodology essentially integrates the H_∞ optimization method for synthesis and the structured singular value (μ) for analysis [Doy2, DoyChu1]. The synthesis problem to be solved is, find a K to minimize

$$\inf_{K} \sup_{\omega} \mu(F_l(P(j\omega), K(j\omega))) \tag{3.18}$$

Unfortunately, this minimization does not have a closed form solution or a tractable numerical solution. Therefore, other methods have been developed to approximate a solution. Since the upper bound for μ can be obtained by scaling and applying the $\| \cdot \|_\infty$, the minimization problem can be reformulated as an H_∞ control design problem. The problem of robust controller design becomes one of finding a stabilizing controller K and a scaling matrix D such that the quantity

$$\| D F_l(P, K) D^{-1} \|_\infty$$

is minimized. One approach to solving this problem is to alternately minimize the above expression for either K or D while holding the other constant. For fixed D, it becomes an H_∞ optimal control problem and can be solved using the well-known state-space method [DGKF, GlovDoy1, GlovDoy2]. With fixed K, D can be formulated as a convex optimization problem. From the resulting data, the magnitude D is fit with a proper, stable, minimum phase, real, rational transfer function. This process is carried out iteratively until a satisfactory controller is constructed. Although this iterative scheme is not guaranteed to find a global optimum of the above minimization problem, the approach appears promising and consistent results have been obtained.

The μ-synthesis technique employed is defined as this D-K iteration. It is a two parameter minimization, which first minimizes over all controllers K with the scaling matrix D fixed, then minimizes over the scaling D with the controller K fixed. This is an iterative process, which is continued until the value of μ does not change or begins to increase. The D-scalings are proper, stable, real-rational transfer functions derived from the μ upper bound calculation. The basis for the D-K iteration method is the fact that an upper bound for μ is the ∞-norm.

The D-scalings associated with full blocks, $\Delta \in C^{n \times n}$, are real constants. Generating real, rational, proper, minimum phase transfer functions that fit the frequency varying D-scalings is done via several techniques. One method is to obtain phase information from the real data using a complex cepstrum method [Dailey, OppSch]. This produces minimum phase, complex data, which is then fit using linear least squares techniques. For repeated scalar blocks, $\delta_i I$, the scalings D are generally complex matrices. Fitting full matrix D scales that vary across frequency with transfer function matrices is a more difficult problem and the subject of current research efforts.

The transfer function scaling matrix, $D(s)$, is only an approximation to the optimal D scaling at each frequency point. The individual transfer functions for <u>each</u> input/output channel, $d(s)$, are usually chosen to be very low order, 3 states or less, because twice the number of states of $d(s)$ are added to the controller synthesis problem. For example, if the uncertainty structure, Δ, has two full block uncertainties of size 3×3 and a first order D scaling, $d(s)$, which was formulated for the first uncertainty block, it would add 6 states to the control design model. One state from each input/output pair and the control problem requires $d(s)$ and $d(s)^{-1}$.

There are several limitations of the D-K iteration for synthesis of control laws. One is that transfer functions are fit to the D scalings as a function for frequency, which may introduce some error. Another is that the D scales are only fit in the frequency range in which μ was analyzed; therefore, these scalings may lead to problems outside the frequency range of interest. Probably of greater concern is that this iteration method is not guaranteed to achieve a global optimum, because the optimization problem is not convex in both D and K, though it is convex in D and K individually. Therefore, the iteration process might iterate down to a local maximum instead of the global maximum. Examples can be constructed where μ equals the upper bound and the D-K iteration does not converge. Currently, the only way to test for a local minima is to restart the iteration process with a new scaling matrix, D, and redo the control design.

In practice, μ-synthesis usually converges to a control law which, we believe, is very close to the global minimum. Weak links in the synthesis process are the numerical issues associated with the formulation of an H_∞ control law. For lightly damped flexible structures, the poles of the system are near the $j\omega$ axis, which causes numerical problems in the solution of the Ricatti equations. Numerically robust and accurate algorithms for calculating solutions to generalized Ricatti equations are needed to enhance H_∞ control design. The D-K iteration is very useful because it provides control laws that are less conservative for structured uncertainty than a pure H_∞ control design. An H_∞ design is an upper bound for the μ-synthesis control law. This design methodology has been used extensively to synthesize a number of control laws for several different flexible structure experiments with great success [BalLDD, BalDoy4, BalChuD].

The following is a step-by-step procedure of how to integrate μ-analysis and H_∞ design methods to perform μ-synthesis.

1. Formulate the control design problem into the general framework given in figure 3.1 and shown below. Define the block structure associated with Δ. This entails

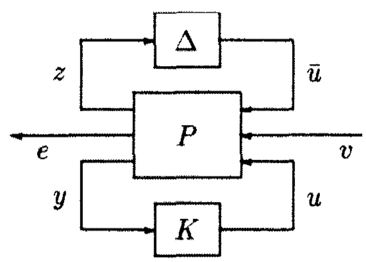

selecting weighting functions for the uncertainty descriptions and performance requirements. These quantities are scaled so that when the μ is 1, the requirements are satisfied. The structure of Δ is assumed to be as shown below. The uncertainty weights are included in the interconnection structure P.

$$\Delta = \begin{bmatrix} \Delta_1 & 0 & \dots & 0 \\ 0 & \Delta_2 & \dots & 0 \\ \vdots & \vdots & \ddots & \vdots \\ 0 & 0 & \dots & \Delta_{k+1} \end{bmatrix} \qquad \Delta_i = p_i \times q_i \qquad i = 1, 2, \dots, k+1 \quad (3.19)$$

2. Let $e' = \begin{bmatrix} z \\ e \end{bmatrix}$ and $v' = \begin{bmatrix} v \\ d \end{bmatrix}$ for the H_∞ synthesis problem shown below. Synthesize an optimal controller, K, which minimizes $\| F_l(P, K) \|_\infty$.

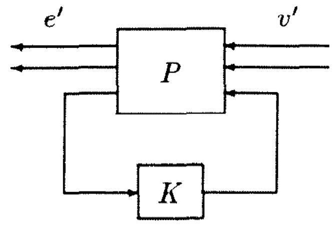

3. Form the closed-loop system, $G = F_l(P,K)$, shown below, using the synthesized control law K. Analyze the frequency response of $G(s)$ using μ. This requires calculation μ for a complex matrix at each frequency point ω. Check if $\mu(G(\jmath\omega)) \leq 1 \;\; \forall\, \omega$. $\mu \leq 1$ implies that the robustness and performance requirements defined in the problem formulation are satisfied. If this is the case, you are finished because the optimal H_∞ control design satisfies the design requirements; otherwise, continue.

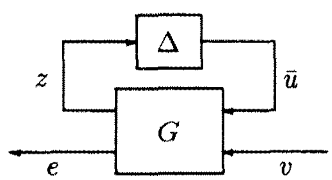

4. The upper bound calculation for μ,

$$\mu(G(\jmath\omega) \leq \inf_{D\in\underline{D}} (D(\jmath\omega)G(\jmath\omega)D(\jmath\omega)^{-1}) \quad \forall\, \omega$$

generates scaling matrices $D(\jmath\omega) \in \underline{D}$ at each frequency ω. There is one free parameter in these scaling matrices D, therefore the D scaling of the last block, Δ_{k+1}, is taken to be the identity matrix of size $I \in \Re^{p_{k+1} \times q_{k+1}}$. These D scalings match the structure of Δ. For full block uncertainty, $\Delta_i \in C^{n\times m}$, the D scaling is a constant. A more detailed discussion is given in the μ-analysis section [Doy1, Doy2, Pack].

5. The individual D scales associated with each uncertainty or performance block, Δ_i are fit with real, rational, stable, proper, minimum phase transfer functions whose magnitude match the D-scalings. From these transfer functions D_{left} and D_{right} are formed. (Note: $D_{left} = D_{right}$ if all the Δ_i block are square.)

6. The scaling matrices, D_{left} and D_{right} are augmented to the <u>original</u> plant interconnection structure as shown below. A new interconnection structure, P', is formed.

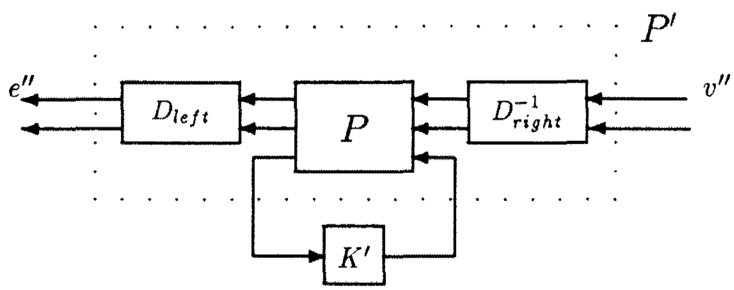

The scaling matrices, D_{left} and D_{right} are used to approximate

$$\mu(F_l(P,K)) \leq \inf_{D \in \underline{D}} \| D_{left} F_l(P,K) D^{-1}_{right} \|_\infty \qquad \forall\, \omega$$

for which a solution can be found via H_∞ optimization techniques.

7. Synthesize a control law K' to minimize $\|F_l(P', K')\|_\infty$.

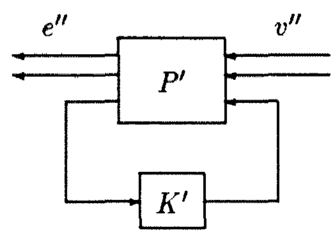

8. Form the closed-loop system, $G' = F_l(P, K')$, using the <u>original</u> plant interconnection structure, P, and the new control law K'. (Note: One can use the modified interconnection structure, P', for analysis but the extra states associated with the old D scalings will be included in the model. These scalings are unnecessary for the analysis problem.) Test if $\mu(G'(\jmath\omega)) \leq 1 \;\; \forall\omega$. If this requirement is satisfied, finish iterating; if not, fit the optimal $D(\jmath\omega)$ scalings for $\mu(G'(\jmath\omega))$ and form new D scaling transfer functions, D'_{left} and D'_{right}.

9. D'_{left} and D'_{right} are augmented to the <u>original</u> plant interconnection structure, P, and a new interconnection structure P'' is formed. (Note: Augmenting P' with

D'_{left} and D'_{right} would have the D scalings from the old μ problem and the new μ test. One can factor the old D scales into the fitting of the new D scales, thereby eliminating the need for the old D scalings in the plant interconnection structure. Therefore, there is no geometric explosion of the number of states in the control design problem.)

10. Continue the iteration until $\bar{\sigma}(G(j\omega)) \leq 1 \ \forall\omega$, the upper bound remains stationary or starts increasing.

The μ-synthesis methodology is used to design all the control laws discussed in this thesis. μ-synthesis offers a flexible, general framework in which to design control laws for flexible structures to achieve robust performance. It allows one to include both frequency domain and parametric information about uncertainties in the control design model. The performance requirements are entered via frequency weighting functions, providing the engineer a means to formulate performance specifications based on frequency domain insight. There is still a significant number of parameters in the control design methodology whose choices require the designer's experience and understanding of the physics of the problem. The μ-synthesis framework provides an environment for the designer to include assumptions and weighting selections that effect the robustness and performance properties of the control laws.

Chapter 4

Caltech Experimental Flexible Structure

The Caltech experimental flexible structure is designed to include a number of attributes associated with large flexible space structures. These include lightly damped, closely spaced modes, collocated and noncollocated sensors and actuators, and numerous modes in the controller crossover region. In addition to these considerations, expandability of the structure is a desired feature. Modular construction provides a means for increasing the modal density in a frequency range of interest.

One objective of the initial design is for the structure to exhibit poor performance with the implementation of a collocated velocity feedback law. In many cases, collocated sensors and actuators with velocity feedback provide sufficient control to achieve the desired performance objectives. Unfortunately, this approach can be insufficient if the performance requirements are associated with locations on the structure without collocated sensor/actuator pairs. Multivariable control design techniques take advantage of extra sensors and actuators to provide improved performance as compared with collocated velocity feedback.

4.1 Phase 1 Design

The initial experimental structure, figure 4.1, consists of two stories, three longerons (columns) and three noncollocated sensors and actuators. The first story columns are

.838 m (33 in.) long with the second story columns measuring .759 m (29.9 in.) Including the platforms, the structure has a height of 1.651 m (65 in.). The two platforms are the shape of an equilateral triangle with a .406 m (16 in.) base. The longerons are connected between the stories via a triangular mating fixture and three bolts. This allows for the easy addition of stories to the structure. All the longerons are shrunk fit and welded to their mating brackets to reduce the effects of joint nonlinearities.

The first story platform is a 9.52 mm (3/8 in.) thick plate of aluminum, weighing 2.36 kg (5.2 lbs), with diagonal mounting brackets for attachment of the actuator diagonals. The second story platform is a 6.35 mm (1/4 in.) thick plate of aluminum with mounting holes for three accelerometers. It weighs 1.55 kg (3.4 lbs). A small offset mass is located on the second story platform to lower the torsional natural frequencies. The entire structure hangs from a mounting structure fixed to the ceiling. This alleviates the problem of buckling of the longerons. The three actuators are attached to the mounting structure and act along the diagonals of the first story. The three sensors are accelerometers that are located on the second bay platform.

The two stories are designed to have the same first bending natural frequency. This is obtained by selecting the stiffness of the second story columns to be a fourth the stiffness of the first with a similar ratio between the masses of the two stories. This ratio of stiffness and masses allows the interaction of the two stories to decrease the first bending natural frequency of the combined structure without significantly spreading out the remaining modes. The interaction leads to poor performance of a collocated velocity feedback at the voice coil actuators. One can see by fixing the first story to be rigid (which is similar to implementation of a collocated velocity feedback law at the actuators) would provide little reduction in the second floor motion for similar second story excitation. This indicates that the use of collocated velocity feedback at the voice coil actuators would not significantly reduce vibration on the second platform.

4.1.1 Voice Coil Actuators

The voice coil actuators are fabricated by Northern Magnetics Inc.. They are similar to typical loudspeakers, outputting a force proportional to the input voltage. The actuators are mounted in line with the column diagonals and are rated at ± 1.36 kg (3 lbs) of force

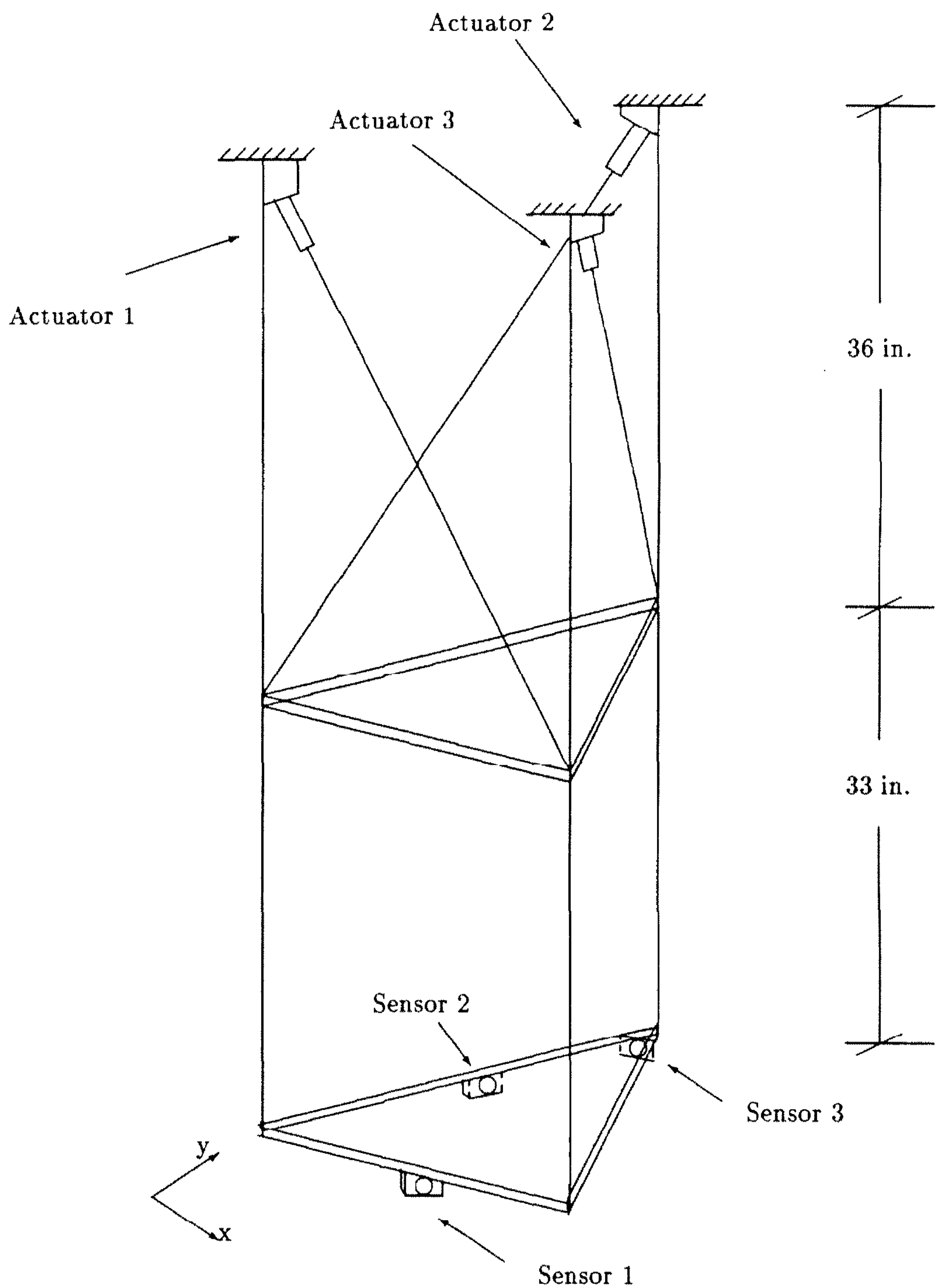

Figure 4.1: Phase I Caltech Flexible Structure

at $\pm$ 5 volts. Command signals are supplied to the actuator from a Masscomp computer used to implement to real time control laws. Commands to the actuator are sent via a Masscomp digital/analog (D/A) board through a current amplifier. The actuator model is derived from a theoretical model and bench tests. Static tests are run for input voltages between $\pm$ 5 volts to formulate a linear relationship between the input voltage and output force. Frequency response data measured from input/output experiments verified this relationship with an actuator bandwidth of 60 Hz determined.

4.1.2 Air Actuators

Three air actuators are used as input disturbances to the second story platform. Each actuator is placed to blow a stream of air directly on each sensor. These actuators consist of compressed air, which is pulsed on and off by solenoids. Commands to the solenoids are sent via the Masscomp D/A. Models of air actuators are difficult to formulate because no accurate measurement of the orifice diameter, air pressure in the line, or force being exerted at the sensors is available. In an effort to develop a crude model, a sinusoidal frequency sweep between 1 and 6 Hz is input to the solenoid and the output response of the flexible structure are measured. The solenoids are determined to have a flat frequency response up to approximately 4 Hz at which point their transfer function rolls off rapidly.

4.1.3 Accelerometers

The sensors are Sunstrand QA-1400 accelerometers. These are mounted on the second story platform, located along the x-axis, y-axis, and at 45 degrees to both axes. The accelerometers have a flat frequency response between 0 and 200 Hz and are extremely sensitive. The noise associated with them is rated at 0.05% of the output at 0-10 Hz and 2% at 10-100 Hz. Models of the accelerometers are generated from data supplied by Sunstrand. The sensors are scaled for accelerations of .016 g per volt to provide a maximum $\pm$ 5 volts output at peak accelerations of the input disturbance. The accelerometer output is conditioned by a 100 Hz, 4^{th} order Butterworth filter prior to input into the analog/digital (A/D) converter to provide attenuation of high frequency signals and noise.

Tests are performed to verify the noise characteristics of the accelerometer. During

Sensors	Serial Number	Sensitivity (mA/g)	(Volts/g)	(g/Volts)
1	# 1340	1.25500	63.00	0.0159
2	# 1343	1.25770	63.14	0.0158
3	# 1294	1.29215	64.87	0.0154

Table 4.1: Phase I Accelerometer Scalings

testing, the accelerometers are isolated from the building due to their sensitivity by hanging them from a 3 ft. rubber band. It is determined that the building vibration is two orders of magnitude higher than the sensor noise in the low frequency range and the accelerometer noise is in line with the manufacturer specifications.

The sensors are based on a force balance design. The principle of operation for these sensors is that an applied acceleration produces a torque on the pendulous mass located inside the accelerometer. Displacement is sensed by a detector that produces a proportional output voltage. This output is amplified and conditioned, then fed to the torquer coil fixed to the mass. The current through the coil develops a restoring torque equal and opposite to the applied acceleration. The same current is also passed through an external load resistor generating an output voltage proportional to applied acceleration. Each accelerometer has a 50.2 $K\Omega$ resistor in-line to scale the acceleration levels to approximately 0.016 g per volt. Table 4.1 has a list of the scaling values for each sensor.

4.2 Phase II Design

The phase II design of the Caltech flexible experiment, figure 4.2, consists of three stories, three longerons, six actuators and six sensors. The first story is the same as in the initial structure: the columns are .838 m (33 in.) and the platform is a solid equilateral triangular platform with a .406 m (16 in.) base. The second story columns measure .559 m (22 in.) and the third story columns are .813 m (32 in.) long. The total height of the phase II structure, including the platforms, is 2.32 m (87.88 in.). The second and third story platforms are 6.35 mm ($\frac{1}{4}$ in.) thick aluminum plates with the same dimensions as the first bay but with an equilateral triangle, of base dimension

.356 m (14 in.) cut out of their center. This reduces the weight of each bay, thereby increasing the natural frequencies of the global flexible modes. The longerons connect the stories via triangular mating fixtures and three bolts. As in the phase I structure, all the longerons are shrunk fit and welded to the mating brackets. The entire structure hangs from a mounting structure fixed to the ceiling.

The same three voice coil actuators, acting along the first bay diagonals, remain in place from the initial structure. Three additional proof mass actuators are mounted to the bottom, third bay, and positioned parallel to the sides of the triangular platform. The center of each proof mass actuator is located in the center of the platform side. Three accelerometers are positioned parallel to the platform sides, corresponding to the proof mass actuators, and located on bays 2 and 3. The three accelerometers on platform 3 are collocated with the proof mass actuators. The actuators are mounted on the bottom of the platform and the sensors on top. There are three additional linear voltage displacement transducers (LVDT) sensors located on the proof mass actuators. These are used in a local feedback loop to linearize the response of the proof mass actuators. Placement of the actuators and sensors are selected to investigate issues associated with collocated and noncollocated control design for flexible structures.

4.2.1 Accelerometers

Two additional Sunstrand QA-700 and one QA-1400 accelerometers are used on the structure. These have the same characteristics as the QA-1400 accelerometers discussed previously. All the accelerometers have a 20.0 $K\Omega$ resistor in line to scale the acceleration levels to approximately 0.04 g per volt. Table 4.2 contains a list of the accelerometers and their scale factors.

4.2.2 Linear Voltage Displacement Transducers (LVDT)

The three LVDTs are Trans-Tek model 244. They are designed to measure displacements up to ± 1.5 inches accurately. The input voltage is selected such that a displacement of ± 1.0 inch correspond to ± 5 Volts. These transducers have zero hysteresis, and are linear across their operating range to within ± 0.5 % of their output voltage. An LVDT is located on each proof mass actuator for use in a local feedback loop to linearize the

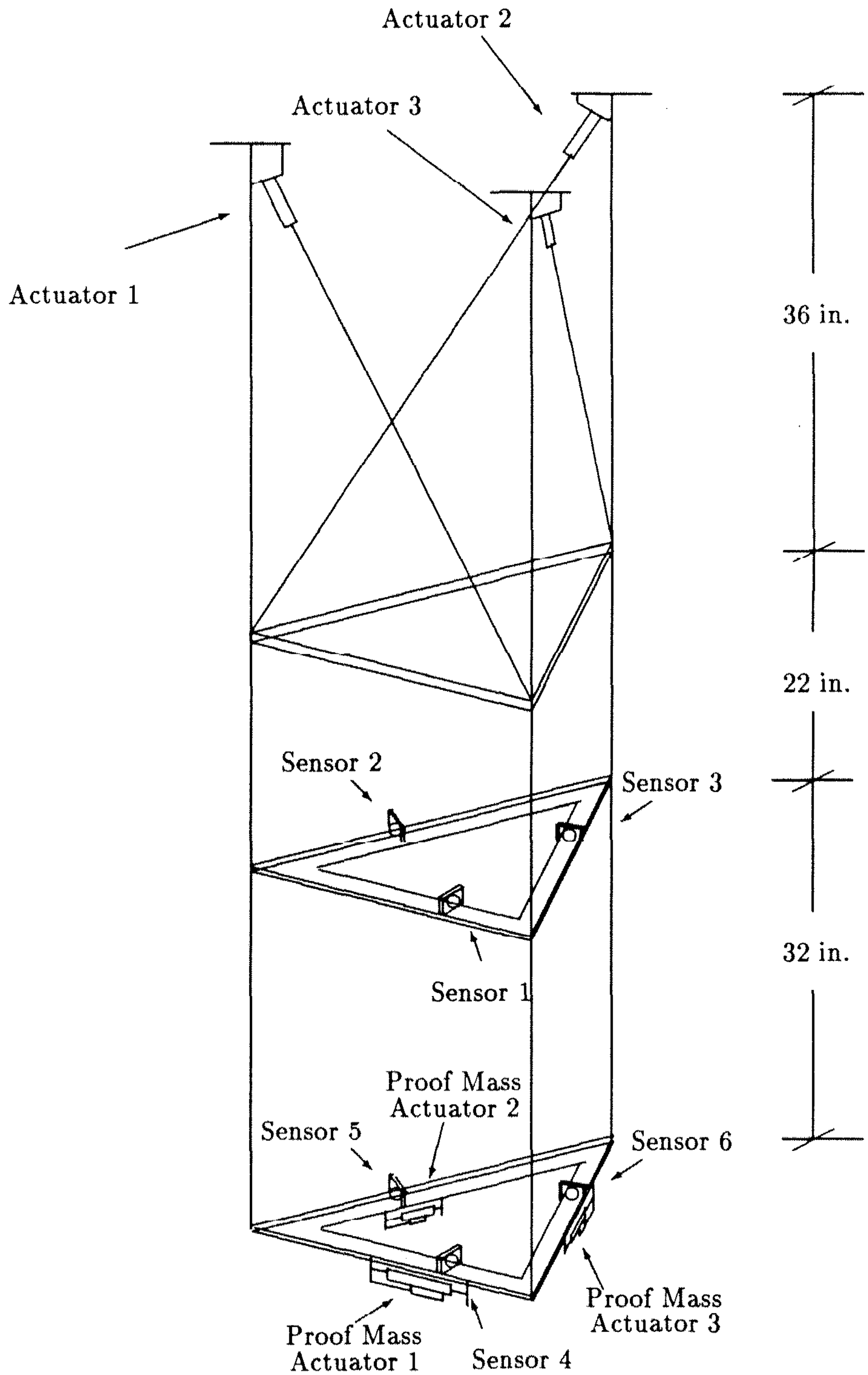

Figure 4.2: Phase II Caltech Flexible Structure

Sensor	Type	Serial Number	Sensitivity (mA/g)	(Volts/g)	(g/Volts)
1	QA1400	# 1340	1.25500	25.10	0.0398
2	QA1400	# 1343	1.25770	25.15	0.0398
3	QA1400	# 1294	1.29215	25.84	0.0387
4	QA1400	# 1338	1.29530	25.91	0.0386
5	QA700	# 1723	1.32700	26.54	0.0377
6	QA700	# 1712	1.29300	25.86	0.0387

Table 4.2: Phase II Accelerometer Scalings

actuators.

4.2.3 Proof Mass Actuators

The proof mass actuators operate on the same principles as the voice coil actuators. A set of permanent magnets are mounted on a shaft, which is surrounded by a winding of wire and a plastic sleeve. The winding and plastic casing ride on bearings along the shaft holding the permanent magnet. A drawing of these actuators is shown in figure 4.3. By passing a current through the windings, a magnetic flux is generated, producing a force. The force sets the winding and sleeve in motion relative to the shaft and magnets, with the direction of the movement depending on the polarity of the current. The movement of the windings and metal casing produces an inertial force, which is transmitted to the structure. The actuators are driven by current amplifiers from commands generated by the Masscomp computer. The proof mass actuator, LVDT sensor, and mounting frame weigh 0.57 kg (1.3 lb) of which 0.35 kg (0.8 lb) is the moving mass.

Ideally, the voltage input would be proportional to the force output. This is not the case as the strength of the permanent magnetic draws it to the LVDT case, core and its bearings, causing alignment problems and rubbing between the mounting structure and the LVDT. This leads to stiction and friction in the actuators. A parasitic effect is noticed due to the realignment of the magnetic field in the LVDT case with each oscillation. The combination of these effects result in the actuator exhibiting a nonlinear response to input excitation. A local feedback system, employing an LVDT sensor, is designed to provide centering of the actuator at low frequencies and improved linear response in the frequency range of 0.5 Hz to 8 Hz.

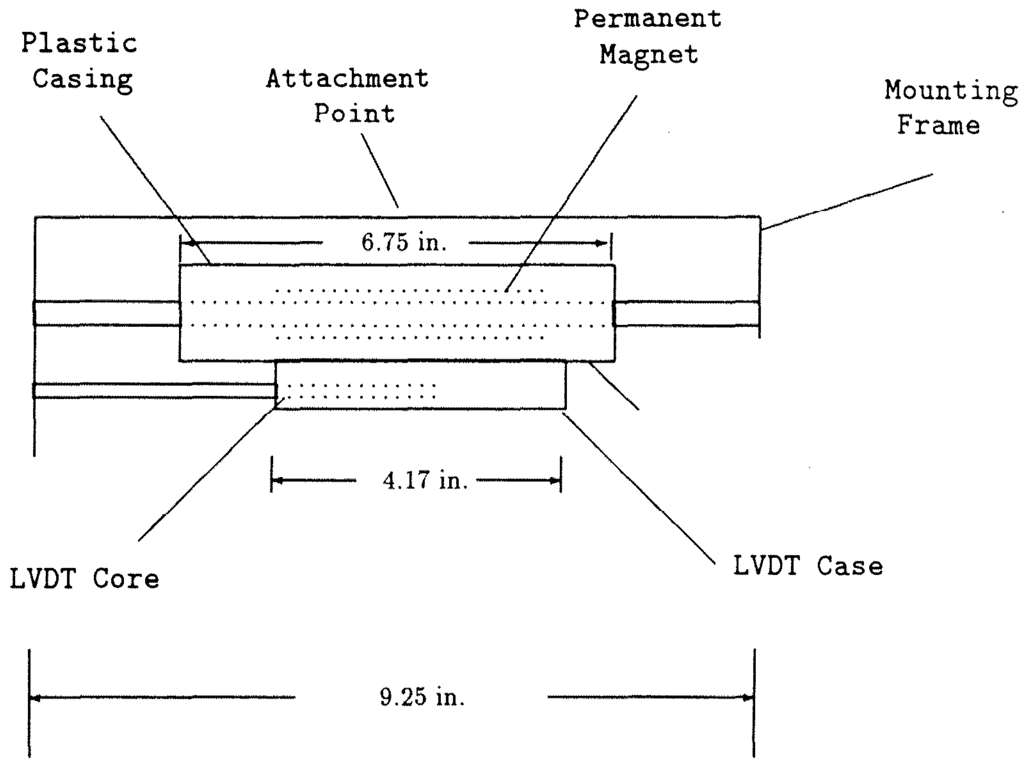

Figure 4.3: Diagram of Proof Mass Actuator

4.2.4 Proof Mass Actuator Control Laws

Experimental testing of the proof mass actuators showed a large variation in their response as a function of input signal level. Sufficiently small command signals resulted in little or no movement of the actuator mass. This is due to a sizable amount of friction/stiction between the LVDT core and its outer casing. Figure 4.4 is a plot of the input command for the first ten seconds, corresponding to a maximum input command size of 40 counts. The input signal has all its energy concentrated in the band 0.24 and 12.74 Hz, with a one pole roll off at 1 Hz. The units of displacement are in counts with 0.254 mm (0.1 in.) displacement corresponding to 0.5 volts. The proof mass actuators are limited in both output force level and stroke.

As the size of the command signal is increased, the amplitude of the response grows nonlinearly. At a critical stroke displacement, the magnetic attraction between the permanent magnetic and the bearings, located on the moving mass, is sufficient to capture

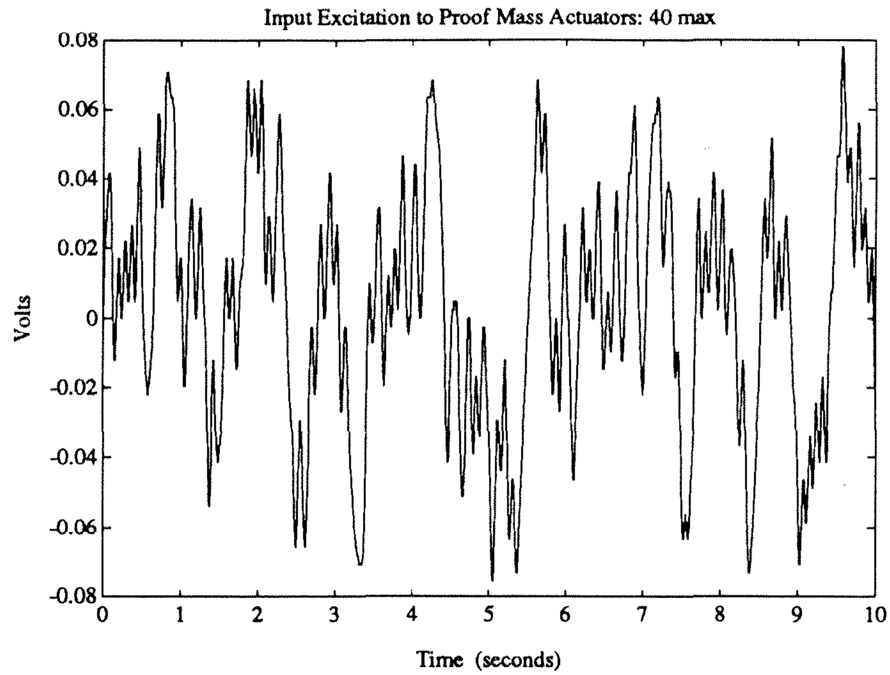

Figure 4.4: Input Excitation for Proof Mass Actuator: Maximum Peak 40

the moving mass. The moving mass is now trapped at one end of its stroke. A local control law is required to linearize the response of the actuator for several reasons: to overcome the friction/stiction associated with low velocity movements and to center the moving mass during its oscillation to avoid capture by the magnetic attraction force.

The dynamics of the system are given by

$$E = L\dot{i} + Ri + \frac{1}{C}\int i\, dt + B\dot{x} \tag{4.1}$$

$$F = m\ddot{x} + f(x, \dot{x}) \tag{4.2}$$

The input command voltage E drives a current amplifier, which supplies current to the proof mass coil. The capacitance, C, is very small and may be neglected. L is approximately 1 milliHenry and R is 0.3Ω. Current flowing through the coil creates a magnetic flux field whose direction is dependent on the polarity of the current. This flux field causes the movement of the coil and surrounding mass relative to the permanent magnetic. There is a dissipative force, due to the realignment of the magnetic field in the LVDT and bearings, which is accounted for by $B\dot{x}$. There is also a friction/stiction force due to the LVDT core rubbing on the inside of the LVDT case. The force is a function of both the velocity of the mass and position of the LVDT core relative to the LVDT case.

The nonlinear response of the proof mass actuators presents a difficult control problem. At low amplitude, the command signal needs to be large to overcome the stiction. As the amplitude of the command signal increases, so does the gain of the proof mass actuator. Therefore a pure high gain feedback loop will destabilize the system as the input command amplitude is increased. As the command signal increases, the control law needs to guard against the amplitude of response so as not to exceed the force limitations on the motor.

A nonlinear control law was developed, which amplifies signals below 40 counts with a $x^{\frac{1}{3}}$ law; and above 40 counts a linear relationship is used. The linear control law has an integrator at low frequency to center the mass with phase lead to push the bandwidth of the system out to approximately 8 Hz. The control law, developed using loop shaping methods, is

$$K_{proof\ mass} = k_i \frac{s^2 + 8s + 25}{s^2 + 100s} \tag{4.3}$$

The gain of the control law, k_i, is 20, 16, and 18 for proof mass actuator 1, 2, and 3 respectively. The closed-loop response of the proof mass actuators varies by a factor of 1.5 between 0.2 and 8 Hz, for input amplitudes varying between 0 and 360. Frequency response plots of the LVDT response to input maximum signal levels of 40 and 360 are shown in figure 4.5 and 4.6. The same input signal shown in figure 4.4 is used for each and scaled accordingly.

4.3 Modeling of Experimental Structures

A model of the structure relating input signals to system outputs is desired for control design purposes. Initially, an input/output model is developed from first principles. The model is refined for control design using system identification techniques discussed in chapter 5. Information concerning how the disturbances enter the system is useful in the control design because it can lead to better disturbance rejection properties of the closed loop system. The total control design model consists of the input/output transfer

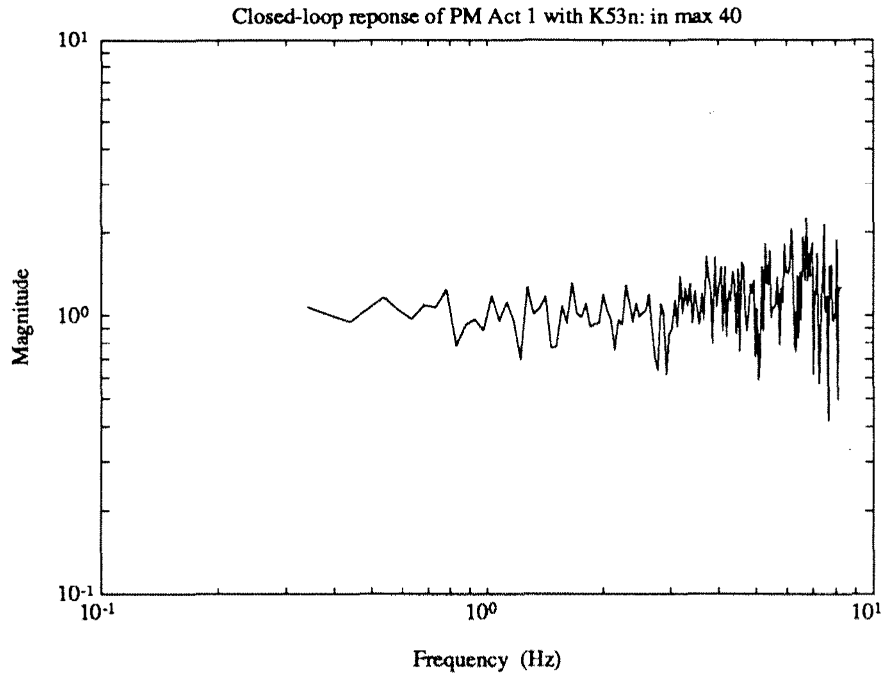

Figure 4.5: Frequency Response of Proof Mass: Input Signal Maximum Peak 40

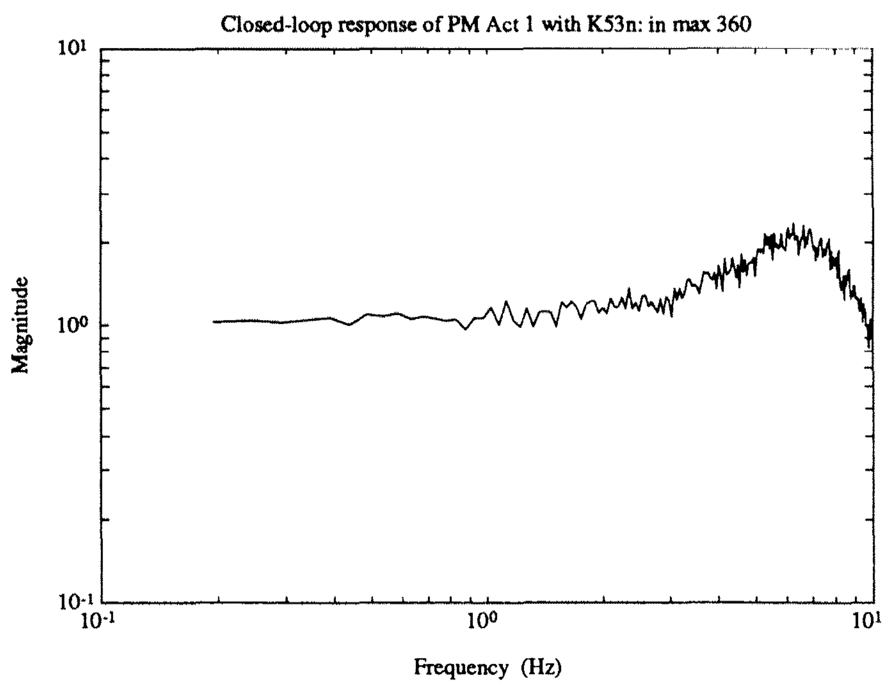

Figure 4.6: Frequency Response of Proof Mass: Input Signal Maximum Peak 360

function model from the actuator signals and disturbances to the sensors and locations of interest on the structure.

First principle models of the structures are based on the finite element method (FEM). Simply, the FEM approximates the distributed parameter system with its unlimited number of degrees of freedom by a discrete system with finite dimensionality. This is done by representing the body or structure by a collection of subdivisions or *finite elements.* A more complete description of the finite element method can be found in a number of textbooks [DesAbel, Zien].

The assumption is made that a linear model of the structure with classical modal damping is a good approximation to the actual experiment. The finite element description of the experimental structure consists of a collection of lumped masses, bar, and beam elements. The longerons and diagonals of the structure are modeled as individual elements, with displacements and rotations at the element boundaries utilized as the finite element degrees of freedom. Displacement of the longerons and diagonals are then approximated by a cubic spline function. Mass and stiffness matrices are generated from the matrix quadratic expressions, which characterize, respectively, the kinetic and potential energy of the continuous parameter system in terms of the finite degrees of freedom. The normal modes of the system are obtained by solving a generalized matrix eigenvalue problem:

$$Kx = \omega^2 Mx \tag{4.4}$$

In equation (4.4), K is the stiffness matrix, M is the mass matrix, x is the eigenvector and ω is the corresponding natural frequency.

The finite element model of the experiment provides a first approximation to the natural frequencies and mode shapes of the structure. The longerons are treated as space frame elements having three translational and three rotational degrees of freedom at each node and torsional and bending stiffnesses in two directions. The diagonals are circular bars that have the same bending stiffnesses in both directions. The longerons and diagonals are modeled as having fixed-fixed ends due to their welded end connections. All joints are modeled as rigid connections.

The accelerometers, mounting brackets, platforms and additional masses on the struc-

Mode	NASTRAN Natural Frequency (Hz)	Experimental Natural Frequency (Hz)	Damping Ratio	Mode Type
1	.991	1.17	1.8 %	1*st* bending
2	.992	1.19	1.8 %	1*st* bending
3	2.004	2.26	1.0 %	1*st* torsional
4	2.069	2.66	1.6 %	2*nd* bending
5	2.100	2.75	1.8 %	2*nd* bending
6	3.832	4.43	0.9 %	2*nd* torsional

Table 4.3: Damping Ratios and Natural Frequencies of the Phase I Experiment

ture are modeled as lumped masses. The inertia properties of each is taken into account in the finite element description. When the control system is not activated, the diagonals in the first story ride on the bearings of the voice coil actuators. No force is exerted in the open-loop configuration. The voice coil actuators are modeled as having free axial motion and as fixed in the two transverse directions. In reality, the diagonals ride on bearings that exhibit some stiction, friction, and free play. The bearings cause the damping levels to vary with the excitation amplitude. These factors lead to errors between the finite element model and the experimentally derived transfer functions. The degrees of freedom associated with vertical motion (along the longerons) are neglected in the analysis, since they correspond to high frequency modes outside the bandwidth of the current control design objectives.

4.3.1 Phase I Experimental Structure

The first six global modes are of interest for control purposes. The first group of local modes, which involve bending of the longerons, occur in the frequency range of 37 to 43 Hz. The local modes are accounted for in the control design to insure they are not destabilized. Attenuation of their vibration is not a performance criteria. Table 4.3 contains a list of natural frequencies derived from the Nastran finite element model compared with natural frequencies and damping derived from experimental data.

Scalings associated with the actuators and sensors are included in the transfer function models to correlate the Nastran model with the experimental data. Each voice coil actuator has a scaling of 0.27 kg/volt (0.59 lb/volt), i.e., one volt produces 0.27 kg (0.59

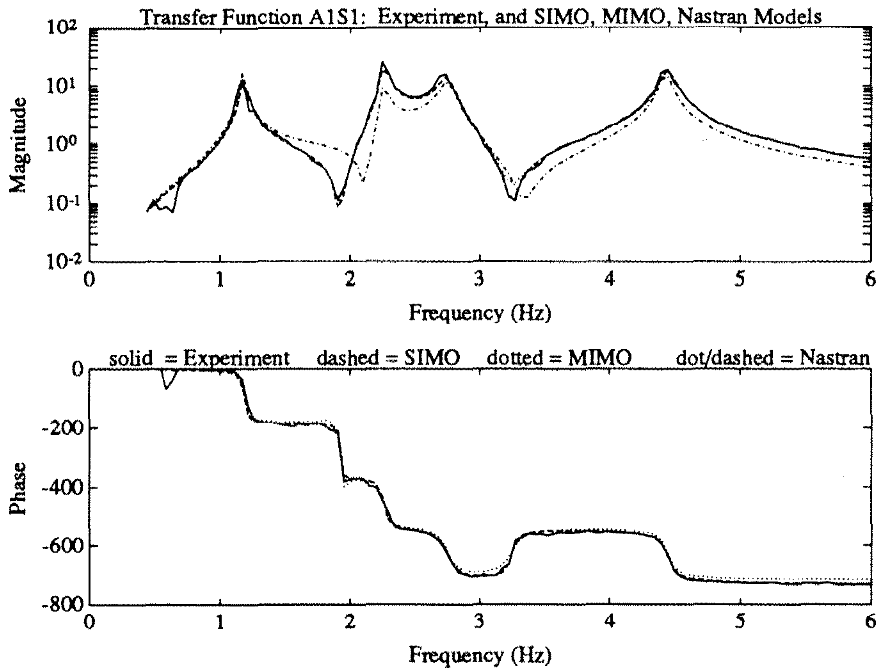

Figure 4.7: A Comparison Between the Experimental Data, Nastran and Identified Model for A1S1

lb) of force. The accelerometers are designed to output a prescribed current level for a one-g acceleration. Each of the three sensors has a 50.2 $K\Omega$ resistor in-line to scale the acceleration levels to approximately 0.016 g per volt. Appendix A contains a state space description of the phase I model.

A multi-input/multi-output (MIMO) transfer function model is derived from the Nastran modal coefficients of the first six modes. Due to significant variation between the experiment and FEM in the natural frequencies, the model uses the natural frequencies and damping levels derived from experimental tests. The variation in the natural frequencies is believed to be caused by two phenomena: the wires connected to the accelerometer were tightly fixed to the columns and pulled taunt, thereby adding stiffness to the longerons, and stiction/friction associated with the voice coil actuators, leading to nonlinear behavior. A comparison between the finite element and experimentally derived transfer functions is shown in figure 4.7 and 4.8.

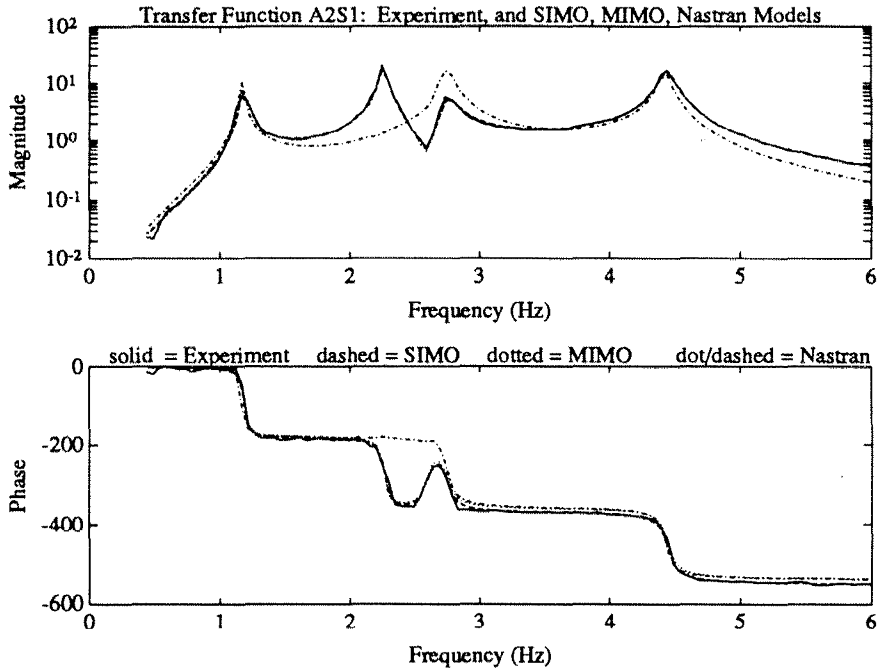

Figure 4.8: A Comparison Between the Experimental Data, Nastran and Identified Model for A2S1

4.3.2 Phase II Experimental Structure

The first nine global modes, between 0.90 and 6.3 Hz, of the structure are of interest for control purposes. The first group of local modes occur in the frequency range of 37 to 43 Hz, corresponding to the same modes as in the phase I experiment. Table 4.4 contains a list of natural frequencies derived from the Nastran FEM and the natural frequencies and damping values derived from experimental data.

Based on experience from the phase I experiment, the finite element model is of little use for control design due to its variation from the experimental data. An identified model developed with system identification techniques presented in the next chapter is used for control design purposes. Appendix B contains the state space model developed for the phase II structure along with transfer function plots of the experimental data versus the identified model for select actuators and sensors.

Mode	NASTRAN Natural Frequency (Hz)	Experimental Natural Frequency (Hz)	Damping Ratio	Mode Type
1	0.76	0.90	0.62 %	$1st$ bending
2	0.76	0.92	0.82 %	$1st$ bending
3	1.84	1.62	1.39 %	$1st$ torsional
4	1.73	2.21	1.21 %	$2nd$ bending
5	1.73	2.29	1.22 %	$2nd$ bending
6	3.40	3.60	1.84 %	$2nd$ torsional
7	4.14	3.94	0.74 %	$3rd$ bending
8	4.14	3.97	0.64 %	$3rd$ bending
9	8.21	6.30	0.96 %	$3rd$ torsional

Table 4.4: Damping Ratios and Natural Frequencies of the Phase II Experiment

4.4 Real Time Control Implementation

The control designs are implemented on the Caltech flexible structure via a 5400 Masscomp computer. The real time control program implements a 3 input/3 output control law at 200 Hz and generates disturbance commands for the 3 air actuators for the phase I structure. The computer speed is such that a 60^{th} order control law, in modal coordinates, can be implemented. The system has a 12 bit A/D converter with a range of $\pm$ 5 volts, .00244 volts per bit, and a 12 bit D/A converter with a range of $\pm$ 5 volts. The noise associated with the computer is $\pm$ 1 lsb (least significant bit). The Masscomp computer is entirely dedicated to the closed-loop experiment during real time implementation of the control law.

A block diagram of the phase I experimental setup is shown in figure 4.9. A disturbance excites the structure, causing the first and second story platform to vibrate. This, in turn, generates accelerations that are measured by the sensors. These signals are filtered by a 100 Hz, 4^{th} order Butterworth filter and input to the Masscomp via the A/D board. The control algorithm operates on these signals and generates force commands for the actuators, which are transmitted to the actuator via the D/A converter. These signals are voltage levels corresponding to actuator force levels. The voltage is input to a current amplifier, which drives the voice coil actuators. Now both the actuator command, which is trying to suppress the vibration, and the disturbance excitation affect the vibration of the second story platform. This cycle is continued throughout the implementation of the closed-loop experiment.

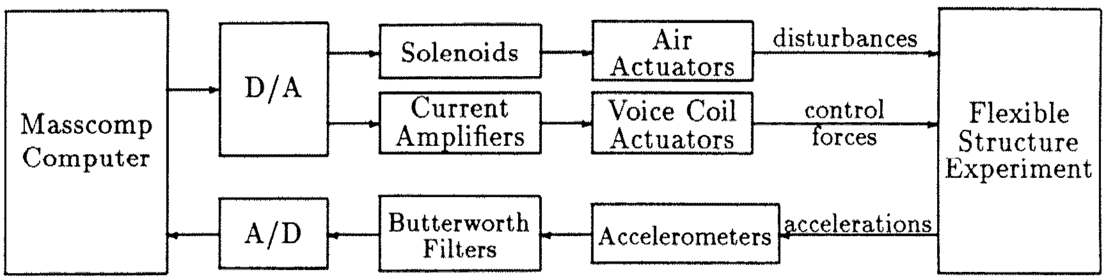

Figure 4.9: Block Diagram of Experimental Setup for the Phase I Experiment

Chapter 5

System Identification of Flexible Structure Experiment

The objective of the Caltech flexible structure is to address active control issues in vibration suppression of flexible structures. A number of different research objectives dictate the use of an accurate transfer function model description of the structure. The finite element models were deemed insufficient due to their deviation from the experimental data. Therefore, system identification techniques are used to develop more accurate multivariable descriptions of the structure.

This chapter discusses the application of system identification techniques to the phase I experimental structure. These methods are applied to the phase II structure but will not be discussed. Chebyshev polynomials are employed to fit phase I experimental data with three single-input/multi-output (SIMO) transfer function models. Combining these leads to a multivariable model with 12 modes versus six in the original finite element model in the frequency range of interest. An ad hoc model reduction technique, based on *a priori* knowledge of the structural system and singular value decomposition methods, is used to develop a multivariable system description with six modes. This approach is compared with balanced realization model reduction techniques, which take no advantage of *a priori* knowledge. Uncertainty descriptions are developed for these models to account for their variation from experimental results. All references are with respect to the phase I structure unless otherwise noted.

5.1 Chebyshev Polynomial Curve Fitting

Chebyshev polynomials have been used previously in FFT signal analyzers to curve fit measured transfer function data of single input/single output systems [Adcock]. This technique was extended to SIMO systems and applied successfully to experimental data [DailLuk2]. The same method is employed to develop SIMO transfer function models of the Caltech flexible structure experiment. A multi-input/multi-output (MIMO) model is derived from the sum of the individual SIMO models.

The transfer function equation,

$$g(s) = \frac{n(s)}{d(s)} = \frac{n_0 + n_1 s + n_2 s^2 + \cdots + n_N s^N}{d_0 + d_1 s + d_2 s^2 + \cdots + d_N s^N} \tag{5.1}$$

which is nonlinear in the coefficients, is transformed into a linear equation by multiplying through by the denominator, $g(s)d(s) - n(s) = 0$. The transfer function data is a set of complex numbers, $g(\jmath\omega)$, at various frequency points, ω. Separating this equation into real and imaginary parts, two real equations are produced for each value of ω. Written in matrix form, they form a linear least squares problem, with the real vector, x, containing the polynomial coefficients of $n(s)$ and $d(s)$.

A problem with this approach is that the matrix $\hat{A}$ is ill-conditioned. This is due to the ratio of $n(s)/d(s)$ being very sensitive to small changes in their coefficients. To alleviated this problem, the numerator and denominator are written as sums of Chebyshev polynomials and, therefore, indirectly as sums of powers of s, where s is define $\jmath\omega$ [Adcock]. SISO rational Chebyshev approximation provides a more robust method than powers of s for estimating the numerator and denominator coefficients of a transfer function from frequency domain data. The Chebyshev polynomials in ω are bounded by ± 1 on the interval $\omega \in [0, 1]$ and have contrasting shapes, unlike the powers of ω, which remain close to 0 over most of the interval. In practice the largest value of ω, taken to be the maximum frequency point in the data, is normalized to 1. The diversity of the Chebyshev polynomials leads to a less sensitive formulation of the curve fitting problem. A comparison of the first four Chebyshev polynomials and powers of ω are shown in figure 5.1.

The first several Chebyshev polynomials, ψ_i, are:

$$\psi_0(\omega) = 1, \quad \psi_1(\omega) = \omega, \quad \psi_2(\omega) = 2\omega^2 - 1, \quad \psi_3(\omega) = 4\omega^3 - 3\omega, \quad \psi_4(\omega) = 8\omega^4 - 8\omega^2 - 1 \tag{5.2}$$

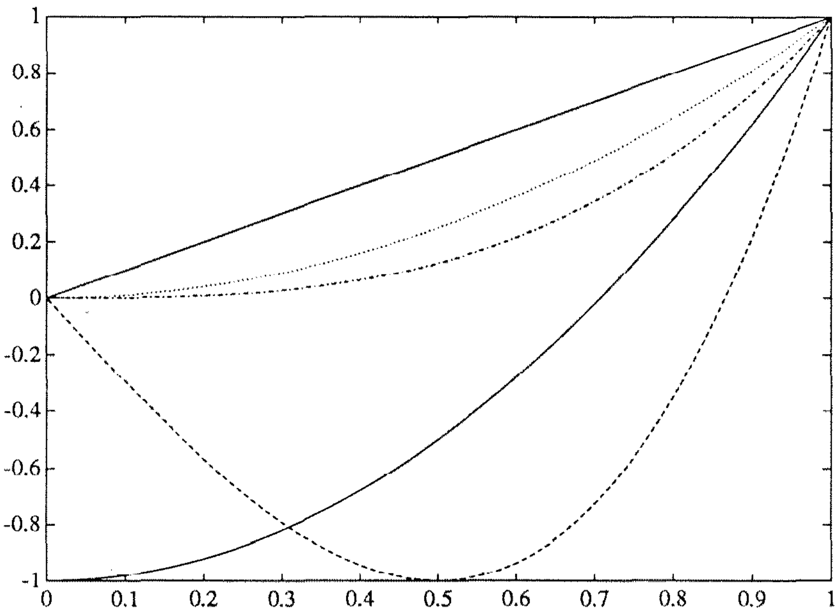

Figure 5.1: The First Four Power and Chebyshev Polynominals between 0 and 1

and can be generated by the recursive formula

$$\psi_i(\omega) = 2\omega\psi_{i-1}(\omega) - \psi_{i-2}(\omega) \qquad where \quad \psi_0 = 1, \quad \psi_1 = \omega \tag{5.3}$$

In the phase I SIMO experimental transfer functions, four dominant modes of the system are observed in the frequency range of 0.5 to 5.5 Hz (3.1 to 34.5 rad/s). Therefore, an eighth order Chebyshev polynomial is used to fit the data.

The numerator, $n(s)$, and denominator, $d(s)$, can be written as the sum of Chebyshev polynomials,

$$\begin{aligned} n(\jmath\omega) &= \textstyle\sum_{k\ even} n_k\psi_k(\omega) + \jmath\sum_{k\ odd} n_k\psi_k(\omega) \\ d(\jmath\omega) &= \textstyle\sum_{k\ even} d_k\psi_k(\omega) + \jmath\sum_{k\ odd} d_k\psi_k(\omega) \end{aligned} \tag{5.4}$$

The transfer function data, $g(\jmath\omega)$, can be described by its real and imaginary parts, $g(\jmath\omega) = g_r(\omega) + \jmath g_i(\omega)$ with a matrix equation formed from the real and imaginary parts of the equation $g(\jmath\omega)d(\jmath\omega) - n(\jmath\omega) = 0$.

$$\begin{bmatrix} g_r\psi_0 & -g_i\psi_1 & g_r\psi_2 & -g_i\psi_3 & \dots \\ g_i\psi_0 & g_r\psi_1 & g_i\psi_2 & g_r\psi_3 & \dots \end{bmatrix} \begin{bmatrix} d_0 \\ d_1 \\ d_2 \\ \vdots \end{bmatrix} - \begin{bmatrix} \psi_0 & 0 & \psi_2 & 0 & \dots \\ 0 & \psi_1 & 0 & \psi_3 & \dots \end{bmatrix} \begin{bmatrix} n_0 \\ n_1 \\ n_2 \\ \vdots \end{bmatrix} = \begin{bmatrix} 0 \\ 0 \end{bmatrix} \tag{5.5}$$

At each frequency point ω , the equation $g(j\omega)d(j\omega) - n(j\omega)$ contributes two rows to the matrix $\hat{A}$. The individual frequency points can be weighted to trade off the accuracy of the fit in different frequency ranges. Each row is normalized by $\mid g(j\omega)d(j\omega) \mid$, using an estimated $d(j\omega)$ to achieve a constant relative accuracy (in log magnitude and phase) at each frequency.

The matrix $\hat{A}$ has two rows for each frequency point ω and $2N$ columns, where N is the degree of the denominator, $d(s)$. To save storage space, one can form the $2N \times 2N$ product $A = \hat{A}^T \hat{A}$, then solve the equation $\inf_{||x||=1} ||Ax||$ using the singular value decomposition (SVD) or a routine to find the smallest eigenvalue-eigenvector pair. The subblocks of A involve products of the form $\Psi\Psi^T$, where $\Psi = [\psi_0 \ \psi_1 \ \psi_2 \ldots \psi_N]^T$. The recursive formula $2\psi_i\psi_j = \psi_{i+j} + \psi_{i-j}$ is used to form $\Psi\Psi^T$, greatly reducing the number of multiplications required. The $(i,j)^{th}$ element of this matrix is given by $[2\Psi\Psi^T]_{ij} = \psi_{i+j+2} + \psi_{|i-j|}$.

The algorithm used to fit the data with Chebyshev polynomials is as follows [Dail-Luk2] :

1. Read in data points, $g(j\omega)$, and associated weights
2. Construct $A = \hat{A}^T \hat{A}$
3. Solve for x to minimize $x^T Ax$
4. Use x to build $d(j\omega)$, $n(j\omega)$
5. Use $\mid g(j\omega)d(j\omega) \mid^{-1}$ as a weight, cycle back to Step 2
6. When the process converges, compute the state space realization of $n(s)/d(s)$

For the SIMO case, the denominator has the same dynamics as in the SISO case. Therefore, by extending the number of numerator coefficients, $n(s)$, one can address the SIMO case in a fashion similar to the SISO case. One problem with the Chebyshev curve fitting method is that it does not guarantee that a stable transfer function will be fit to the raw data. However, given that the frequency domain data reflects a stable system, and the polynomial approximation is a good fit to the data, the stability properties of the two are usually comparable. This was not an issue in fitting the experimental data for the phase I structure, but was a problem for the phase II structure. Once the single input/multi-output transfer functions are fit with Chebyshev polynomials, the models are converted to a state space description.

For the phase I experimental structure, the Chebyshev polynomial SIMO curve fitting technique is used to develop three SIMO transfer function models to describe the 3-input/3-output experimental structure. A MIMO model is constructed from the 3 SIMO models. It contains 12 modes (24 states), though only six modes (12 states) are present in the experimental data. A technique for model reduction based on *a priori* knowledge of the flexible structure is developed using SVD.

Performing system identification using curve fitting techniques is not the optimal method for lightly damped, flexible structures. These structures can often be modeled accurately by stable, second-order systems and the identification process should take advantage of this knowledge. A shortcoming of the Chebyshev technique is that it uses no *a priori* knowledge of the system dynamics. Identification of flexible structures is an area of enormous research and the results presented represent only the methods used to derive multivariable transfer function models of the Caltech flexible structure experiments for control design.

5.2 MIMO Transfer Function Model

A multivariable transfer function model is constructed from the individual SIMO models. This model has the same number of states as the sum of each SIMO model, which leads to a redundant number of states in the MIMO model that are not physically motivated. An SVD model reduction technique, based on an *a priori* model of the system, is developed to produce a MIMO transfer function model of the same order as the finite element model. The Chebyshev polynomial curve fitting and SVD based model reduction techniques are used in sequence to form a transfer function model of the experimental structure.

Based on the finite element model and physical data, the phase I experimental structure has only six natural frequencies and mode shapes between 0.5 to 5.5 Hz. This is the frequency range in which an accurate multivariable model of the structure is desired for control design. The SIMO Chebyshev curve fitting technique is used to develop transfer function models from each voice coil actuator to the three accelerometer sensors. These models contribute 4 modes to the total system model for each input. Although all six modes are excited by each actuator, only four modes appear distinctly in each channel of the experimental data. This is due to the two and second bending modes having nearly identical natural frequency. After fitting the individual SIMO transfer functions, the 3-input/3-output transfer function model is comprised of 12 modes. One would like to take advantage of the physical knowledge about the problem to reduce the 12 mode model to a 6 mode model.

5.3 Ad Hoc Model Reduction Technique

An ad hoc model reduction technique is developed using *a priori* knowledge of the flexible structure experiment. Modes in the SIMO models are grouped together based on their natural frequencies. Four groups of modes are defined in the frequency range of interest for the phase I structure. These groups include the first bending modes, first torsional mode, second bending modes, and the second torsional mode. The SVD method is used to reduce the number of modes present in the Chebyshev MIMO model, to six physically motivated modes.

The experimental structure has two first bending and second bending modes present in the frequency range of interest. The two modes associated with the first bending mode have approximately the same natural frequency as do the second bending modes. Although the bending modes have similar natural frequencies, their mode shape are perpendicular to one another. In the individual transfer functions, it is hard to differentiate between the individual bending modes with similar natural frequencies. Therefore, when fitting the Chebyshev polynomial models to the experimental data, the first and second bending modes are treated as having only one mode each. Each SIMO model consists of one first bending mode, a first torsional mode, a second bending mode and a second torsional mode.

Combining the SIMO Chebyshev polynomial transfer function models for actuator 1 and 2, a 2 input, 3 output 8 mode model is formed. Because there are two first and second bending modes, the coefficients associated with both the first and second bending modes remain in the model. This model contains two modes that are not physically motivated. It is found that each torsional mode in the 8 mode model has two nearly identical natural frequencies associated with it, accounting for the two extra modes. The extra modes are due to the torsional response showing up predominantly in both sets of transfer functions from actuators 1 and 2 to the three sensors. From the physics of the problem, there is only one mode associated with each torsional natural frequency. A common, one mode model for each torsional mode needs to be unraveled from the two SIMO transfer function models. To see how this might be done, a modal description of the experimental structure is constructed.

The voice coil actuators input a force to the structure and accelerations are measured. Assuming modal damping, a SISO transfer function model relating force input to acceleration output can be developed for each mode. For the i^{th} mode, it has the form:

$$\frac{b_i c_i s^2}{s^2 + 2\zeta_i \omega_i s + \omega_i^2} \tag{5.6}$$

Rewriting the transfer function in strictly proper form yields

$$b_i c_i - \frac{2s\zeta_i \omega_i b_i c_i + \omega_i^2 b_i c_i}{s^2 + 2\zeta_i \omega_i s + \omega_i^2} \tag{5.7}$$

The coefficients $b_i c_i$, ζ_i and ω_i are determined from the Chebyshev polynominal models. One will notice that only the combined scalar $b_i c_i$ can be determined uniquely. Unfortunately, this does not allow for the identification of the individual modal coefficients b_i and c_i associated with each mode. However, the identified coefficients are within a scalar transformation of the modal coefficients.

Each SISO transfer function model developed from the experimental structure consists of 4 individual modes, which can be written as the sum of distinct modal components:

$$TF_{actuator \rightarrow sensor} = \sum_{i=1}^{4} \frac{b_i c_i s^2}{s^2 + 2\zeta_i \omega_i s + \omega_i^2} \tag{5.8}$$

Transfer functions, written in state space form, are described by

$$G(s) = \left[\begin{array}{c|c} A & B \\ \hline C & D \end{array}\right] \doteq D + C(sI - A)^{-1}B \tag{5.9}$$

with the constant part, D, given by

$$D_{actuator \rightarrow sensor} = \sum_{i=1}^{4} b_i c_i \tag{5.10}$$

The D term derived from curve fitting is often inaccurate, because it is outside the frequency range in which the data was fit. Therefore, it cannot be used to determine the individual $b_i c_i$ components.

One way to determine each component from the curve fitting data is to replace s by $\jmath\omega$ and evaluate the strictly proper transfer function associated with each individual mode at $\omega = 0$. Consider an individual mode of an identified SISO transfer function, $\tilde{G}(s)$, whose state space representation is of the form

$$\begin{aligned} \tilde{G}(s) &= \left[\begin{array}{cc|c} 0 & 1 & 0 \\ -\omega_i^2 & -2\zeta_i\omega_i & b_i \\ \hline -c_i\omega_i^2 & -2c_i\zeta_i\omega_i & d_i \end{array}\right] \\ &= d_i - \frac{2s\zeta_i\omega_i b_i c_i + \omega_i^2 b_i c_i}{s^2 + 2\zeta_i\omega_i s + \omega_i^2} \end{aligned} \tag{5.11}$$

Evaluating this equation at $\omega = 0$, scaling A by -1 and disregarding the d_i component, leads to

$$\tilde{G}(0) = C(A)^{-1}B = \begin{bmatrix} c_i\omega_i^2 & 2c_i\zeta_i\omega_i \end{bmatrix} \begin{bmatrix} 0 & 1 \\ -\omega_i^2 & -2\zeta_i\omega_i \end{bmatrix}^{-1} \begin{bmatrix} 0 \\ b_i \end{bmatrix} = b_i c_i \tag{5.12}$$

The individual modal components, $b_i c_i$, can be determined for each mode with this method. The same idea can be applied to multiple input and output pairs with a single mode. Instead of a scalar, $b_i c_i$, two vectors B_i and C_i are determined. Note vectors B_i and C_i are not unique. The multi-input/output technique makes use of the singular value decomposition. In the phase I experiment, it is known that there are only one or two modes present in the data at each modal natural frequency. The two first bending modes have close natural frequencies, one first torsional, two second bending modes with close natural frequencies and one second torsional mode. Individual modes can be identified using this information, an SVD of the matrix is performed and the dominant mode is kept for the torsional case and two are kept for the bending cases. For one mode, the maximum singular value and its associated right and left singular vectors determine B_i and C_i. For n modes, the n singular values, the largest and their associated right and left singular vectors, would determine B_i and C_i.

The singular value decomposition for an $n \times m$ matrix A [HornJ], is given by

$$A = U\Sigma V^* = \sum_{i=1}^{K} \sigma_i(A) u_i v_i^* \tag{5.13}$$

where U and V are unitary matrices with column vectors denoted by

$$U = (u_1, u_2, \ldots, u_n) \quad and \quad V = (v_1, v_2, \ldots, v_m) \tag{5.14}$$

Σ contains a diagonal nonnegative definite matrix Σ_1 of singular values arranged in descending order as in

$$\Sigma = \begin{pmatrix} \Sigma_1 \\ 0 \end{pmatrix}, \quad n \geq m; \qquad \Sigma = (\Sigma_1 \;\; 0), \quad n \leq m \tag{5.15}$$

with

$$\Sigma_1 = diag[\sigma_1, \sigma_2, \ldots, \sigma_K]; \quad K = \min(m, n) \quad and \quad \sigma_1 \geq \sigma_2 \geq \ldots \geq \sigma_K \tag{5.16}$$

The C_i vector, corresponding to the output direction of the mode, is constructed from the maximum singular value and the unitary U matrix. For a single mode, the C_i vector is given by $C_i = \sigma_1 u_1$, where C_i is a vector of the length of the number of outputs. The B_i vector, constructed from the V matrix, is given by $B_i^T = v_1$, which is the right singular vector associated with the maximum singular value. The matrix $B_i^T C_i$ has the corresponding $b_i c_j$ matrix elements associated with input i and output j. For multiple modes, the B_i and C_i vectors are of size (number of modes) $\times$ (number of inputs) and (number of outputs) $\times$ (number of modes) respectively.

This approach is used to transform the 3 input, 3 output, 12 mode model of the phase I structure, developed from Chebyshev polynomials, into a 3 input, 3 output, six mode model that agrees with the predicted properties of the structure in the frequency range of interest. The three SIMO transfer function models have 3 modes describing the first bending modes, 3 modes for the first torsional mode, 3 modes describing the second bending modes, and 3 modes for the second torsional mode. Applying the SVD based reduction method to each modal group led to the development of a six mode MIMO transfer function model of the experimental flexible structure with two first bending modes, a first torsional mode, two second bending modes, and a second torsional mode.

The six mode MIMO model developed using the ad hoc model reduction technique matches the original 12 mode Chebyshev model very well. There are some small differences in the Bode magnitude plots of the transfer functions associated with sensor 3. Presented in figures 5.2, 5.3, and 5.4 is a comparison among the Bode plots of the transfer

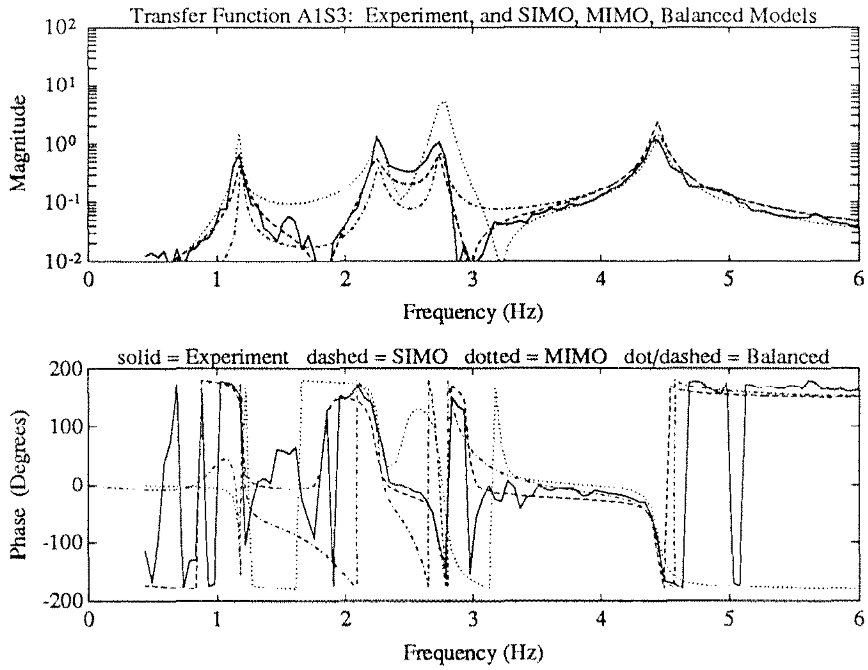

Figure 5.2: Phase I Experimental Bode Plot, **SIMO**, **MIMO** and Balanced Models of A1S3

functions from: (a) The experimental data, (b) the SIMO Chebyshev polynomial model method, and (c) the six mode MIMO method derived using the techniques described above. The frequency range of interest for fitting of the Chebyshev polynomial model is between 0.5 and 5.5 Hz (3.14 and 35 rad/s).

5.4 Balanced Model Reduction

The method of model reduction based on balancing is applied to the 12 mode MIMO model constructed from the three Chebyshev SIMO models. The objective is the same as before, to obtain a six mode model from the Chebyshev MIMO 12 mode model. This method requires no physical knowledge of the system it is trying to approximate.

The balanced model reduction technique computes an m^{th} order reduced model

$$G_m \;=\; C_m(sI - A_m)^{-1}B_m \;+\; D_m \tag{5.17}$$

of a possibly non-minimal n^{th} order system

$$G \;=\; C(sI - A)^{-1}B \;+\; D \tag{5.18}$$

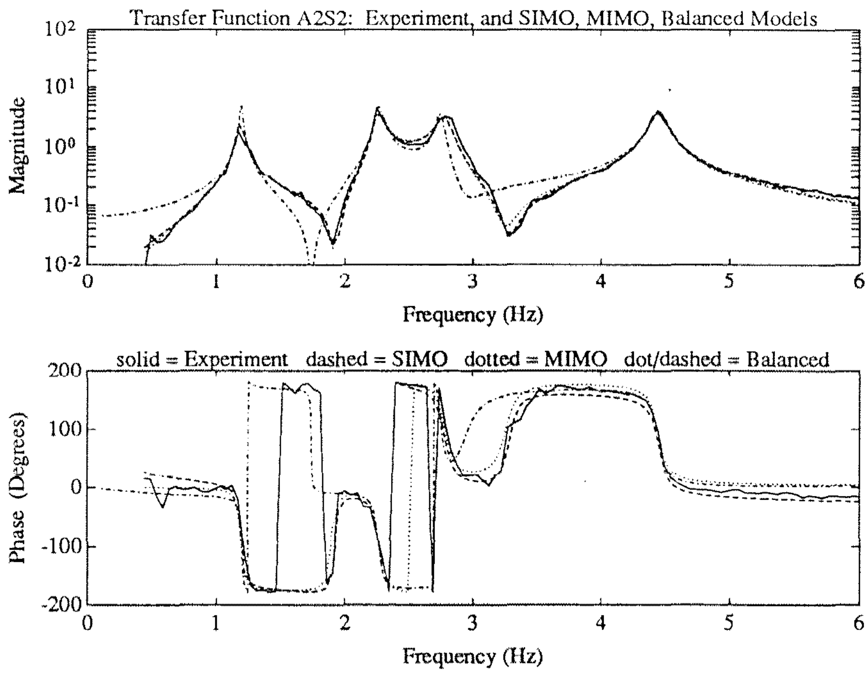

Figure 5.3: Phase I Experimental Bode Plot, **SIMO**, **MIMO** and Balanced Models of A2S2

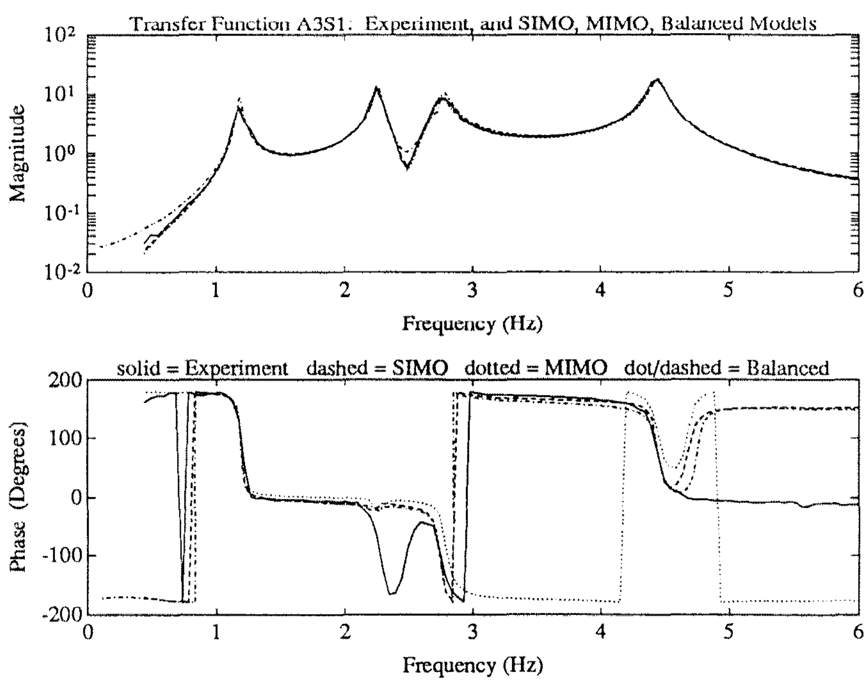

Figure 5.4: Phase I Experimental Bode Plot, **SIMO**, **MIMO** and Balanced Models of A3S1

such that

$$\|G(\jmath\omega) - G_m(\jmath\omega)\|_\infty \;\leq\; 2 \sum_{i\,=\,m+1}^{n} \sigma(i) \tag{5.19}$$

where $\sigma(i)$ are the square-roots of the eigenvalues of the controllability and observability grammians. These are also the Hankel singular values of $G(s)$ [Glov1, Moore, Enns].

A 6 mode MIMO model is developed using this technique. The reduced order transfer function model matches the original 12 mode MIMO model quite well and the natural frequencies and damping values closely match those in the Chebyshev model. The corresponding Bode plot functions are shown in figures 5.2, 5.3, and 5.4 and are compared therein to those from the Chebyshev models and the experimental data.

5.5 Experimental Data and Models

Three different multivariable models are developed for the phase I experimental data in the frequency range of interest. The first model, **SIMO**, is the Chebyshev SIMO transfer function model for each actuator input. A 12 mode MIMO model is developed by combining the three Chebyshev SIMO models. The second model, **MIMO**, is the reduced, six mode MIMO transfer function model formed using the ad hoc model reduction technique. The third model, **Balanced**, is a six mode MIMO model formed by applying balanced model reduction to the Chebyshev SIMO transfer function models.

As one would expect, the Chebyshev SIMO models provide the best fit to the experimental data. This is due to the other two models approximating the Chebyshev model. The poorest fit occurs in the Bode plot representing the transfer function between actuator 1 and sensor 3. Because actuator 1 excites the direction perpendicular to sensor 3, the magnitude of the transfer function is an order of magnitude below that of the other actuator 1 transfer functions. The curve fitting technique applies a maximum magnitude error criteria to fit the data, which accounts for this discrepancy.

The ad hoc technique is used to develop a six mode, multivariable model that fits the experimental data well except from actuator 1 to sensor 3. The balanced model reduction also fits the data well, with the notable exception of the Bode plots associated with the transfer functions of A2S2 and A1S3. The balanced model transfer function from actuator 2 to sensor 2 has problems with the interlacing of the poles and zeros associated with the second bending modes. Overall, the balanced model reduction method performed quite well considering it had no knowledge of the dynamic characteristics of the system. The ad hoc technique produced the best six mode model corresponding to the experimental data and is the control design model for the phase I experimental structure. A state-space description of the model used in control design is given in Appendix A. These same techniques are applied to the phase II experimental structure to generate a control design model.

5.6 Phase II Experimental Structure

The Chebyshev curve fitting techniques are similarly applied to the phase II flexible structure. This experiment represents a much more difficult identification problem. There are nine flexible modes between 0.90 Hz and 6.3 Hz. The lightest damped mode has on the order of 0.2% damping with the highest damping level at approximately 1.8%. Three sets of bending modes, which have two modes practically coalested, make the identification process difficult. A single-input/three-output model is desired from each actuator to the three accelerometers on bay 3. In several of the accelerometer transfer functions, eight of the nine natural frequencies of the structure are present, causing the Chebyshev curve fitting method to have difficulties fitting lightly damped modes. It may be due to the limited amount of frequency information for each mode.

Two sets of multivariable models are developed for the phase II structure. One set of models is formulated for the voice coil actuators as inputs, and the other using the proof mass actuators as inputs. A plot of the transfer functions between the voice coil actuator 1 and sensors 4 and 5 are shown in figures 5.5 and 5.6. Plots of the transfer function between proof mass actuator 1 and sensors 4 and 5 are shown in figures 5.7 and 5.8. A state-space description of the two phase II models and a more complete set of experimental transfer functions is provided in appendix B.

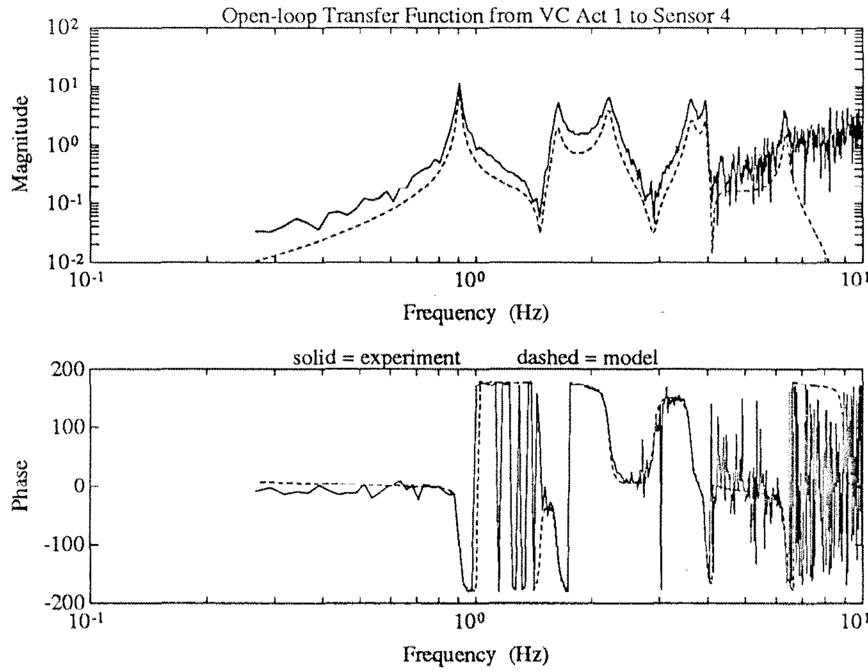

Figure 5.5: Phase II Experimental Bode Plot and SIMO Model of Voice Coil Actuator 1 to Sensor 4

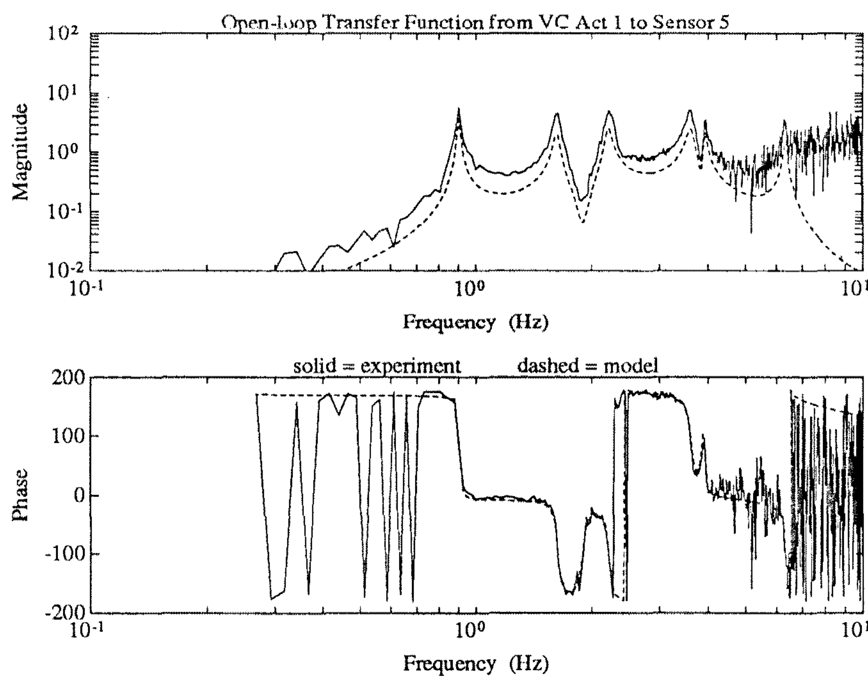

Figure 5.6: Phase II Experimental Bode Plot and SIMO Model of Voice Coil Actuator 1 to Sensor 5

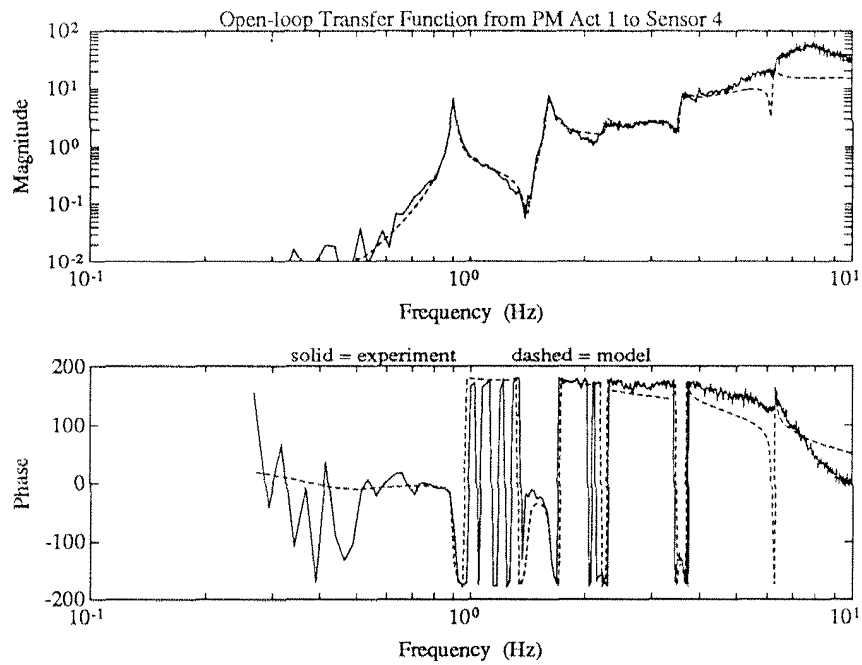

Figure 5.7: Phase II Experimental Bode Plot and SIMO Model of Proof Mass Actuator 1 to Sensor 4

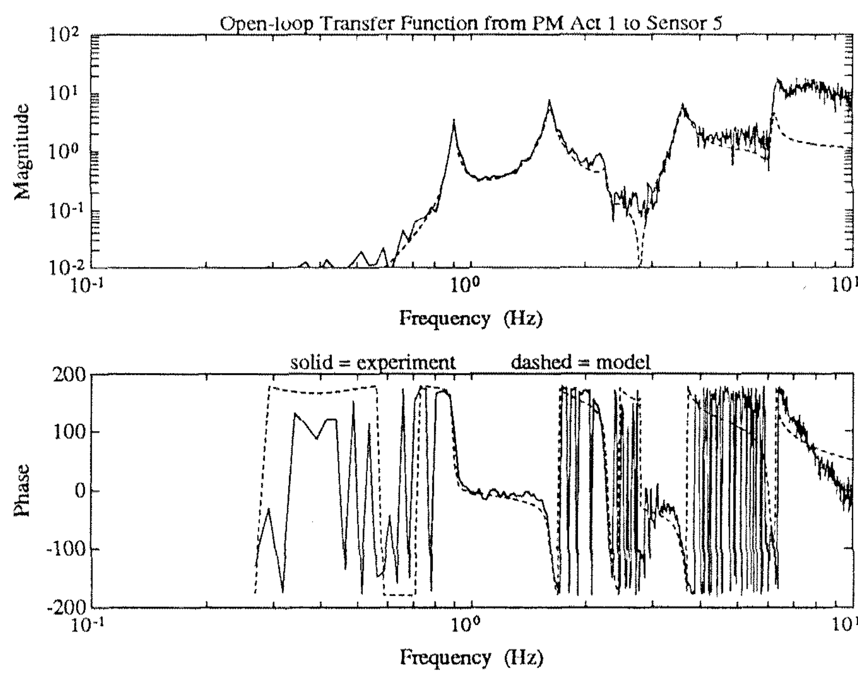

Figure 5.8: Phase II Experimental Bode Plot and SIMO Model of Proof Mass Actuator 1 to Sensor 5

Chapter 6

Uncertainty Modeling for Flexible Structures

The μ-framework requires the nominal structural transfer function model to be formulated as a linear time invariant (LTI) system. Though, this model might describe the physical system accurately, any model is only an approximation of the physical system. There is always some "uncertainty" present even when the underlying process is essentially linear. This can be due to the physical parameters not being known exactly, high frequency dynamics being neglected, or invalid assumptions made in the model formulation. These inaccuracies can be described in numerous ways, such as: bounds on the parameters of a linear model, bounds on the nonlinearities, and frequency domain bounds on transfer function models. One needs to account for the variation between the mathematical model and the "real" system in the control design.

Uncertainty descriptions determine the tradeoff between achievable performance and robustness of the control design. A control design synthesized for a physical system not within the set of plants described by the nominal and uncertainty models may be unstable or exhibit poor performance when implemented on the actual system. However, if the uncertainty descriptions are overly conservative, system descriptions may be included in the set, which severly limit the performance of the closed-loop system. Therefore, tight uncertainty bounds are required to synthesize robust control designs that achieve high performance when implemented on the actual system.

A variety of uncertainty descriptions are available to the control designer. Two types of uncertainty descriptions that fit into the linear fractional format are frequency weighting functions and parameter variations. Frequency domain uncertainty is used to describe frequency dependent variation, via weighting functions, between the experimental data and the model. They are also used in the control problem formulation to shape the response of signals associated with performance requirements. These uncertainty descriptions are transfer functions between select inputs and outputs in the design model. This type description is *unstructured* uncertainty because it assumes there is no structure associated with the model errors except for known magnitude bounds. Alternatively, *parameter* variations can be used to introduce perturbations into the system model. These introduce uncertainty into the control design model coefficients to account for variations in natural frequency, damping levels, and mode shapes. Together, parameter variations and frequency domain uncertainty descriptions are used to define sets of flexible structure models.

6.1 Frequency Domain Uncertainty Descriptions

Frequency domain descriptions of uncertainty lead to the flexible structure being described by a nominal LTI system and frequency varying uncertainty models in the control problem formulation. These models allow us to account for the variation in experimental data at specific frequency points. For example, a frequency response experiment is performed to establish upper and lower bounds on both the magnitude and phase of the real system as a function of frequency. Variations in the data are then approximated by disk shaped regions in the complex plane, which lead to either a multiplicative or additive uncertainty description of the bounds [DoyWSt]. The nominal plant model together with the uncertainty models are used to define a set of plants within which the "real" physical system is assumed to lie. μ-analysis techniques measure the stability and performance of control laws for these prescribed models while the μ-synthesis methodology is employed to optimize control designs for these models to achieve the stability and performance requirements.

The plant transfer function can be described by $P(s) + \Delta P(s)$, where $P(s)$ is the nominal plant model and $\Delta P(s)$ is an unknown perturbation [MorZaf]. Every transfer function is taken to be a function of s, therefore the (s) notation will be dropped henceforth. Consider a SISO system with ΔP bounded across frequency by a weighting function, W_a, which is a real-rational, stable minimum phase transfer function and δ, a norm bounded complex number, $|\delta| \leq 1$, such that

$$|\Delta P(j\omega)| \quad < \quad |W_a(j\omega)\delta| \quad \textit{for all} \quad 0 \leq \omega \leq \infty, \quad |\delta| \leq 1, \quad s = j\omega \tag{6.1}$$

ω represents individual frequency points. The set of plants described by this uncertainty is given by

$$\hat{P}(j\omega) \quad = \quad P(j\omega) \; + \; W_a(j\omega)\delta \quad |\Delta| \leq 1 \tag{6.2}$$

Equation (6.2) is referred to as an additive uncertainty description and (6.1) defines the bound on the allowable additive uncertainty. δ is an unknown complex constant at each frequency. This assumption is implicit in the formulation of the robust control analysis and synthesis methods. For a multivariable system, the magnitude bounded scalar uncertainty δ can be replaced with Δ, a norm bounded complex matrix such that $\bar{\sigma}(\Delta) \leq 1$. The magnitude bounds in equation(6.1) would be replaced by norm bounds on the maximum singular value.

The additive uncertainty weighting is wrapped around the plant, shown in figure 6.1, and often is used to account for additive plant errors and uncertain right half plane zeros. Additive uncertainty weights can also describe performance requirements on the input responses to input commands. A variety of additive uncertainty weights can be developed for a MIMO system, each one adding states to the control problem. Low order weighting functions are usually employed to limit the number of states added to the problem formulation. Another reason for low order weights is that knowledge about the exact size of the uncertainty is often limited. Therefore describing the variation by a complex, high-order weight is unjustified.

Consider the following SISO system with additive plant uncertainty:

$$y = (P + W_a\Delta)u = (\frac{40}{s+20} + .2\Delta)u, \qquad \bar{\sigma}(\Delta) \leq 1 \tag{6.3}$$

This describes a set of plant models within which the "real" system lies. A Nyquist plot of this uncertain system is shown in figure 6.2. The plant is described at each frequency

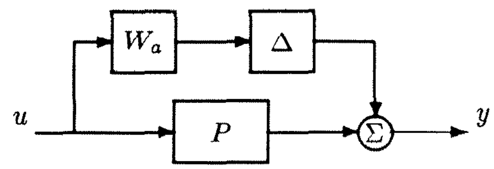

Figure 6.1: Block Diagram of Additive Uncertainty

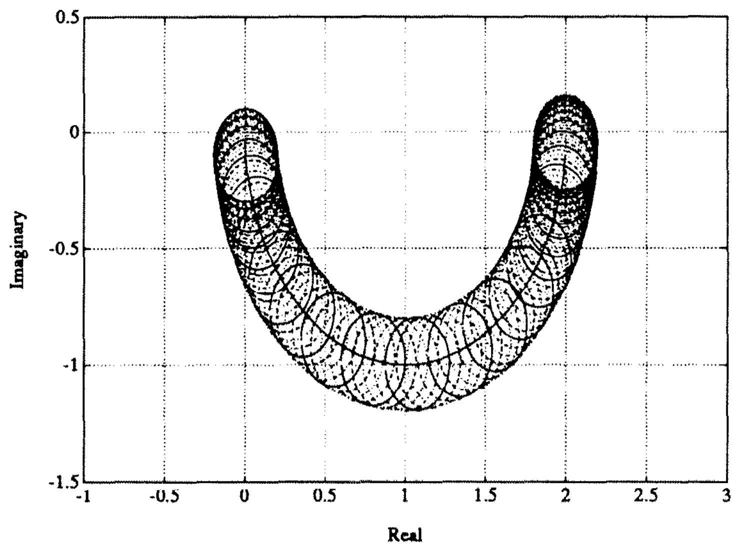

Figure 6.2: Nyquist plot of Additive Uncertainty

point ω, by a circle centered at $P(j\omega)$ of radius $|W_a(j\omega)|$. Plotting the magnitude Bode plot in figure 6.3, the magnitude of the model transfer function is defined to lie within the dotted lines. All transfer function models described by the model set $\tilde{P}$ lie within these bounds.

Additive uncertainty is used to account for unmodeled dynamics in flexible structures. These unmodeled dynamics are a result of low or high frequency modes, outside the desired control bandwidth. They cannot be modeled due to the representation of these modes being inaccurate, the frequencies and mode shapes associated with these modes varying, or low order design models are desired. Unmodeled modes need to be accounted for in the problem formulation, so as not to destabilize them with the control design. The size of the additive uncertainty weight is selected to encompass the transfer function response of these modes at each frequency.

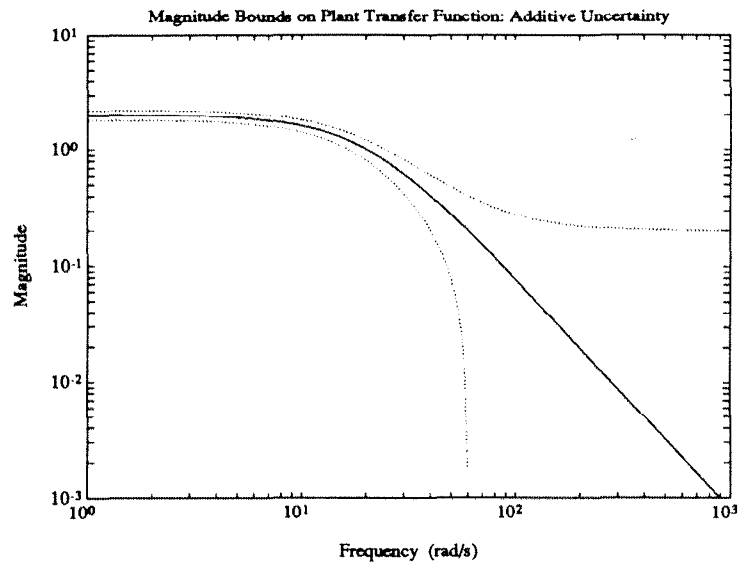

Figure 6.3: Bode plot of Additive Uncertainty

Selection of an additive uncertainty weight to account for unmodeled high frequency dynamics is shown in figure 6.4. The transfer function from A2S2 has modes between 30 and 80 Hz, which are not to be included in the control design model. A weighting function, W_a, given by $6.8\frac{(s+10)^2}{(s+100)^2}$, is selected to cover the higher frequency modes above 20 Hz. The control design accounts for the additive uncertainty weight by gain stabilizing the unmodeled modes.

It is easy to see in SISO systems how the additive uncertainty wraps around the nominal plant model. In MIMO systems, the additive uncertainty weights can be wrapped around the plant model from each input to each output with different additive weights used for each transfer function output. There are several ways of describing additive uncertainty in multivariable systems. One can allow cross-feed between channels or restrict the uncertainty to one input/output pair. The inclusion of information about how the variations affect the system leads to structure in the uncertainty descriptions. Full block unstructured uncertainty allows all the inputs to the uncertainty block to couple or cross-feed to the outputs. Restricting the uncertainty to each channel requires scalar block uncertainties, which add structure to the problem. Figure 6.5 is a diagram of the additive uncertainty, assuming that there is no coupling of the uncertainty in the plant model. This model restricts the effect of uncertainty in actuator i to sensor i,

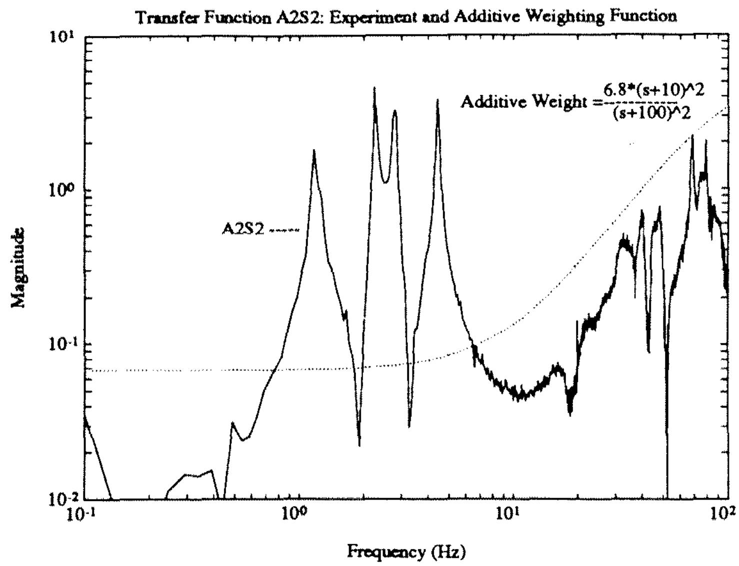

Figure 6.4: Transfer Function A2S2: Experiment and Additive Weighting Function

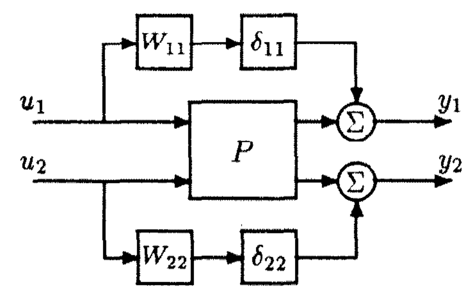

$$W_a = \begin{bmatrix} W_{11} & 0 \\ 0 & W_{22} \end{bmatrix},$$

$$\Delta = \begin{bmatrix} \delta_{11} & 0 \\ 0 & \delta_{22} \end{bmatrix}$$

Figure 6.5: Additive Scalar Block Uncertainty

($i \in 1, 2$). The matrix representation of the weighting W_a and the uncertainty block Δ are provided. Figure 6.6 allows paths for cross feeding between the inputs and outputs, implying that the uncertainty in the model inputs into either actuator affect both sensor outputs.

One can see how scalar or full blocks of unstructured uncertainty at the component level leads to structured uncertainty in the control problem formulation. Analyzing robustness and performance measures using singular values ignores the structure of the uncertainty descriptions. In most instances, this leads to a conservative measure of the affect of uncertainty on the control design. The μ-framework incorporates the uncertainty structure into the control analysis and synthesis problem.

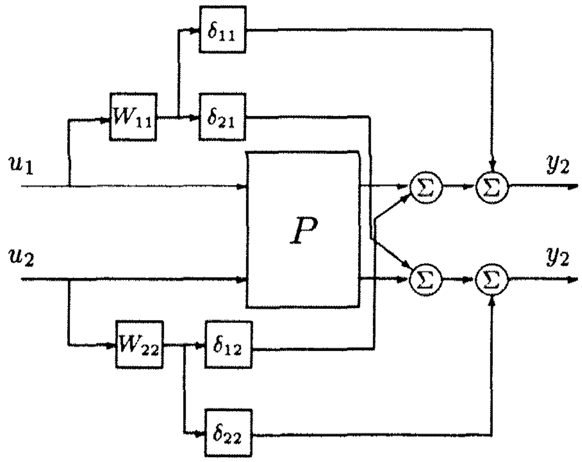

$$W_a = \begin{bmatrix} W_{11} & 0 \\ 0 & W_{22} \end{bmatrix},$$

$$\Delta = \begin{bmatrix} \delta_{11} & \delta_{12} \\ \delta_{21} & \delta_{22} \end{bmatrix}$$

Figure 6.6: Additive Full Block Uncertainty

An example of this in flexible structures is a high frequency mode, not to be controlled or modeled, which exhibits a large response due to one input channel. This may be attributed to an actuator exciting a set of local modes near the sensors. The designer would use this information to cover the high frequency mode with an additive uncertainty weight from the dominant actuator to all the sensors. Other actuator channels would require a weighting function smaller in magnitude because these actuators do not significantly excite the mode. To include the same level of additive uncertainty for each input/output pair would be overly conservative. The number of states associated with the additive uncertainty weights can be reduced by using the same weighting function from one input to all the sensor outputs, with each associated transfer function having the same level of uncertainty.

Another approach to modeling errors involves multiplicative uncertainty descriptions. Consider a SISO transfer function initially. Defining $W_m(\jmath\omega) = W_a(\jmath\omega)/P(\jmath\omega)$, we can describe a set of plants by

$$\hat{P}(\jmath\omega) \quad = \quad P(\jmath\omega)(1 \; + \; W_m(\jmath\omega)) \qquad and \qquad \frac{|W_a(\jmath\omega)|}{P(\jmath\omega)} \quad = \quad |W_m(\jmath\omega)| \tag{6.4}$$

Equation 6.4 is referred to as a multiplicative uncertainty description and states a bound on the allowed multiplicative uncertainty.

Multiplicative uncertainty descriptions are used to account for relative variations in input or output signals. Input multiplicative uncertainty is useful in describing actuator errors at high frequency and unmodeled actuator dynamics. For performance, weighting input signals corresponds to specifications on the input response to input commands. Output multiplicative uncertainty is used to model similar quantities on output signals and time delays. Sensor noise attenuation and output response to output commands are performance measures that can be specified with such weighting.

Component modeling often makes use of multiplicative uncertainty descriptions. Multiplicative uncertainty is used to model actuator and sensor components, independently or combined, to account for input/output variations in a multivariable transfer function. Typically, testing of actuators and sensors involves inputting signals into the components and measuring their response (i.e., force, displacement, torque). The output response is measured with a percentage error from a nominal plant model that may vary across frequency. A SISO design model $\hat{P} = P(1 + W_m\delta)$, $|\delta| \leq 1$, is described by a set of plants that lie inside a band around the nominal plant P. Nyquist and Bode plots of these model sets are similar to the additive uncertainty plots in figures 6.2 and 6.3. This is apparent from their relationship in equation 6.4.

Multiplicative uncertainty in multivariable systems can be included in the control problem formulation to account for directionality of signals. An example of this is a situation where a command to one actuator may affect the response of another actuator. Assuming there is no uncertainty associated with cross coupling terms between the inputs lead to the two scalar uncertainty blocks shown in figure 6.8. An alternative representation is to allow the uncertainty to affect both input channels due to a single input as shown in figure 6.9. Other representations of multiplicative uncertainty will lead to variations in the descriptions of W_m and Δ. As with the additive uncertainty, unstructured uncertainty at the component levels leads to structured uncertainty in the control problem.

The two examples of multiplicative and additive uncertainty presented have diagonal uncertainty weighting matrices. These were selected as a matter of convience. Alternatively, one can employ multivariable weighting matrices to better account for cross feed and coupling between channels. Additive and multiplicative uncertainty descriptions are only two ways of describing uncertainty. Figure 6.10 provides a list of alternative uncer-

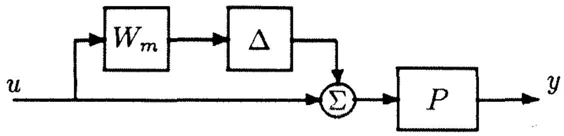

Figure 6.7: Input Multiplicative Uncertainty

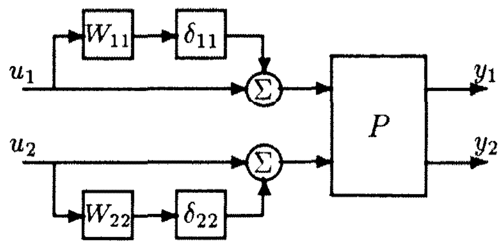

$$W_m = \begin{bmatrix} W_{11} & 0 \\ 0 & W_{22} \end{bmatrix},$$

$$\Delta = \begin{bmatrix} \delta_{11} & 0 \\ 0 & \delta_{22} \end{bmatrix}$$

Figure 6.8: Input Multiplicative-Scalar Block Uncertainty

tainty descriptions for multivariable systems for use in control design [DoyWSt]. These descriptions can account for variations in system dynamics, low frequency uncertainty, and changing rhp poles. Weights are also used to describe input and output sensitivity performance measures. The location of weighting functions in the problem formulation reflects performance or robustness requirements at those points. The designer's selection of uncertainty and performance weights provides specifications and limitations on the control designs. There are no guarantees of robustness or performance associated with transfer functions unaccounted and unweighted by uncertainty descriptions.

6.2 Selection of Uncertainty Weights

Uncertainty models are developed to account for the variation between phase I experimental data and the **MIMO** model. An additive uncertainty weight is used to describe the low frequency variation (below 0.5 Hz) and the high frequency modes (above 5.5 Hz) not included in the **MIMO** model. The additive uncertainty transfer function weight is given by

$$W_{additive} = 8.0\frac{(s+6)(s+12)(s+24)}{(s+.6)(s+400)(s+400)} \tag{6.5}$$

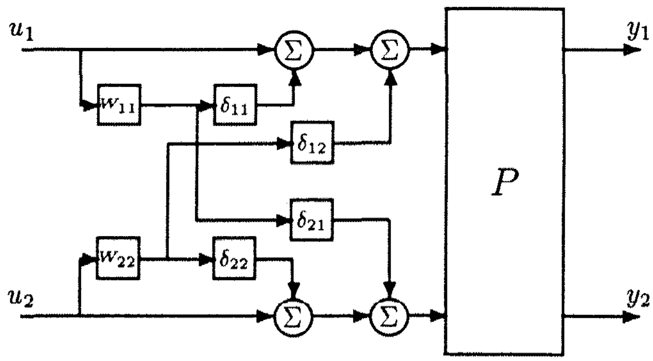

$$W_m = \begin{bmatrix} W_{11} & 0 \\ 0 & W_{22} \end{bmatrix},$$

$$\Delta = \begin{bmatrix} \delta_{11} & \delta_{12} \\ \delta_{21} & \delta_{22} \end{bmatrix}$$

Figure 6.9: Input Multiplicative-Full Block Uncertainty

This weight requires the μ-control design methodology to gain stabilize the high frequency modes and limits the controller gain below 0.5 Hz due to the variations at low frequency.

Multiplicative uncertainty models are used to account for input/output errors between the model and physical system. The additive uncertainty weight covers the model error outside the control bandwidth, hence the multiplicative uncertainty is relevant only within the control bandwidth. There is little variation of the uncertainty in this region, therefore a constant level of multiplicative uncertainty is used.

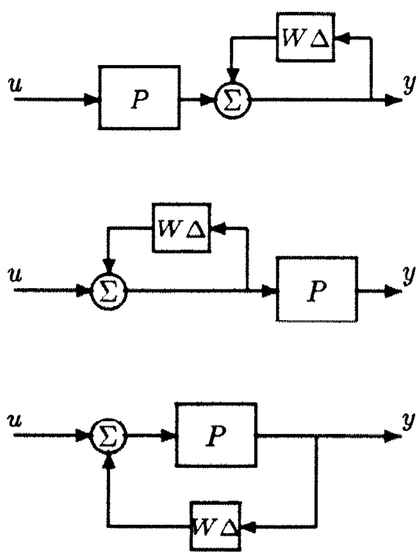

Uncertainty
Descriptions

$$y = (I + W\Delta)^{-1} P u$$

$$y = P(I + W\Delta)^{-1} u$$

$$y = (P^{-1} + W\Delta)^{-1} u$$

Figure 6.10: Alternative Uncertainty Descriptions

6.3 Parameter Variations

The control problem formulation often requires the transfer function from a number of inputs to outputs to be small over some frequency range. At the same time, the control law needs to be robust to changes or uncertainties in the system description. Another type of uncertainty, besides unmodeled dynamics, is due to parameter variation in the coefficients of a state-space model. These coefficients can be extracted from system description and rearranged so that the perturbations enter the system in a linear fractional form. This is defined as *parametric* uncertainty. One source of parametric uncertainty in flexible structures is in the mass, damping, and stiffness coefficients of the design model. Formulating these as a linear fractional transformation, they can be included in the μ-framework control design. A property of this is that perturbations of model coefficients are often real variations, with the parameters lying within a range of real numbers. Although real parameter variations can be analyzed, the current μ-synthesis framework can not handle real parameter variations directly, hence one needs to formulate these variations as complex uncertainties.

An approach to designing for real parameter variations is to bound these real variations by a complex variation. This approach introduces some conservatism into the controller design, which can be bounded and often made small. One can always design for real perturbations by replacing them with complex perturbations. Selection of the complex perturbations is important to reduce the conservatism of their approximation to the real variation.

The design model is a finite dimensional LTI system, described by

$$\begin{aligned} \dot{x} &= Ax + Bu \\ y &= Cx + Du \end{aligned} \tag{6.6}$$

where $A \in R^{n \times n}, B \in R^{n \times p}, C \in R^{m \times n}$

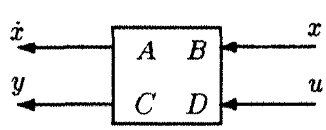

Consider a n-dimensional linear system P parameterized by k uncertain parameters, $\delta_1, .., \delta_k$, and described by the following uncertain equation

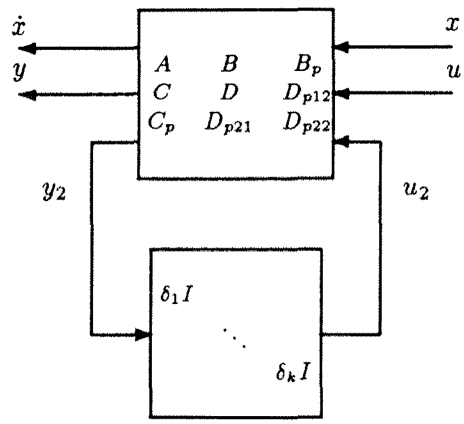

Figure 6.11: Block Diagram of State-Space Parametric Uncertainty

$$
\begin{aligned}
\dot{x} &= (A + \textstyle\sum_{i=1}^{k} \delta_i A_i)x \; + \; (B + \textstyle\sum_{i=1}^{k} \delta_i B_i)u \\
y &= (C + \textstyle\sum_{i=1}^{k} \delta_i C_i)x \; + \; (D + \textstyle\sum_{i=1}^{k} \delta_i D_i)u
\end{aligned}
\tag{6.7}
$$

The nominal system description is given by A, B, C, and D. The uncertainty enters the system via $\delta_1, \ldots, \delta_k$. These are assumed to be complex or real constant parameters, satisfying $\|\delta_i\| \leq 1$. The structure of the uncertainty is contained in A_i, B_i, C_i, D_i, reflecting how the i^{th} uncertainty, δ_i, effects the state-space model. The entries in these matrices correspond to the uncertainty levels on the coefficients. The designer selects the A_i, B_i, C_i andD_i matrices based on his knowledge of the problem.

The model description can be written as

$$
\begin{aligned}
\dot{x} &= Ax \; + \; Bu \; + \; B_p u_2 \\
y &= Cx \; + \; Du \; + \; D_{p12} u_2 \\
y_2 &= C_p x \; + \; D_{p21} u \; + \; D_{p22} u_2 \\
u_2 &= diag(\delta_1 I_1, \delta_2 I_2, \ldots, \delta_k I_k)
\end{aligned}
\tag{6.8}
$$

The additional input (u_2) and output (y_2) are defined so that all the parametric uncertainty is represented in the nominal system P, with unknown parameters, δ_i, entering as feedback gains around the additive input and output [MorMcA, Pack]. A diagram of this standard framework is shown in figure 6.11.

To address the problem of mass, damping, and stiffness variation in flexible structures, we will transform the problem into modal coordinates and include variations in the damping coefficient, ζ_i, and the natural frequency squared, ω_i^2. Considering the damping and natural frequency uncertainty individually would lead to repeated parametric uncertainties that are undesirable for the current discussion.

Consider a single mode transfer function, from input force to displacement output, with uncertainty in the damping and natural frequency squared terms.

$$\frac{1}{s^2 + 2\zeta\omega(1+\delta_1) + \omega^2(1+\delta_2)} \tag{6.9}$$

The transfer function can be represented using state space notation as follows:

$$\left[\begin{array}{c|c} \hat{A} & \hat{B} \\ \hline \hat{C} & \hat{D} \end{array}\right] = \left[\begin{array}{cc|c} 0 & 1 & 0 \\ -\omega^2(1+\delta_2) & -2\zeta\omega(1+\delta_1) & 1 \\ \hline 1 & 0 & 0 \end{array}\right] \tag{6.10}$$

and rewritten in the form of equation 6.7

$$\left[\begin{array}{c|c} \hat{A} & \hat{B} \\ \hline \hat{C} & \hat{D} \end{array}\right] = \left[\left[\begin{array}{c|c} A & B \\ \hline C & D \end{array}\right] + \sum_{i=1}^{n} \delta_i \left[\begin{array}{c|c} A_i & B_i \\ \hline C_i & D_i \end{array}\right]\right] \tag{6.11}$$

For a single real parameter, the perturbation matrix is rank one

$$\left[\begin{array}{c|c} A_i & B_i \\ \hline C_i & D_i \end{array}\right] = \begin{bmatrix} \alpha_{11} \\ \alpha_{12} \end{bmatrix} \begin{bmatrix} \beta_{11} & \beta_{12} \end{bmatrix} \tag{6.12}$$

which leads to a state space realization of P by

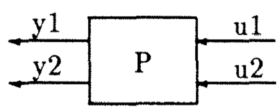

where P is

$$\left[\begin{array}{c|c} P_{11} & P_{12} \\ \hline P_{21} & P_{22} \end{array}\right] = \left[\begin{array}{c|cc} A & \alpha_{11} & B \\ \hline \beta_{11} & 0 & \beta_{12} \\ C & \alpha_{12} & D \end{array}\right] \qquad \Delta_1 = [\delta_1] \tag{6.13}$$

In the example stated, the $\hat{A}$ matrix is as follows

$$\hat{A} = \begin{bmatrix} 0 & 1 \\ -\omega^2(1+\delta_2) & -2\zeta\omega(1+\delta_1) \end{bmatrix} = \begin{bmatrix} 0 & 1 \\ -\omega^2 & -2\zeta\omega \end{bmatrix} + \delta_1 \begin{bmatrix} 0 & 0 \\ 0 & -2\zeta\omega \end{bmatrix} + \delta_2 \begin{bmatrix} 0 & 0 \\ -\omega^2 & 0 \end{bmatrix} \tag{6.14}$$

$$= \begin{bmatrix} 0 & 1 \\ -\omega^2 & -2\zeta\omega \end{bmatrix} + \delta_1 \begin{bmatrix} 0 \\ 1 \end{bmatrix} \begin{bmatrix} 0 & -2\zeta\omega \end{bmatrix} + \delta_2 \begin{bmatrix} 0 \\ 1 \end{bmatrix} \begin{bmatrix} -\omega^2 & 0 \end{bmatrix} \tag{6.15}$$

The interconnection matrix, P, and uncertainty description, Δ, for the system is given as

$$\Rightarrow \qquad \left[\begin{array}{c|c} \hat{A} & \hat{B} \\ \hline \hat{C} & \hat{D} \end{array}\right] = \left[\begin{array}{cc|ccc} 0 & 1 & 0 & 0 & 0 \\ -\omega^2 & -2\zeta\omega & 1 & 1 & 1 \\ \hline 0 & -2\zeta\omega & 0 & 0 & 0 \\ -\omega^2 & 0 & 0 & 0 & 0 \\ 1 & 0 & 0 & 0 & 0 \end{array}\right] \qquad \mathit{and} \qquad \Delta = \begin{bmatrix} \delta_1 & 0 \\ 0 & \delta_2 \end{bmatrix} \tag{6.16}$$

with the interconnection block diagram as

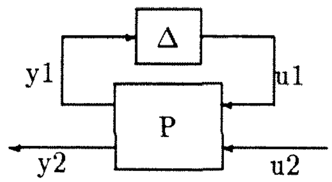

The same approach can be expanded upon for any number of δs. This provides a means to include parametric uncertainty associated with the state matrix A, into the interconnection description P.

6.3.1 Real and Complex Variations

Consider a one-mode system with real parameter variation associated with the natural frequency coefficient, ω^2. The transfer function equation is written as

$$\frac{1}{s^2 + 2\zeta\omega s + \omega^2(1+\delta)} \tag{6.17}$$

We want to find what real or complex value of δ will cause the system to go unstable. The roots of the denominator in equation 6.17 are given that the equation:

$$\begin{aligned} s_{1,2} &= -\zeta\omega \pm \sqrt{\zeta^2\omega^2 - (1+\delta)\omega^2} \\ &= -\zeta\omega \pm \omega\sqrt{\zeta^2 - 1 - \delta} \qquad\qquad \delta \in [-1, 1] \end{aligned} \tag{6.18}$$

given that the damping coefficient, ζ, is below critical damping ($\zeta < 1$), this implies

$$s_{1,2} = -\zeta\omega \pm j\omega\sqrt{(1-\zeta^2) + \delta} \tag{6.19}$$

for the real parameter case, and as long as $\delta > -1$, the system will be stable. This differs dramatically from the case where δ is a complex variation. For δ imaginary, $\delta = jx$, equation (6.18) can be rewritten as

$$s_{1,2} = -\zeta\omega \pm \jmath\omega\sqrt{(1-\zeta^2)+\jmath x} \tag{6.20}$$

The square root of a complex number is

$$\sqrt{\alpha + \jmath\beta} = \pm\left(\sqrt{\frac{\alpha+\sqrt{\alpha^2+\beta^2}}{2}} + \jmath\frac{\beta}{\mid\beta\mid}\sqrt{\frac{-\alpha+\sqrt{\alpha^2+\beta^2}}{2}}\right) \tag{6.21}$$

Unstable roots will occur if the imaginary part of the square root is greater than ζ. This restricts ζ for complex variations to

$$\sqrt{\frac{-(1-\zeta^2)+\sqrt{(1-\zeta^2)^2+x^2}}{2}} \quad < \quad \zeta \tag{6.22}$$

since both sides are positive, this leads to:

$$\begin{array}{rrcl} \Rightarrow & -(1-\zeta^2)+\sqrt{(1-\zeta^2)^2+x^2} & < & 2\zeta^2 \\ \Rightarrow & \sqrt{(1-\zeta^2)^2+x^2} & < & 1+\zeta^2 \\ \Rightarrow & (1-\zeta^2)^2+x^2 & < & 1+2\zeta^2+\zeta^4 \\ & x^2 & < & 4\zeta^2 \qquad \Rightarrow \quad |x| < 2\zeta \end{array} \tag{6.23}$$

The system will be stable for a complex variation of size $|\delta| < 2\zeta$. Whereas, with δ real, the requirement for stability is $\delta > -1$. As one can see for lightly damped structures, replacing a real parameter uncertainty directly with a complex one can lead to very conservative results.

6.3.2 Real versus Complex Perturbations

The above result is discouraging, due to its conservativeness, when one simply replaces real parameter variations with complex ones. The main reason for employing complex perturbations is that they can be included in a control problem formulation. The controller synthesis problem currently restricts the parameter variations to be scaled and norm bounded complex variations. One approach is to reformulate the complex uncertainty description describing the real parameter variation. Define a new nominal model in which a majority of the real variation is included via a complex uncertainty. A drawback of this approach is that a number of plants, not originally in the model set defined by the real parameter variation, are included in the new set of models. On the surface, this approach has as many shortcomings as the previous one. However, if the extra plant

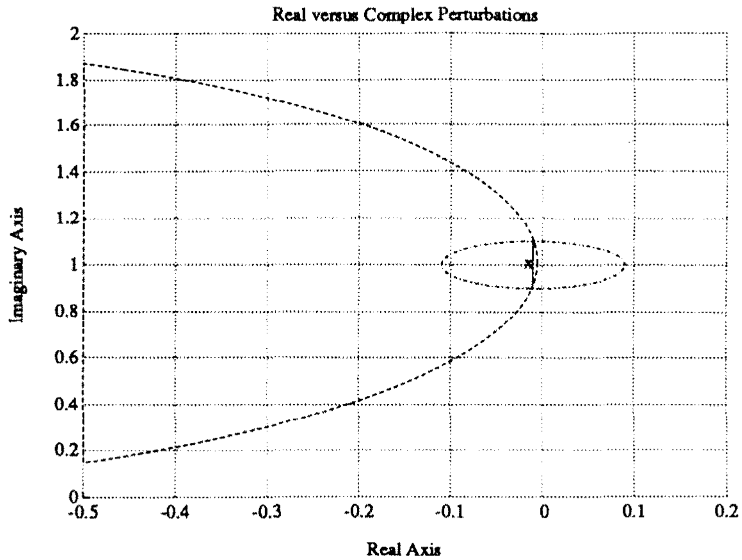

Figure 6.12: Real versus Complex Perturbations

models included in the set of allowable plants do not limit the stability of the control design, then no additional conservatism is introduced into the problem.

Graphically, as shown in figure 6.12, we can describe the idea in two dimensions. Suppose we represent the nominal plant by an $\times$ and the allowable real variation in the natural frequency coeffecient with a solid line in the complex plane. Using the nominal plant as the model, and replacing the real parameter variation by a complex variation (a disk in the complex plane represented by the dashed/dotted line), one can see how conservative that approach might be. By redefining the nominal plant and redefining the complex uncertainty by a dashed line, the entire real variation can be included in the set of plants described by the uncertainty.

As is expected, one does not get something for nothing. A number of extra plants are included in the set of allowable plants. This *does not* increase the conservatism of the design if the limiting points in the set are at the extremes of the real parameter variations. This approach is very useful in the modeling of real variations in the damping level and natural frequencies associated with flexible modes.

Control designs employing frequency domain uncertainty descriptions and parameter variations have been synthesized using the μ-framework. Frequency domain descriptions of uncertainty have been used more extensively due to the ability to translate system identification data into control design model with these descriptions. Parameter variations will play a role in future research into control design for large variations in damping levels and natural frequencies. Some initial work using parameter variations to formulate the addition of masses and dynamical systems to flexible structures has been investigated. This area of research shows great promise for the analysis and design of control laws with significant variations in plant dynamics.

Chapter 7

Tradeoffs Between Robustness and Performance Corresponding to Uncertainty Models

Selection of uncertainty descriptions plays a major role in the tradeoff between robustness and performance requirements in the control design process. A control law design based on an assumed "perfect" model leads to a high performance design on the model, but when implemented on the "real" system it may be destabilizing or exhibit poor performance. This is attributed to the control design methodology optimizing the control law based only on the information provided it, which it assumes is "perfect." Models, though, are only approximations to the "real" system. Uncertainty descriptions are introduced to account for variations between the models and the physical system. They provide a quantitative measure of these differences. Control design methodologies have been developed, (e.g., μ-synthesis), to include uncertainty descriptions into the optimization process.

The selection of uncertainty descriptions and levels are not arbitrary. These descriptions of model error need to be developed based on the actual system characteristics. For example, choosing a large uncertainty model, unmotivated by the physical data, can lead to overly conservative control designs, thereby limiting performance of the control design. A tradeoff exists between robustness of the control law and performance objectives in the design process. This chapter investigates this tradeoff in the selection of uncertainty descriptions and levels for the Phase I flexible structure experiment. Results indicate that an accurate plant (nominal) model and uncertainty descriptions lead to control laws which exhibit superior performance when implemented on the physical system. This compares with control laws formulated without or with too large an uncertainty description. The selection of input or output uncertainty models to account for model errors has a direct bearing on the performance of multivariable control designs. This is very different from single-input/single-output uncertainty models where their location in the problem formulation is not important.

A series of control laws are designed for the Phase I Caltech flexible structure with varying levels of uncertainty and sensor noise weights. One set of control laws are designed using only an additive sensor noise model to account for uncertainty. These control laws destabilize the physical system until the sensor noise level model is increased, in the problem formulation, to the magnitude of the flexible modes response. As the noise level is increased, the design methodology subsequently reduces the control gain, limiting the closed-loop performance. The only control design which is stable when implemented is synthesized with a high level of sensor noise and provides little performance improvement compared with the open-loop response. A set of control laws is formulated using frequency domain uncertainty descriptions of the variations between the model and the "real" system. These designs make use of an additive uncertainty description to account for high frequency unmodeled dynamics and multiplicative input/output uncertainty to account for actuator/sensor errors and mode shape mismatch. As one traverses from a control law designed with only an additive uncertainty model to one with a significant amount of input (output) uncertainty, the performance level is maximized between these two extremes. This clearly indicates the tradeoffs between robustness and performance in control design and the importance of uncertainty descriptions in the control design process.

7.1 Control Objectives

The control objective is to attenuate vibration of the first six natural frequencies in the Phase I Caltech flexible structure at the three accelerometer locations. These modes are between 1.2 and 4.5 Hz and consist of two first bending, two torsional and two second bending modes. The disturbance enters the structure via air actuator 1, and blows directly on the sensor 1. A sine sweep disturbance, between 1 and 6 Hz, drives the air solenoid. The performance measure is to minimize the maximum frequency response of the first six modes at the sensor locations, as compared with their open-loop response, for a worst case input signal. This specification is formulated as minimizing the $\|\cdot\|_\infty$ norm between the input disturbances and sensor outputs. The robustness measures and other performance specifications are formulated using the $\|\cdot\|_\infty$ norm, allowing μ-synthesis techniques to be used for control design.

7.2 Uncertainty Descriptions

Frequency domain uncertainty descriptions are employed to account for the variation between the model and the "real" system. An additive uncertainty weight is used to account for the low frequency inaccuracies (below 0.5 Hz) and the unmodeled high frequency dynamics (above 10 Hz). The magnitude of the additive uncertainty weight at high frequency is selected to envelope the unmodeled modes of the system. The additive uncertainty weight assures that the high frequency modes are gain stabilized by requiring the control design to satisfy $\| W_{add}^{-1} K S \|_\infty < 1$, where K is the controller and S is the sensitivity transfer function $(I - P_{nom} K)^{-1}$. A plot of the frequency response of transfer functions between voice coil (VC) actuator 2 and the three sensors along with the additive uncertainty weight is shown in figure 7.1. The additive uncertainty weight is given by

$$W_{add} = 8\frac{(s+6)(s+12)(s+24)}{(s+.6)(s+400)^2}$$

Within the controller bandwidth, 1 to 5 Hz, the additive uncertainty takes on a minimal value. This weight is purposely reduced within the frequency range performance is desired to demonstrate how additional uncertainty descriptions, (i.e., multiplicative

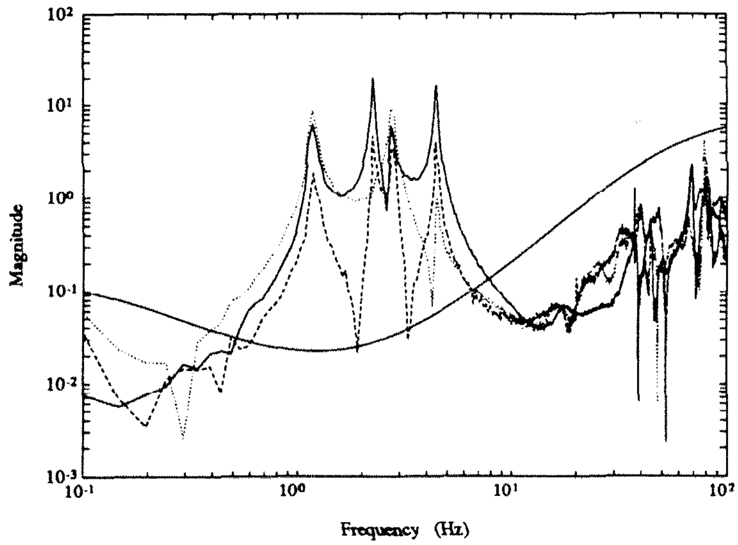

Figure 7.1: Frequency Response of Actuator 2 to Sensors and the Additive Uncertainty Weight

input and output uncertainty weights), affect the performance of the control laws. The magnitude of the additive uncertainty weight is selected to insure that all control laws synthesized with this weight would stabilize the structure. Control laws based on additive sensor noise models only, do not include this weight, leading to destabilizing control laws. The multiplicative uncertainty on the inputs and outputs is varied independently between 0 and 25% in a series of control designs to gauge their effect on the robustness and performance properties of the control designs. The multiplicative uncertainties are selected to be constant across frequency. It is assumed that between 1 and 5 Hz there is negligible frequency variation in the errors. The additive uncertainty weight dominates the uncertainty models outside this range. In the control problem formulation, the multiplicative weights are distributed between the inputs and outputs, to and from the uncertainty blocks, to provide better initial scaling for the H_∞ control design algorithms.

7.3 Control Problem Formulation

Control designs are formulated to examine the tradeoff between robustness levels and performance objectives using the μ-synthesis control design methodology. The Phase I experimental structure provides the test bed for the experimental investigation. A

3-input/3-output nominal model, P_{nom}, of the flexible structure, is developed using the identification techniques described in the system identification section. It serves as a baseline to which uncertainty models are appended. A state-space model description of the experimental flexible structure is provided in Appendix A.

A block diagram of the problem formulation is shown in figure 7.2. As stated, the control design must be robust to unmodeled high frequency dynamics and model errors while attenuating the vibrational responses of the first six flexible modes. The additive uncertainty weight accounts for the neglected high frequency modes and some low frequency errors. It is modeled as an unstructured full block uncertainty, Δ_1, around the flexible structure model as seen in the block diagram. The additive uncertainty weight remains unchanged throughout the set of control designs.

Multiplicative input and output weights, *actu* and *sensu*, are the parameters varied to examine tradeoffs between the robustness and performance of the control designs. A constant input uncertainty, *actu*, is selected to account for actuator errors and mismatch between the input mode shapes and the experimental data. *actu* is varied from 0 to 0.5, which represents a 0 to 25% variation in the uncertainty level associated with the input signals to the flexible structure model. *sensu* represents a constant multiplicative output uncertainty, which is varied. Sensor errors and output mode shape discrepancies are accounted for by this uncertainty description. One set of control laws is formulated with no output multiplicative uncertainty, *sensu*, and the input uncertainty, *actu*, varied. These control laws investigate the effect of input uncertainty descriptions on the performance characteristics of the control designs when implemented on the physical system. Similarly, a set of control laws are synthesized with no input uncertainty, *actu*, and the output multiplicative uncertainty, *sensu*, varied between 0 and 0.5 (0-25% uncertainty). The effect of output uncertainty on control designs is examined in this set of experiments.

The input and output multiplicative uncertainty models are described by full block unstructured uncertainty. Full block uncertainty descriptions indicates that cross coupling between the input (output) channels is allowed. For the Phase I structure, cross feed in the input channels can be caused by: movement of one of the actuators affecting the position of the other actuators; crosstalk between the actuator wires carrying the force commands, or directionality mismatch between the mode shapes in the model and

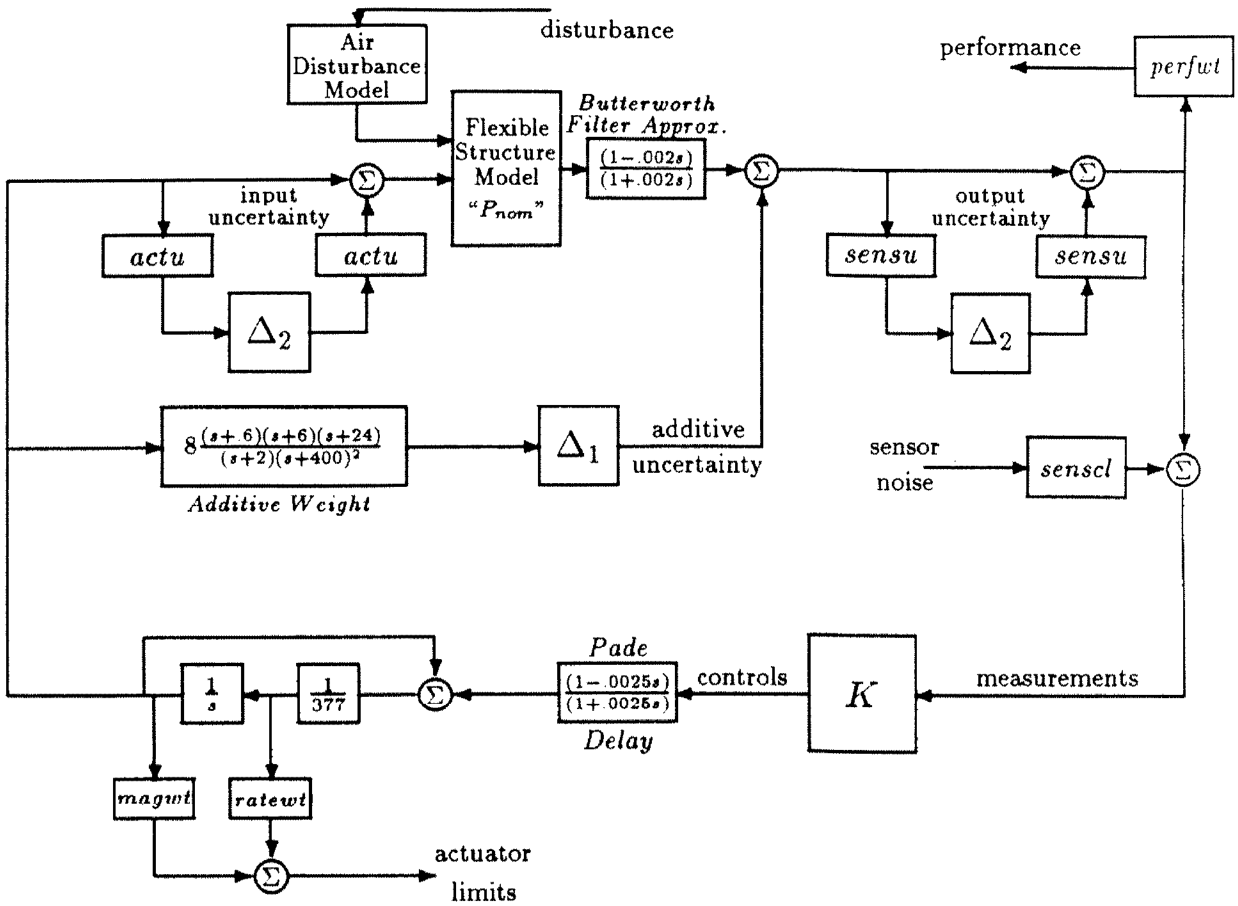

Figure 7.2: Block Diagram of Tradeoff Control Problem Formulation

the physical system. Position variation should have little effect on the actuator response in this system, because the actuators are driven by current amplifiers. This eliminates back electro-magnetic flux (EMF), which may affect output force levels of the actuators. The actuator wires on the structure are twisted, shielded pairs to reduce the potential for crosstalk between them. The full block uncertainty description primarily accounts for mode shape errors that are present in the model. During the analysis stage of the control designs, comparisons are made between assuming the multiplicative uncertainty to be a full block or three independent scalar uncertainty blocks, which restricts the uncertainty to the individual channels (i.e., no cross coupling of uncertainty). The three scalar, structured, uncertainty blocks had values of μ that were 1-3% less than the full block uncertainties. This implies that if the structured uncertainty is a more accurate description of the physical system, it would have 1-3% better robustness margins and exhibit 1-3% better performance than the unstructured uncertainties when implemented. This is a modest difference, hence the unstructured uncertainties are used. The advantage of describing the input uncertainty by a full block is two fold: it reduces the number of uncertainty block in the μ-analysis problem and the full block uncertainty accounts for cross feed between channels leading to a more robust control design. Output multiplicative uncertainty is also treated as a full block uncertainty. This uncertainty description accounts for output mode shape mismatch and crosstalk between the accelerometer signals. There is little difference, on the order of 1-3%, whether a full block uncertainty or three scalar uncertainties are used in the analysis of the control laws with output multiplicative uncertainty.

There are a number of performance specifications associated with the experimental flexible structure. The performance objective is to minimize the maximum transfer function frequency response between the input disturbance and the three accelerometer outputs. The frequency range of interest is between 1 and 5 Hz and contains the six flexible modes. To achieve this objective, the performance weight for vibration attenuation is selected as a constant scaling, *perfwt*, on the sensor outputs. The disturbance to acceleration output transfer functions are first scaled to one, then the performance weight, *perfwt*, is used to determine the amount of attenuation of the frequency domain peaks. A constant weighting is sufficient only if one desires the closed-loop performance transfer functions to be flat across frequency with no additional frequency shaping. The magnitude of the six flexible modes between 1 and 5 Hz are all on the same order, therefore a constant scaling provides a good performance objective and does not add additional states to the control problem.

The input disturbance enters via air actuator 1 and blows directly on sensor 1. A simple model of the excitation and the air actuators is included in the control design, $(\frac{10}{s+10})$. There are several performance restrictions associated with the VC actuators. These actuators are limited to ± 3 lbs of force at ± 5 V with a 60 Hz rate limit. The actuator force limit is included in the control design by scaling, *magwt*, its output to 1 when the force is at ± 3 lbs. This scaling needs to be consistent with a unit input level of disturbance. Similarly, the 60 Hz rate limit is scaled with *ratewt*. The sensor noise level for the accelerometers is included as a performance limitation in the problem formulation. The weighting, *senscl*, is selected to be 2×10^{-3} and represents an accelerometer signal to noise ratio of 250. These performance specifications and limitations are accounted for in the μ-framework by a full block unstructured uncertainty, resulting in a $\|\cdot\|_\infty$ norm measure. All performance requirements are satisfied when the $\|\cdot\|_\infty$ of the performance block is less than 1.

The accelerometers are filtered by 100 Hz, 4^{th} order Butterworth filters before being input into the Masscomp A/D channels. One can account for these filters with accurate fourth order models in each channel, but it would entail an additional 12 states. A first order approximation of the filters, $(\frac{1-.002s}{1+.002s})$ is used instead, reducing the additional states to 3. This approximation is accurate up to 40 Hz and accounts for the phase lag due to the filters. The first order model is accurate far above the controller bandwidth, 5 Hz, and any error induced by this approximation is accounted for by the additive uncertainty weights. A first order Pade approximation, $(\frac{1-.0025s}{1+.0025s})$, is included to model the $5ms$ sample time delay associated with the Masscomp D/A channels. The complete block diagram is shown in figure 7.2.

The block diagram is reformulated into the LFT general framework to design control laws using the μ-synthesis methodology. A diagram of the LFT is shown in figure 7.3. The dimensions of the Δ blocks are: 3×3 for Δ_1, 3×3 for Δ_2, and 6×4 for Δ_3. Δ_1 is associated with the additive uncertainty, Δ_2 with the multiplicative input (output) uncertainty, and Δ_3 is the performance block. All the Δ_i blocks are full blocks. Either input or output multiplicative uncertainty is included in the control problem formulation. In this set of designs, both are not included simultaneously. The Δ block associated with the control design problem has structure due to the two uncertainty blocks and one performance block. A pure H_∞ control design would synthesize a control law for one full block of size 12×10, neglecting the inherent structure associated with the three blocks. Ignoring the structure of the uncertainty block leads to overly conservative control laws. The μ-synthesis methodology incorporates knowledge of this structure in the control design process.

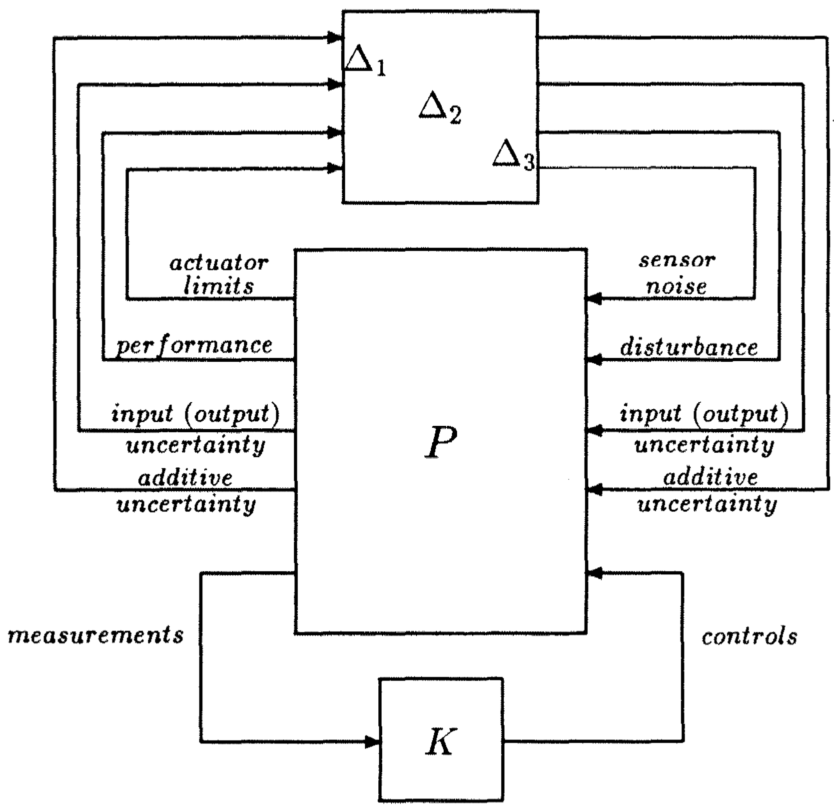

Figure 7.3: LFT of Tradeoff Control Problem Formulation

7.4 Control Designs

7.4.1 Sensor Noise Only

Six control laws are synthesized based on the block diagram in figure 7.2 with no additive or multiplicative input/output uncertainty, (i.e., *actu* and *sensu* are set to zero). The sensor noise weight, *senscl*, is varied between 4×10^{-3} and 2.3 to account for uncertainty and provide robustness in the control designs. Table 7.4.1 contains a list of the control law parameters used in the design and the results of implementation on the flexible structure experiment. The list includes: the level of sensor noise, *senscl*, the performance scaling, *perfwt*, the value of μ achieved in the design and their performance on the structure. Each control design is synthesized to achieve a μ value of 1. That is, the performance and robustness specifications are scaled to be 1 when they are satisfied.

Controller	*senscl*	*perfwt*	μ	Predicted Performance	Experimental Performance
$K1sn$	4×10^{-3}	15.00	0.99	.067	Unstable
$K2sn$	4×10^{-2}	14.00	0.98	.071	Unstable
$K3sn$	4×10^{-1}	8.00	1.00	.125	Unstable
$K4sn$	9×10^{-1}	4.75	1.00	.211	Unstable
$K5sn$	1.15	4.75	1.00	.253	Unstable
$K6sn$	2.30	2.12	0.99	.472	0.87

Table 7.4.1: Parameters for Control Design with Sensor Noise

Figures 7.1 and 7.2 contain singular value plots of the loop gain, $P_{nom}K$, the plant model multiplied by the controller, for control laws $K1sn$ and $K6sn$. Controllers $K1sn$ through $K5sn$ are destabilizing when implemented on the experimental structure. This is due to the excessive gain of the control laws at high frequency, which destabilizes the unmodeled high frequency dynamics. One can see the large loop gain at high frequency associated with $K1sn$ in figure 7.1. Raising the level of the sensor noise to the magnitude of the flexible mode peaks, $K6sn$, leads to a reduction in the controller gain at low and high frequency. This stabilizes the system, and, in turn reduces the performance of the control laws. Controller $K6sn$, has little improvement in performance as compared to the open-loop response seen in the time response data in figures 7.3 and 7.4. Control laws

$K1sn$ through $K6sn$ were stable and achieved their predicted performance in simulations using the nominal model.

This is an extreme example of the shortcomings associated with designing control laws based solely on additive noise models to account for model errors. It illustrates, though, the need to provide information in the model formulation as to the fidelity of the model across a range of frequencies. The structural model is sufficiently accurate between 1 and 5 Hz that by accounting for the unmodeled dynamics with an additive uncertainty model a control law can be synthesized stabilizes the system and performs well when implemented. The development of better uncertainty models to describe the model errors can further increase the performance of control laws on the experimental flexible structure.

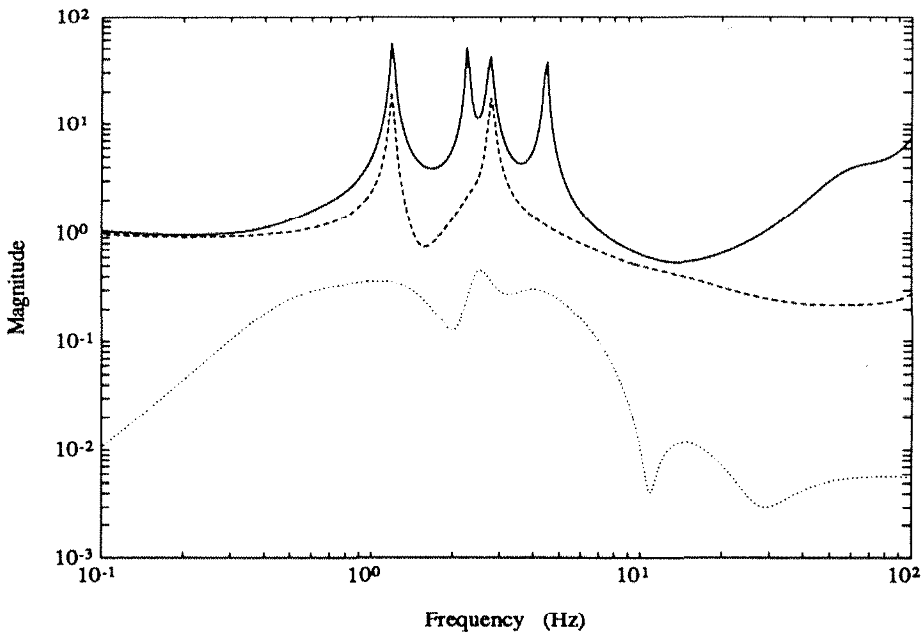

Figure 7.1: Singular Value Plot of the Loop Gain for Controller $K1sn$

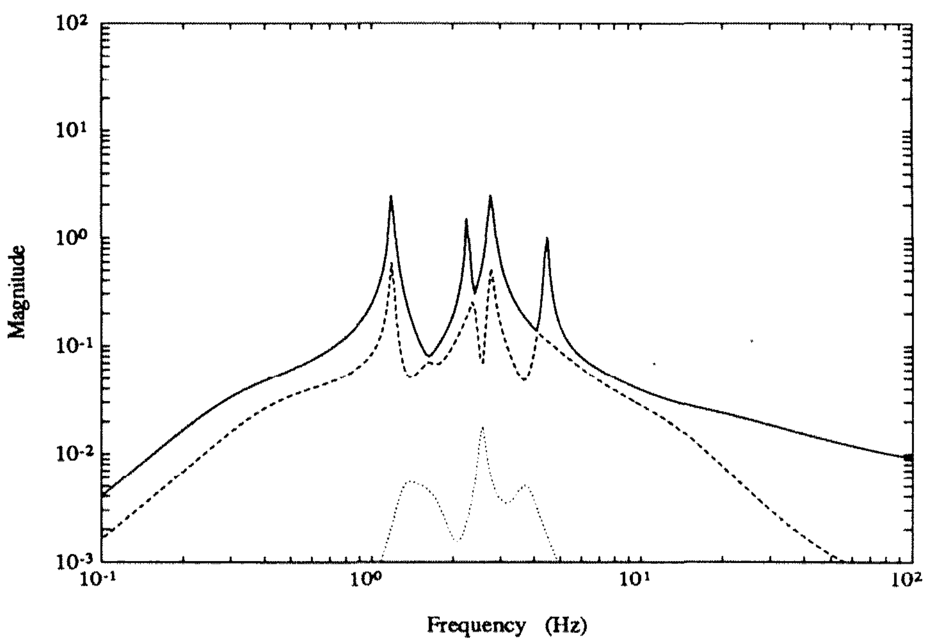

Figure 7.2: Singular Value Plot of the Loop Gain for Controller $K6sn$

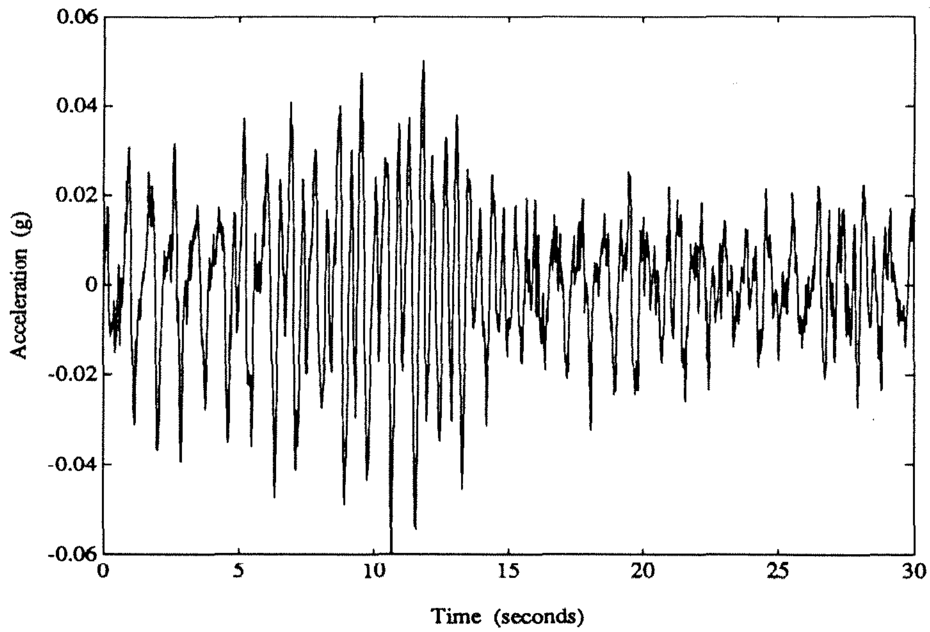

Figure 7.3: Open-loop Sensor 1 Response to 1-6 Hz Sine Sweep into Air Actuator 1

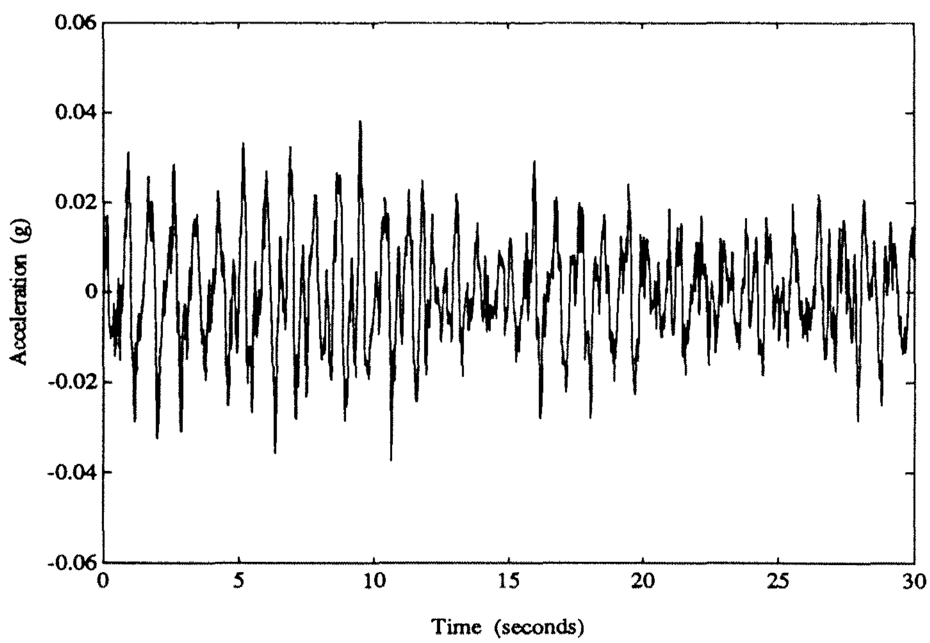

Figure 7.4: Closed-loop, $K6sn$, Sensor 1 Response to 1-6 Hz Sine Sweep into Air Actuator 1

7.4.2 Input Multiplicative Uncertainty

A series of control laws is synthesized using additive uncertainty and input multiplicative uncertainty descriptions to account for variations in the model. The block diagram in figure 7.2 describes the problem formulation. The output uncertainty, *sensu*, is set to zero in this series of designs. Ten control laws are formulated for *actu* varying between 0 and .5. This results in the input multiplicative uncertainty level varying between 0 and 25%. Robustness and performance of the control designs are traded off in the design process, as one is increased the other is decreased. Each design is iterated on until it achieves a μ value of approximately 1. This is done by selecting a desired level of input uncertainty and scaling the performance requirement, *perfwt*, until the the control design achieves a μ value of 1. A control law with a μ value of 2.0 indicates that for the uncertainty and performance criteria prescribed, the control laws achieve $\frac{1}{2}$ or 50% of the performance for $\frac{1}{2}$ or 50% of the uncertainty level.

Each control law is designed for a specific level of uncertainty, α. For the purpose of this discussion, we will refer only to the input multiplicative weight, *actu*, as the uncertainty. The additive uncertainty is lumped into the design model because it doesn't vary with each control design. For a prescribed level of uncertainty, α, using the μ-synthesis methodology, we are able to achieve a performance level of β, corresponding to $\frac{1}{perfwt}$ for a control design $\bar{K}$. This provides the point "$\times$" on the curve in figure 7.5. For $\beta = 1$, the closed-loop performance is equal to the open-loop performance, for $\beta < 1$, the closed-loop performance is better than the open-loop, and for $\beta > 1$ it is worse than open-loop. Assuming the system to be controlled is described exactly by the design model defined by the nominal model and uncertainty descriptions, the level of performance achieved for the worst case input signal affecting the worst case plant model can be formulated as an H_∞ control problem.

Suppose that initial model set, described by the nominal structural model and uncertainty descriptions, is a conservative description of the "real" structure. The control law $\bar{K}$ designed for this model set will most likely achieve better performance when implemented than is anticipated. This is due to the predicted performance level, β, is related to the worst plant model in the initial model set. If the nominal plant model is not the worst case plane model in the set, the performance level of the closed-loop system will be higher than the design value. This is attributed to the $|| \cdot ||_\infty$ measure is related to the worst case performance. Similarly, if the uncertainty description does not encompass the "real" system, the control law may destabilize the system or performance may degrade severely. As the amount of error between the design model and the physical system, α, increases, the performance of the control law, $\bar{K}$, will decrease. A graphical representation of this is presented in figure 7.5. The dotted line indicates how the performance, β, of the control law $\bar{K}$ might vary as a function of the uncertainty level α. As an example, the control law $\bar{K}$ is designed for an uncertainty level of 40%, and achieves a performance of 0.58. If there is less uncertainty between the "real" system and the model, the control law will exhibit improved performance when implemented. Conversely, if there is more error the control law performance will degrade.

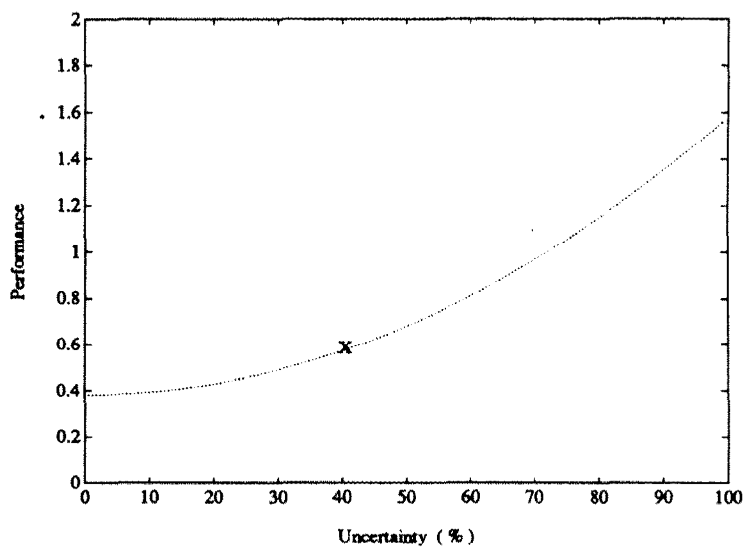

Figure 7.5: Control Design, $\bar{K}$, for an Uncertainty Level of 40%

A number of control laws, K_1 to K_6, are designed for 3, 10, 20, 40, 60, and 80 percent uncertainty, each generating a curve similar to the one in figure 7.5. A graph of these curves is shown in figure 7.6. Each "x" in the figure corresponds to a control law synthesized for the specified level of uncertainty and corresponding level of performance. Each control law would have a μ value of 1. The solid curve represents the achievable performance of the control designs based on the nominal model and the uncertainty

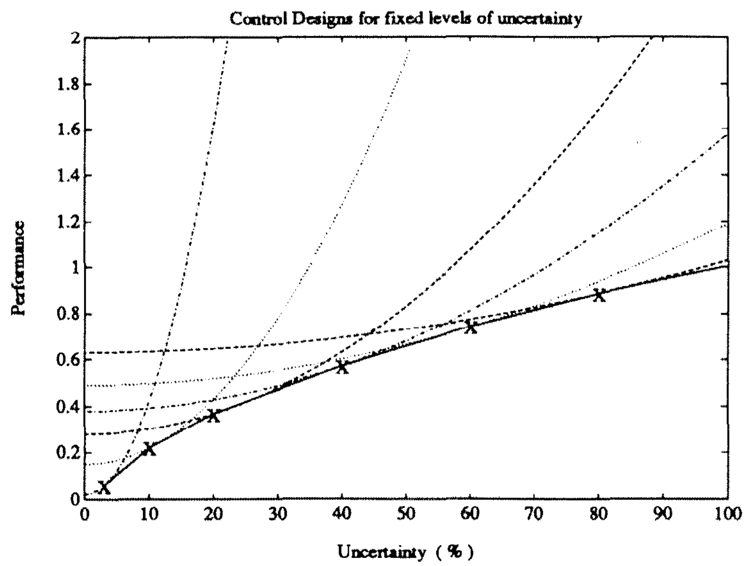

Figure 7.6: Six Control Designs for Uncertainty Levels of 3%, 10%, 20%, 40%, 60%, 80%

description. As one would expect, the highest performance is achieved when the nominal model is a perfect representation of the "real" system. From these graphs, one can see that accurately describing the physical system with non-conservative sets of plants results in the superior performing control laws on the system for a given nominal model and uncertainty description. One can use this approach to verify the consistency of the model and uncertainty descriptions.

Ten control laws are synthesized with input multiplicative uncertainty. The percent input uncertainty is selected and then the performance objective, *perfwt*, is scaled to achieve a μ value of 1.

A plot of the value of μ across frequency for $K1am$, $K3am$, and $K10am$ is shown in figure 7.7. One notices that their μ values very significantly across frequency. An optimal H_∞ control law usually has a maximum singular value of the closed-loop frequency response which is flat across frequency. The μ control laws do not have this property since a sub-optimal H_∞ control law is synthesized using μ-synthesis techniques and the $\|\cdot\|_\infty$ is just an upper bound for μ. A sub-optimal control law usually has a slightly larger $\|\cdot\|_\infty$ than the optimal but will roll off significantly at the high and low frequencies. This is due to the control design methodology not pushing the constraints of the system to squeeze out the last bit of performance. Often the robustness characteristics of the sub-optimal H_∞ control laws are significantly better than the optimal designs with little degradation in performance.

The level of sensor noise, *senswt*, is fixed at 2×10^{-3}. This represents the relative noise level measured experimentally. The actuator weights, *magwt* and *ratewt*, are selected to correspond to the magnitude and rate limits of the actuators. For these control designs, *magwt* is set to 80 and the *ratewt* is set to 3770. Table 7.4.2 contains the parameters varied in the control designs.

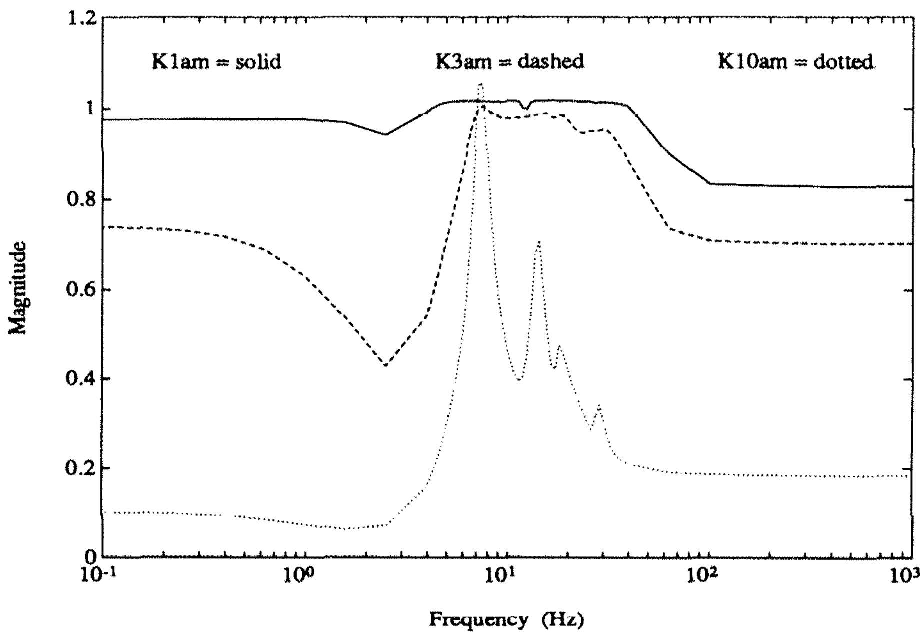

Figure 7.7: A Plot of μ for Control Designs $K1am$, $K3am$ and $K10am$

An experimentally derived set of transfer function data is generated between the input disturbances and sensor outputs, using the open-loop response and the ten closed-loop responses. The open-loop frequency response is shown in figure 7.11. Singular value plots of the loop gain for $K1am$, $K3am$, and $K10am$ are provided in figures 7.8, 7.9, and 7.10 and their corresponding experimental closed-loop frequency responses of $K1am$, $K3am$ and $K10am$ are shown in figures 7.12, 7.13 and 7.14. The frequency range of the plots is between 0 and 10 Hz because the input disturbance signals a sine sweep between 1 and 6 Hz. Table 7.4.2 contains the raw experimental data of the closed-loop experiments for each control design. The performance objective is to attenuate the

Control Law	Actuator Uncertainty (%)	$perfwt$	Predicted Performance	μ
$K1am$	0.00	13.0	.077	1.02
$K2am$	1.00	12.4	.081	1.02
$K3am$	2.25	11.0	.091	1.01
$K4am$	4.00	10.0	.100	1.02
$K5am$	7.29	8.4	.119	1.03
$K6am$	10.00	7.1	.141	1.00
$K7am$	14.44	5.8	.172	1.08
$K8am$	17.00	4.2	.238	1.07
$K9am$	20.25	3.9	.256	1.02
$K10am$	25.00	2.9	.345	1.02

Table 7.4.2: Parameters for Control Design with Input Multiplicative Uncertainty

maximum frequency peak value of the three sensor transfer functions due to the input disturbance. The experimental performance is measured as the maximum closed-loop peak response to the maximum open-loop response. The maximum frequency response magnitude peaks associated with accelerometers 1, 2 and 3 are given in table 7.4.2. The ratio of the maximum peak of the closed-loop control law to the open-loop response corresponds to the experimental performance.

The highest performance, 0.073, representing a reduction of the maximum frequency domain peak by 13.7, is achieved for the control law designed with 2.25% input uncertainty. Control laws designed for higher and lower uncertainty levels than this exhibited less performance. $K1am$ and $K2am$ achieved performance levels less than predicted by the design model, and all other control designs surpassing their predicted performance. Figure 7.15 is a plot of the designed level of performance given a value of uncertainty as a function of input uncertainty weight. These are compared with the experimentally derived performance levels. Circles, 'o', represent the experimental values and 'x' represent the model. One can interpret this graph as one interprets figure 7.6. The set of models described by the problem formulation for $K1am$ and $K2am$ does not contain the "real" system, because for the worst case plant description the performance levels are higher than achieved when implemented on the experimental structure. The set of models defined in the control design problems for $K3am$ through $K10am$ provide a good representation of the "real" system due to the robustness and performance levels following

Control Law	Maximum Magnitude in Frequency Range 0-10 Hz Raw Data Sensor 1	Sensor 2	Sensor 3	Experimental Performance	Predicted Performance
Open-loop	2.1511	1.2450	0.5232	1.0000	1.000
$K1am$	0.187	0.139	0.176	0.087	0.077
$K2am$	0.187	0.082	0.028	0.087	0.081
$K3am$	0.157	0.074	0.024	0.073	0.091
$K4am$	0.176	0.087	0.026	0.082	0.100
$K5am$	0.200	0.088	0.025	0.093	0.119
$K6am$	0.261	0.131	0.029	0.121	0.141
$K7am$	0.306	0.124	0.026	0.142	0.172
$K8am$	0.265	0.181	0.025	0.123	0.238
$K9am$	0.223	0.160	0.020	0.104	0.256
$K10am$	0.346	0.247	0.030	0.161	0.345

Table 7.4.3: Experimental Results of Control Designs with Input Multiplicative Uncertainty

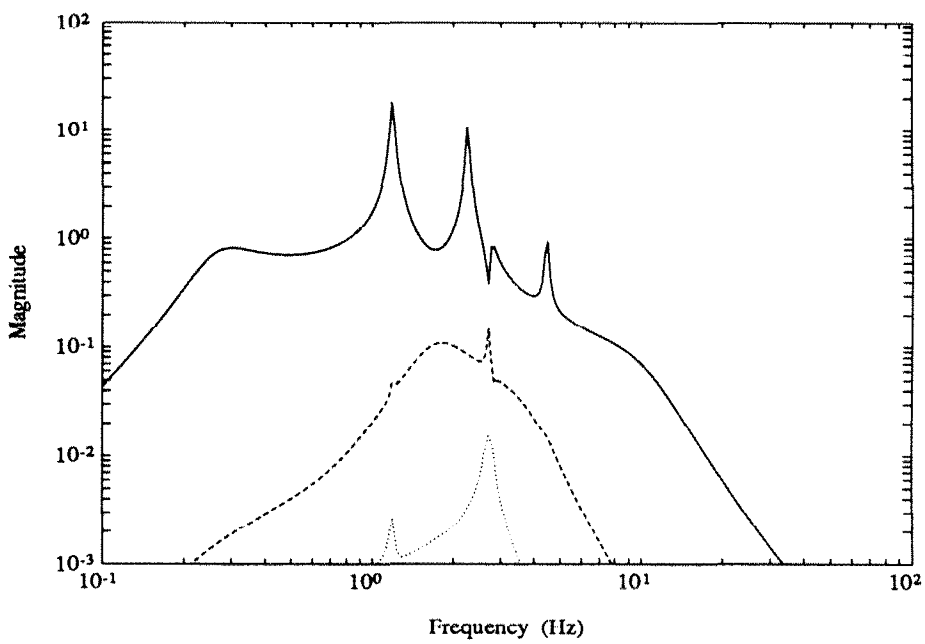

Figure 7.8: Singular Value Plot of the Loop Gain for Controller $K1am$

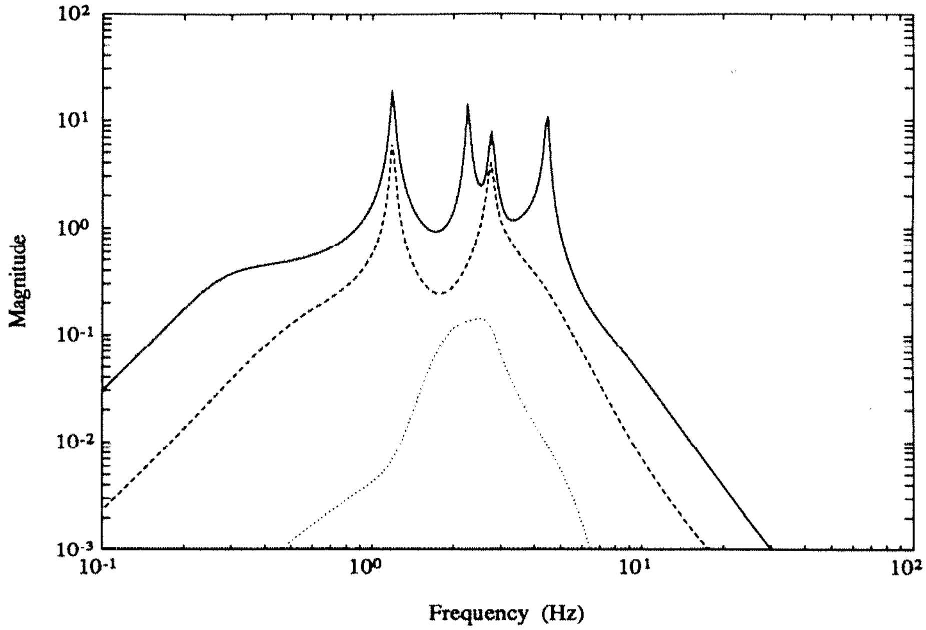

Figure 7.9: Singular Value Plot of the Loop Gain for Controller $K3am$

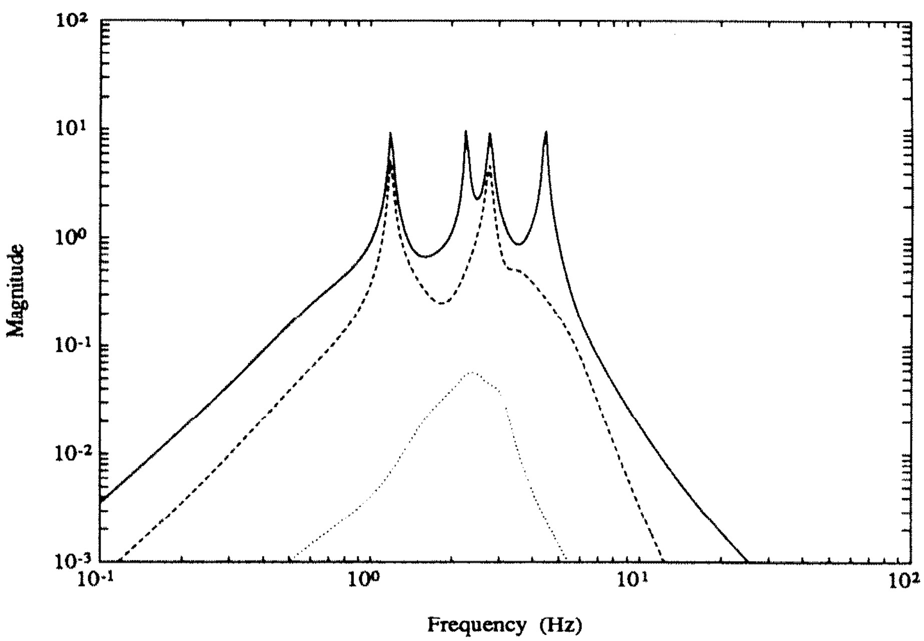

Figure 7.10: Singular Value Plot of the Loop Gain for Controller $K10am$

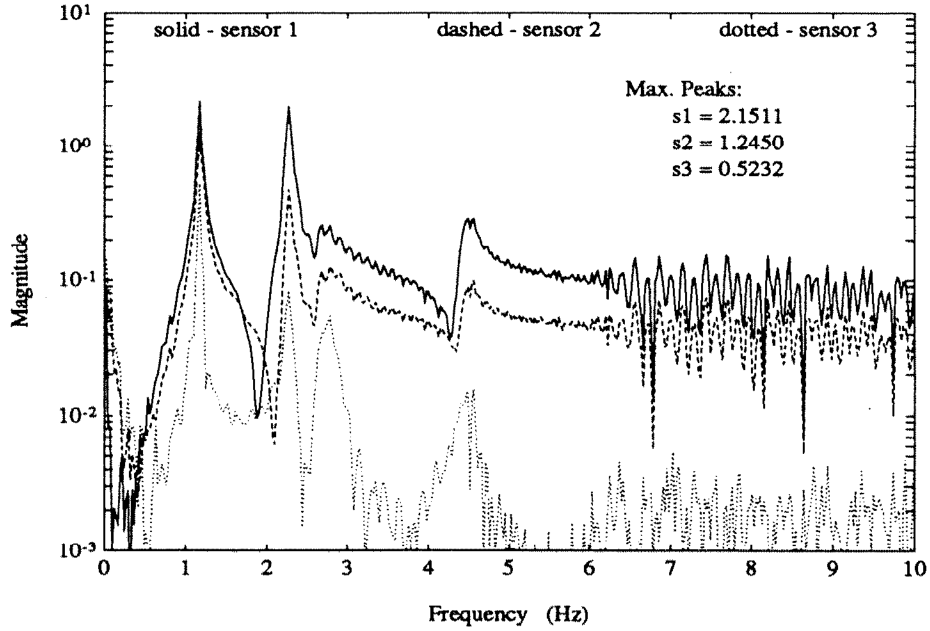

Figure 7.11: Open-loop Response of Sensors to 1-6 Hz Sine Sweep into Air 1

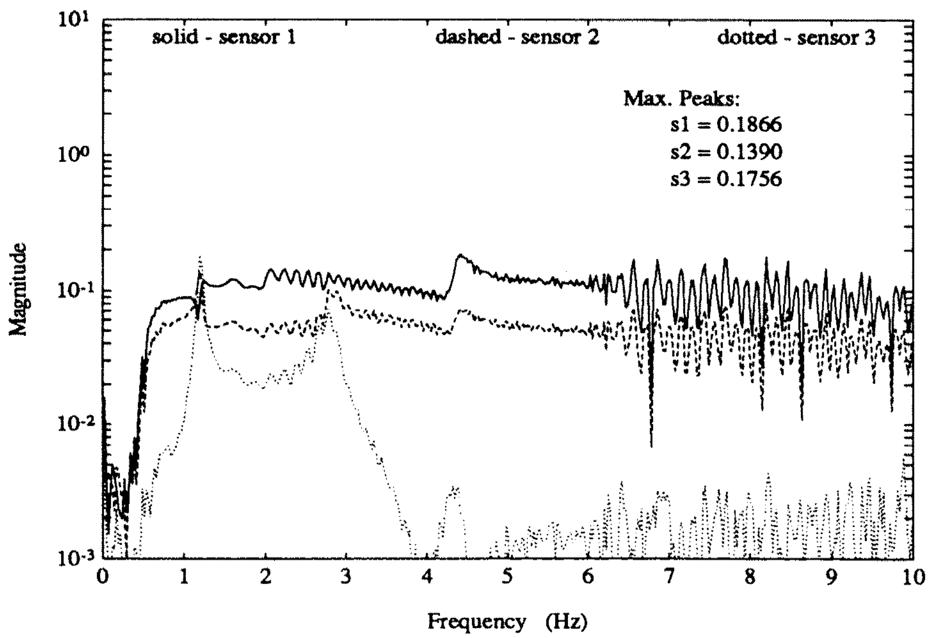

Figure 7.12: Closed-loop Response, $K1am$, of Sensors to 1-6 Hz Sine Sweep into Air 1

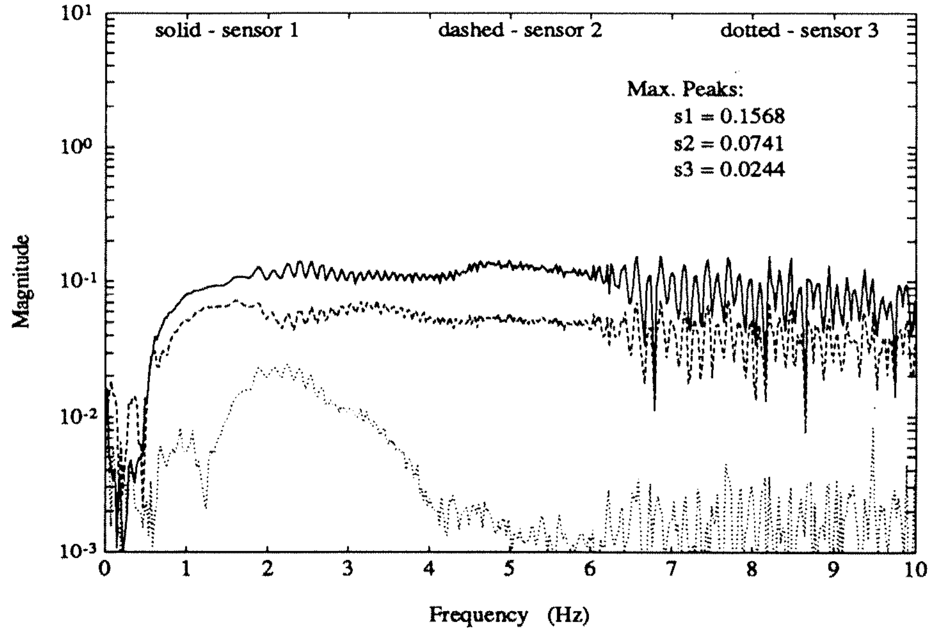

Figure 7.13: Closed-loop Response, $K3am$, of Sensors to 1-6 Hz Sine Sweep into Air 1

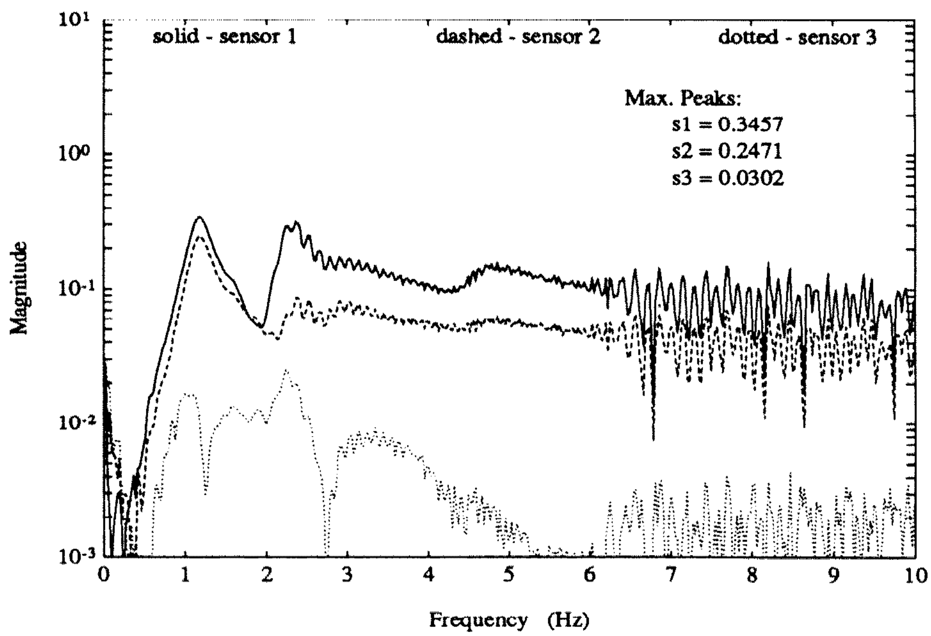

Figure 7.14: Closed-loop Response, $K10am$, of Sensors to 1-6 Hz Sine Sweep into Air 1

the designed uncertainty levels. These models can not be validated or can it be said that the "real" system lies inside this set of plant models. <u>Data can never validate a model</u> because the next set of experiments may invalidate it. All that can be said about the model sets for control designs $K3am$ through $K10am$ is that they provide an accurate description of the physical system for control design.

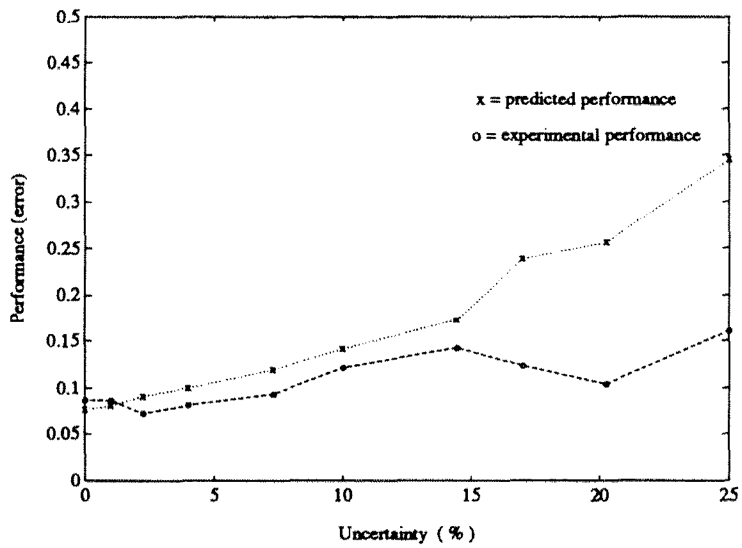

Figure 7.15: Predicted versus Experimental Performance for the Input Uncertainty Designs

Time histories of the closed-loop response of control designs $K3am$ and $K10am$ are shown in figures 7.16 and 7.17. The time response data corresponds to the frequency response data. Control laws designed with insufficient levels of uncertainty, $K1am$ and $K2am$, achieve performance levels less than predicted when implemented on the system. One can infer that the control designs are optimized for an inaccurate model. Selecting an appropriate level of uncertainty, 2.25% for this problem description, provides the highest level of performance on the structure. Increasing the input uncertainty level leads to more conservative control laws which emphasize robustness. These control laws reduce the amount of control action there by reducing the attenuation level. One can see that selection of uncertainty descriptions has a direct bearing on the performance and robustness of the control designs.

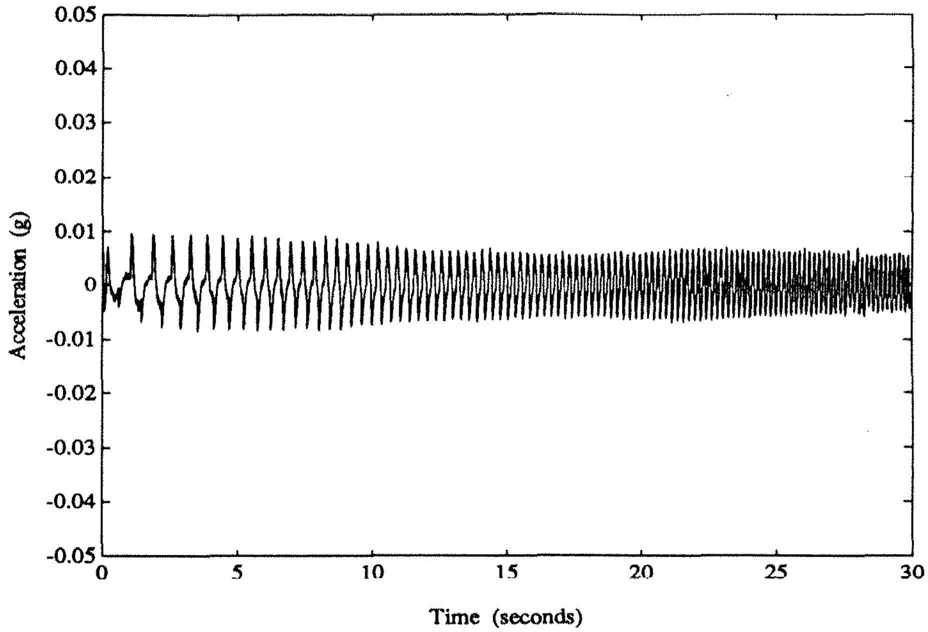

Figure 7.16: Closed-loop Time Response, $K3am$, of Sensor 1 to 1-6 Hz Sine Sweep into Air 1

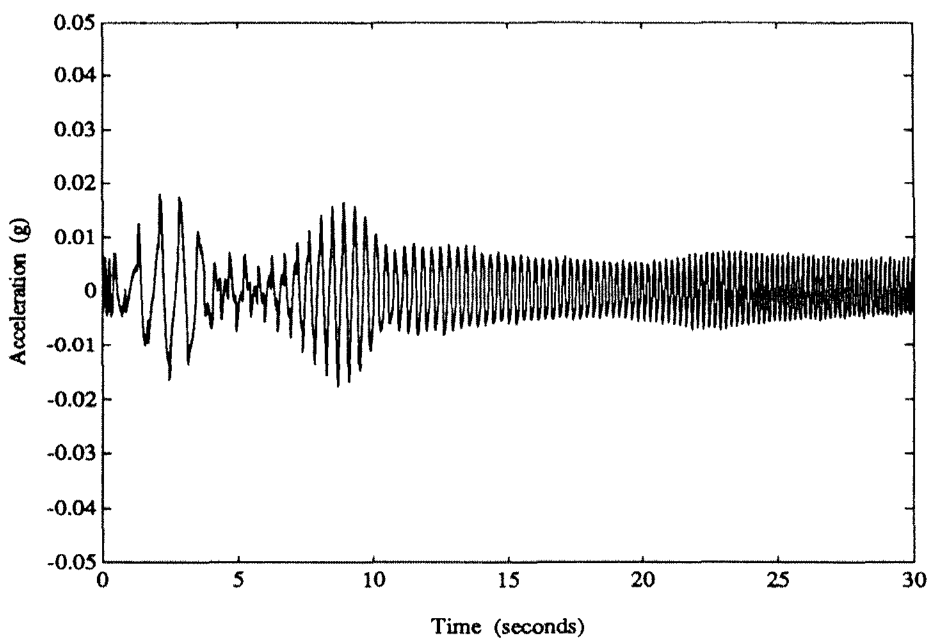

Figure 7.17: Closed-loop Time Response, $K10am$, of Sensor 1 to 1-6 Hz Sine Sweep into Air 1

7.4.3 Output Multiplicative Uncertainty

A set of control laws is synthesized with additive and output multiplicative uncertainty to account for errors in the design model. The problem formulation is based on the block diagram in figure 7.2 with the input uncertainty scaling, *actu*, set to zero. Nine control laws are formulated for the output scaling, *sensu*, varying between 0.1 and 0.5. This is analogous to the output multiplicative uncertainty varying between 1% and 25%. Each control law is designed for a specified level of output uncertainty, *sensu*, with the performance weight, *perfwt*, scaled to achieve a μ value of 1.

Control Law	Sensor Uncertainty (%)	*perfwt*	Predicted Performance	μ
$K1sm$	1.00	11.60	.086	1.03
$K2sm$	2.25	10.95	.091	0.95
$K3sm$	4.00	10.40	.096	1.05
$K4sm$	7.29	9.70	.103	1.03
$K5sm$	10.00	9.10	.110	1.06
$K6sm$	14.44	8.80	.114	1.03
$K7sm$	17.00	8.40	.119	0.96
$K8sm$	20.25	8.10	.124	1.07
$K9sm$	25.00	7.75	.129	1.09

Table 7.4.4: Parameters for Control Design with Output Multiplicative Uncertainty

The set of nine control laws uses the same noise weight, *censwt*, *magwt*, and *ratewt* as in the set of input uncertainty designs. Table 7.4.3 contains a list of parameters varied in the output multiplicative uncertainty control designs. Each control law is implemented on the structure and an experimental frequency response is generated from the air disturbance input to the three accelerometer outputs. A plot of μ as a function of frequency is shown for control laws $K3sm$ and $K10sm$ in figure 7.18. Singular value plots of the controller loop gain for these two controllers are shown in figures 7.19 and 7.20. Closed-loop experimental frequency responses of $K3sm$ and $K10sm$ are shown in figures 7.21 and 7.22. Table 7.4.3 contains the raw experimental data from the closed-loop experiments. $K1am$ is included because it was designed with zero input/output multiplicative uncertainty.

The highest performing control law, $K3sm$, achieved a performance level of 0.072.

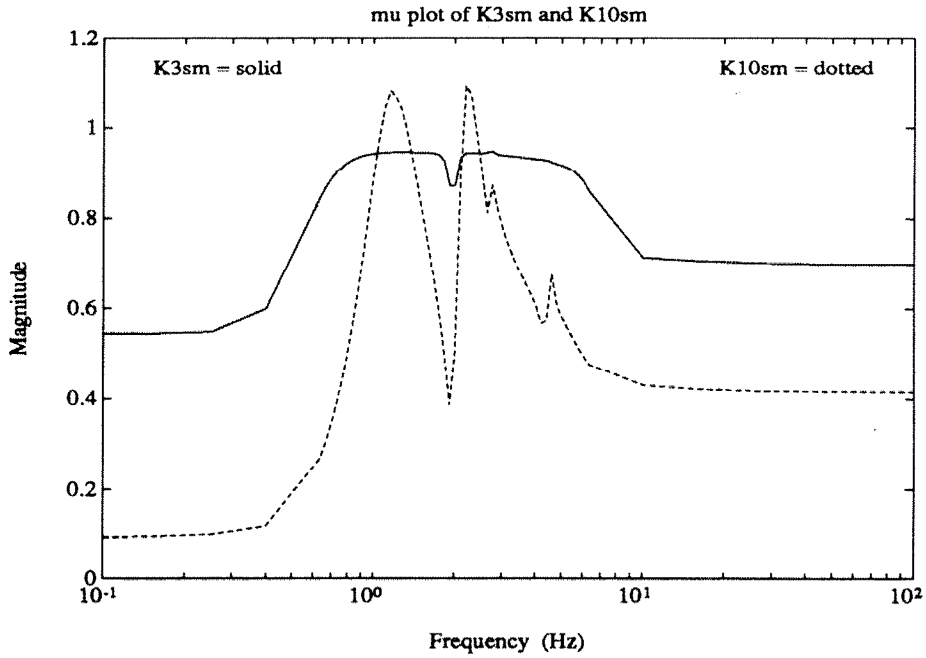

Figure 7.18: A Plot of μ for Control Designs $K3sm$ and $K10sm$

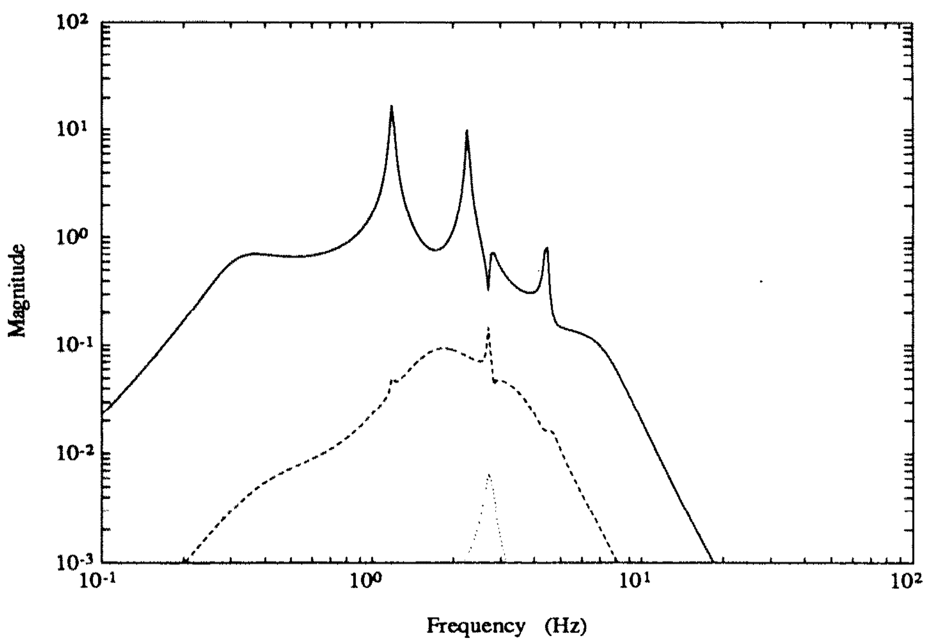

Figure 7.19: Singular Value Plot of the Loop Gain for Controller $K3sm$

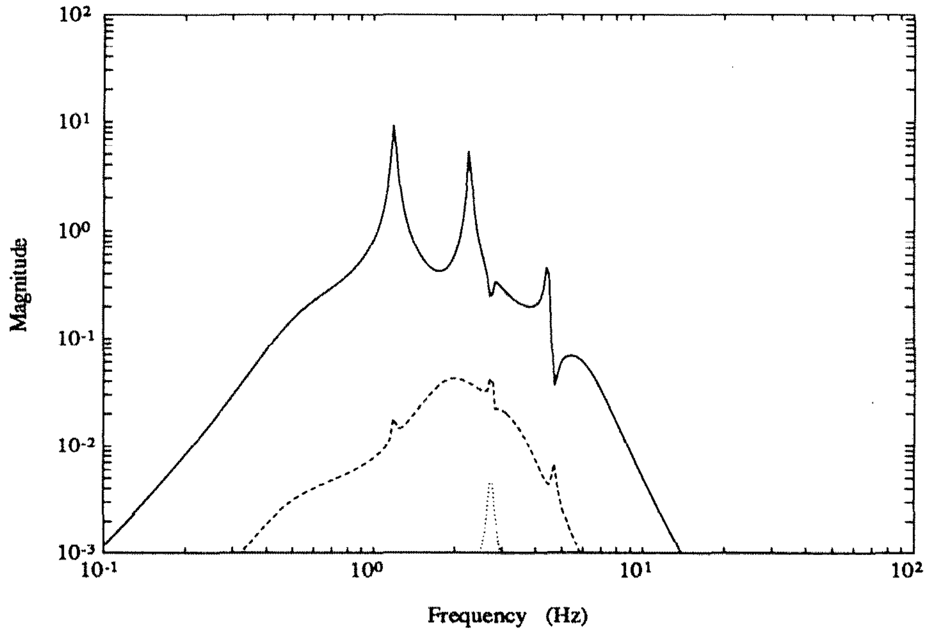

Figure 7.20: Singular Value Plot of the Loop Gain for Controller $K10sm$

Control Law	Maximum Magnitude in Frequency Range 0-10 Hz Raw Data Sensor 1	Sensor 2	Sensor 3	Experimental Performance OL:CL	Predicted Performance OL:CL
Open-loop	2.151	1.245	0.523	1.0000	1.00
$K1am$	0.187	0.139	0.176	0.087	0.077
$K2sm$	0.182	0.152	0.182	0.085	0.086
$K3sm$	0.154	0.123	0.138	0.072	0.091
$K4sm$	0.177	0.142	0.140	0.082	0.096
$K5sm$	0.180	0.138	0.127	0.084	0.103
$K6sm$	0.195	0.145	0.131	0.091	0.110
$K7sm$	0.180	0.122	0.113	0.084	0.114
$K8sm$	0.185	0.105	0.105	0.086	0.119
$K9sm$	0.208	0.124	0.047	0.097	0.124
$K10sm$	0.229	0.131	0.054	0.106	0.129

Table 7.4.5: Experimental Results of Control Designs with Output Multiplicative Uncertainty

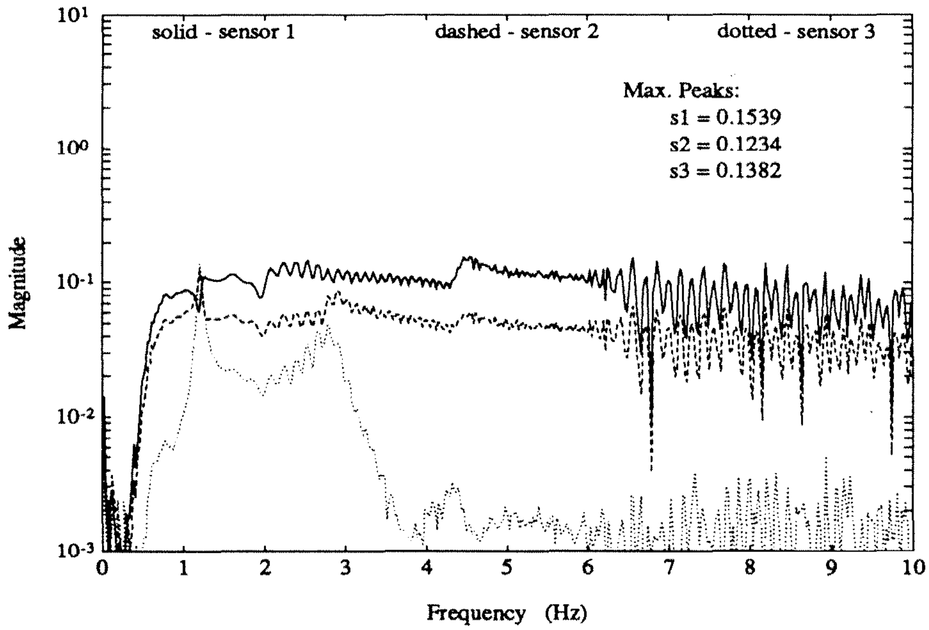

Figure 7.21: Closed-loop Response, $K3sm$, of Sensors to 1-6 Hz Sine Sweep into Air 1

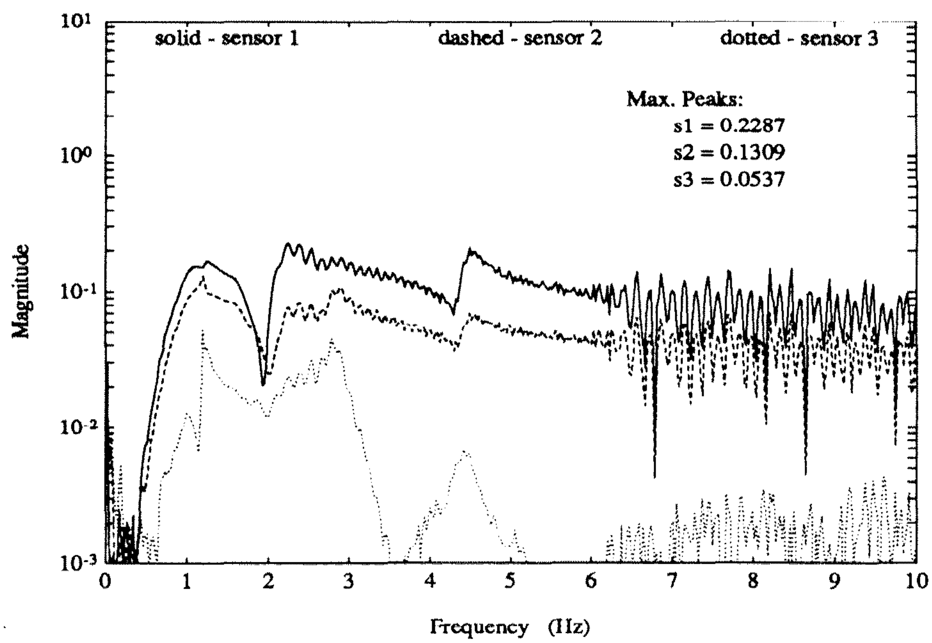

Figure 7.22: Closed-loop Response, $K10sm$, of Sensors to 1-6 Hz Sine Sweep into Air 1

$K1am$ had a performance level less than predicted and all other control laws exceeded their predicted performance. Therefore, the nominal model with output multiplicative uncertainty provides an excellent model for control design purposes. Figure 7.23 provides a comparison between the predicted performance of the model, given the designed uncertainty level and the experimental data. Note the consistent trend in the data between the theory and the experiments. As expected, increasing the output uncertainty weight increases the robustness characteristics of the control law at the expense of the performance. $K10sm$ are shown in figures 7.24 and 7.25.

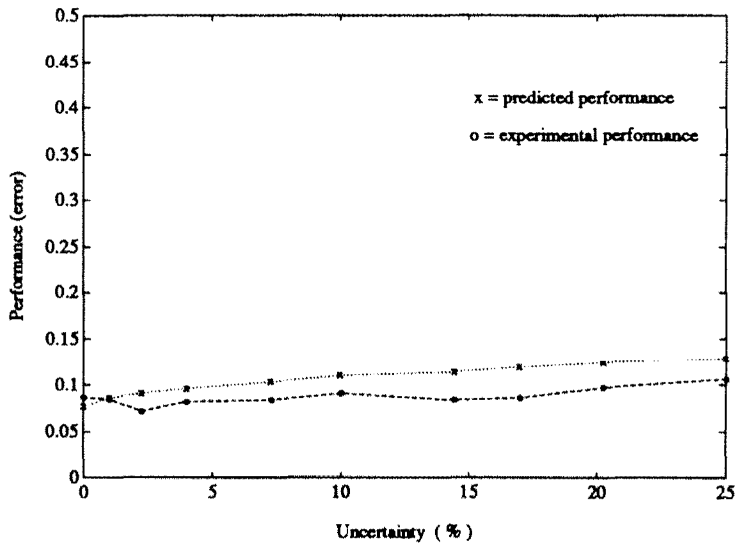

Figure 7.23: Predicted versus Experimental Performance for Output Uncertainty Designs

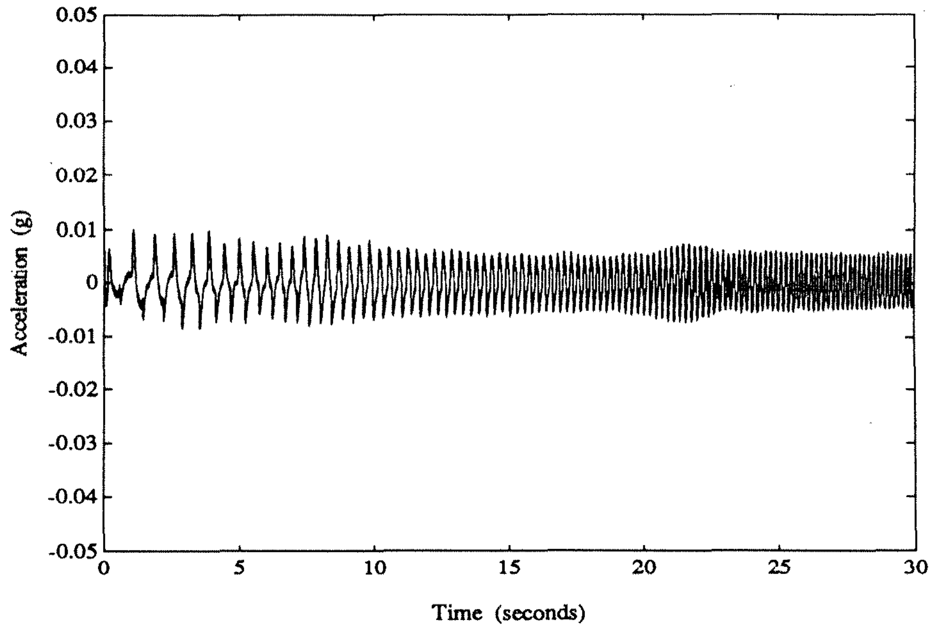

Figure 7.24: Closed-loop Time Response, $K3sm$, of Sensor 1 to 1-6 Hz Sine Sweep into Air 1

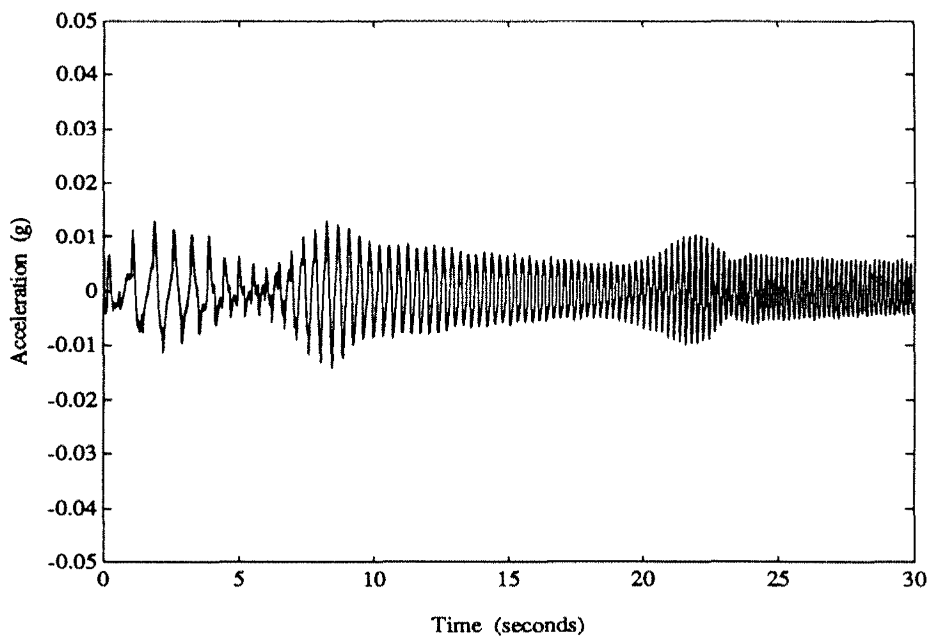

Figure 7.25: Closed-loop Time Response, $K10sm$, of Sensor 1 to 1-6 Hz Sine Sweep into Air 1

7.5 Summary

Representing the physical system with a nominal model and an uncertainty description provides an excellent design model for use in the μ-synthesis techniques. The addition of uncertainty models is required because the inclusion of sensor noise models alone will not provide the required robustness at desired locations in the plant. The series of control laws developed using input uncertainty reflect a strong dependence of the control laws on accurate input signals to the system. As the input uncertainty level is increased in the control design model, there is a marked decrease in the closed-loop performance. Control designs for the phase I flexible structure are less sensitive to output uncertainty, which provides a very accurate description of the system when combined with the nominal model for control design. The output multiplicative control designs exhibit better performance both theoretically and experimentally as a function of uncertainty. The theoretical and experimental results indicate that uncertainty modeling plays a major role in the tradeoff of performance requirements and robustness properties of synthesized control laws. Accurately accounting for model error and its location in the problem formulation has a direct bearing on the achievable performance of the control design.

Chapter 8

Control of Flexible Modes in the Controller Crossover Region

Attributes of flexible structures require the control design to attenuate vibration in one frequency range while not destabilizing other natural frequencies outside this range. The bandwidth of the control design is often dictated by the dynamics of the actuator and sensors. This chapter investigates the design of control laws to achieve performance in one frequency range while being robust to unmodeled, closely spaced modes in the region crossover. Control laws are synthesized to investigate this issue on the phase I Caltech experimental flexible structure. They are designed to crossover over between two closely spaced, lightly damped modes, the first set of bending modes and the first torsional mode.

8.1 Control Objectives

The control objective is to attenuate the vibration of select modes of the structure at the accelerometer locations. The input disturbance due to air actuator 1 blows directly on sensor 1. The disturbance takes the form of a sinusoid sweep through the frequency range of 1 to 6 Hz. The performance requirement is to minimize the maximum frequency response of the first two bending modes of the closed-loop system in comparison with their open-loop response. This is to be achieved at the same time as being robust to unmodeled higher frequency modes present in the structure. The performance criteria is defined as minimizing $|| \cdot ||_\infty$ norm of the transfer function from the input disturbance to sensors.

8.2 Uncertainty Descriptions

The uncertainty descriptions determine the tradeoff between achievable performance and robustness of the control design. We will restrict ourselves to frequency domain descriptions of uncertainty for the control design model.

An additive uncertainty, $W_{additive}$, is included in the problem formulation to account for the unmodeled high frequency dynamics of the structure. Because it is desirable to gain stabilize the first torsional mode at 2.26 Hz, the additive uncertainty weight is selected to encompass the frequency domain peak of the mode. A plot of the additive uncertainty weight and the phase I transfer functions between voice coil actuator 1 and the three sensors is shown in figure 8.1. The uncertainty level is selected so that the phase component of the first torsional mode at 2.25 Hz is modeled as being totally unknown. One would expect the control methodology to formulate a design for which the torsional mode has the same open-loop and closed-loop response since there is no knowledge of the first torsional mode assumed in the model. Several control designs are synthesized by varying the additive uncertainty weight to investigate the effect of the additive weight level on the control design and closed-loop performance. The additive weight description is:

$$W_{additive} = 800 \frac{(s+3)^5}{(s+30)^5} \tag{8.1}$$

The additive uncertainty weight associated with sensor 3 is scaled by 0.25 since the response of the structure in this channel due to air actuator 1 is a factor of 4 below sensors 1 and 2. A constant input multiplicative uncertainty of 4% is used in the control designs. This weight is based on results presented in the previous chapter [BalDoy3].

8.3 Problem Formulation

Control designs are formulated using the μ-synthesis methodology to address the issue of crossing over the closed loop design in a frequency range with numerous flexible modes.

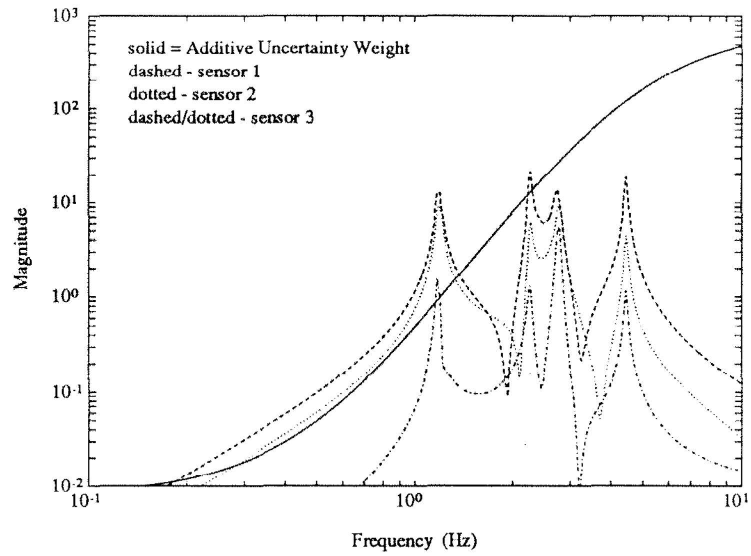

Figure 8.1: Frequency Response of Actuator 1 to All Sensor and the Additive Uncertainty Weight

There are both performance and robustness requirements that must be satisfied by the control design and hence are included in the problem formulation.

There are a number of performance requirements associated with the control laws. The actuator force and rate levels must be limited to have them operate in their linear range. The actuator magnitude weight is determined by its maximum output of $\pm$ 3 lbs and the rate weight corresponds to its 60 Hz bandwidth. The performance objective is to minimize the maximum response of the first two bending modes in the frequency domain. To achieve this, the performance weight for vibration attenuation is selected as a constant scaling on the sensor transfer function outputs. These transfer functions are first scaled to one, then the performance weight (*perfwt*) is used to determine the amount of attenuation of the frequency domain peaks. The input disturbance enters via air actuator 1, which blows directly on sensor 1. A model of the excitation, $\frac{10}{s+10}$ is included in the control problem formulation. A block diagram of the problem formulation is shown in figure 8.2.

For μ-synthesis , the block diagram is reformulated into the general linear fractional framework. A diagram of this is shown in figure 8.3. The dimensions of the Δ blocks are: 3×3 for Δ_1, 3×3 for Δ_2 and 6×4 for Δ_3. Δ_1 is associated with the additive uncertainty,

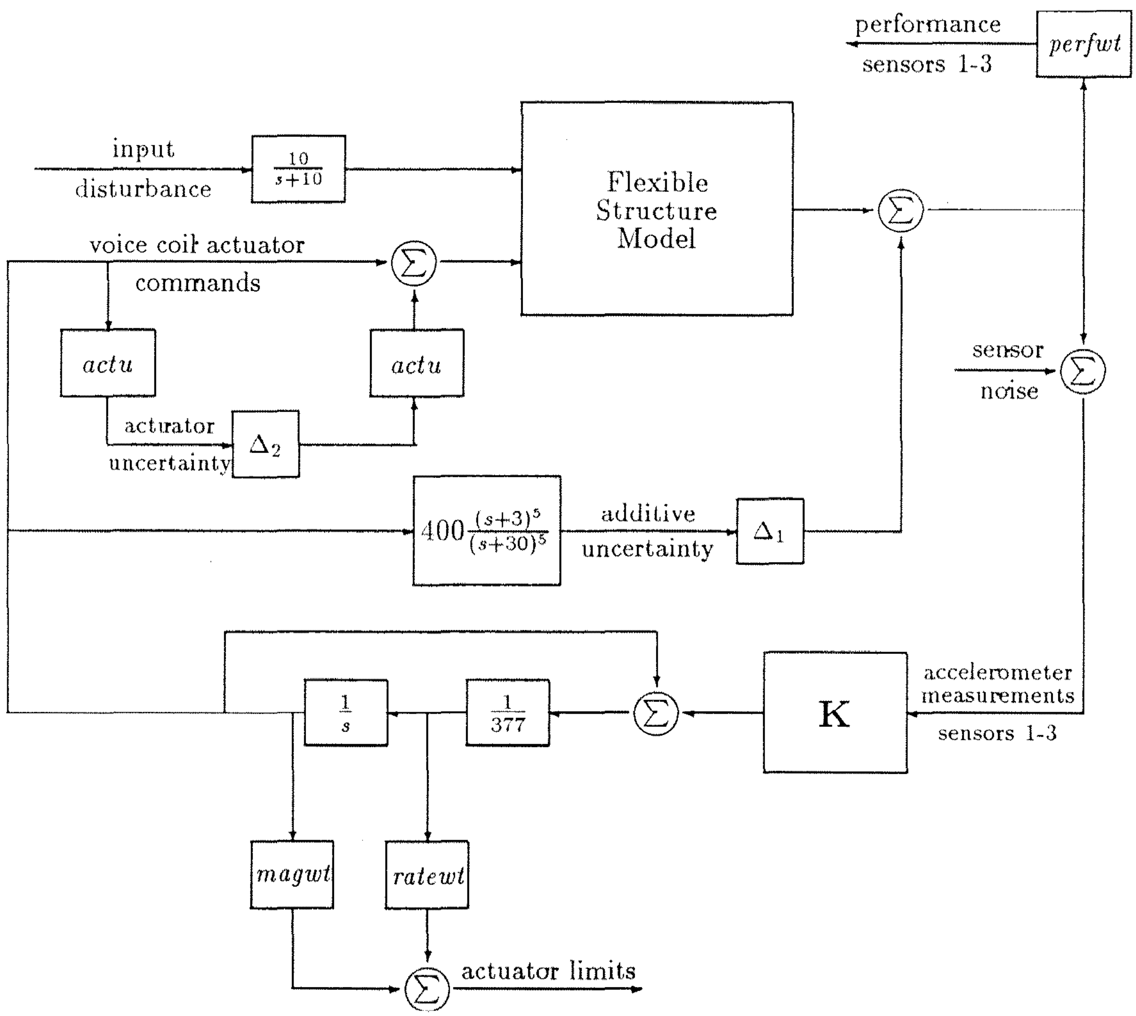

Figure 8.2: Block Diagram of the Crossover Control Problem

Δ_2 with the actuator uncertainty and Δ_3 is the performance block. All the Δ blocks are full blocks. The problem formulation is similar to the formulation in chapter 7. The additive uncertainty dictates the region in which the control law is to roll off.

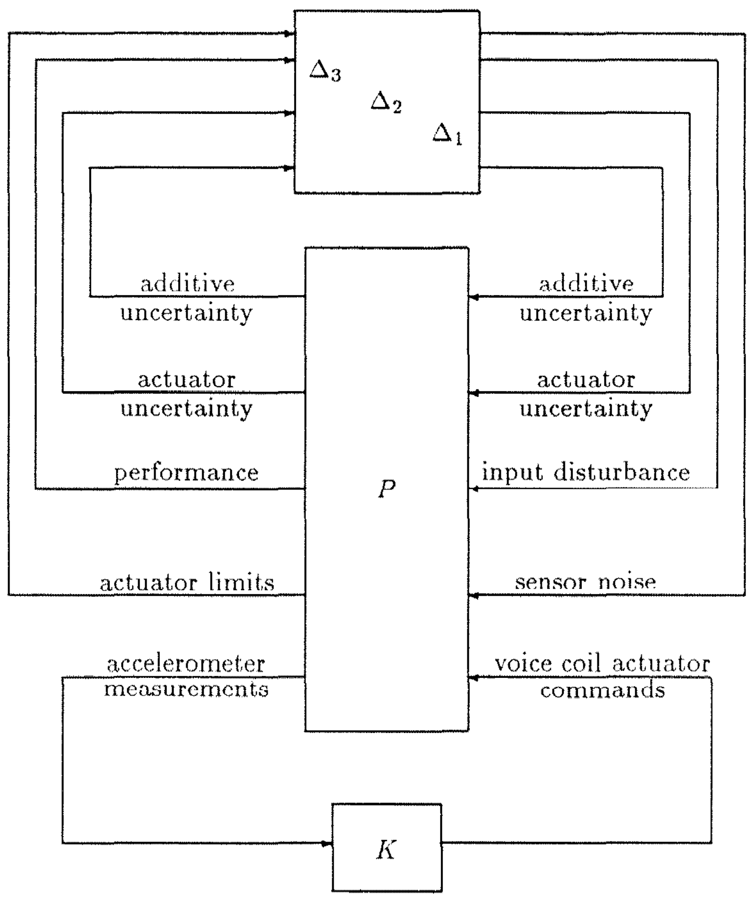

Figure 8.3: LFT for Crossover Control Problem

8.4 Control Design

Six different control designs are formulated for the Caltech flexible structure experiment. The first three, $K10n$, $K11n$, and $K12n$ use the complete six mode, transfer function model, *air_as123.sys*, developed from the system identification techniques. Its state space description is given in Appendix A. The second set of three control designs, $K13n$,

Design Name	Structural Model	Designed for Performance *perfwt*	Additive Unc. Weight Scaling	Theoretical Performance OL:CL	Experiment Performance OL:CL
K10n	*air_as123.sys*	2.8	1.0	0.357	0.181
K11n	*air_as123.sys*	4.7	0.5	0.213	0.101
K12n	*air_as123.sys*	6.9	0.1	0.145	0.062
K13n	*air_mod12.sys*	2.7	1.0	0.370	0.208
K14n	*air_mod12.sys*	5.5	0.5	0.182	0.105
K15n	*air_mod12.sys*	6.4	0.1	0.156	unstable

Table 8.4.1: Parameters for Control Designs in Crossover Region

$K14n$, and $K15n$, use only a model of the first two bending modes, *air_mod12.sys*. This is a truncated version of *air_as123.sys*. There is a one to one correspondence between the uncertainty descriptions and performance requirements between each of the three designs in the control problem formulation. The three different designs correspond to additive uncertainty levels of 100%, 50%, and 10% of the nominal uncertainty description. Table 8.4.1 lists the parameters used in the design. In the synthesis of each control design, the vibration attenuation level is scaled to provide a μ value of one for the closed loop system. Performance is measured as a ratio of closed-loop frequency domain response to the open-loop response for the first two bending modes in the frequency range of 0.1 and 2.0 Hz.

The goal of the experiments is to determine the interaction between modeling and uncertainty descriptions in the control design process. The first set of control designs uses the full six mode model of the structure combined with the additive uncertainty description. These control designs should stabilize the structure and achieve the performance levels designed for them based on the results in chapter 7. The control designs have considerable knowledge of the physical system inside the control bandwidth and at the crossover region. These designs indicate the benefit of accurate modeling for both performance objectives and stability requirements.

The second set of control designs assumes only knowledge of the first two bending modes to be controlled. The additive uncertainty must account for all other dynamics in the system that are not modeled. The control design methodology cannot take advantage of any knowledge of the system in the crossover region or about higher frequency modes as in the six mode model designs. The best these control designs can do is to achieve the performance objective within the control bandwidth and not destabilize the higher frequency modes. These two sets of designs are extreme examples of the models traditionally available to the control designer. The design model usually falls between these two, with some knowledge of modes in the crossover region and higher but limited accuracy.

8.5 Results

The first set of three control designs, based on the six mode model, achieved the performance objective of attenuation of the first two bending mode peaks. It is of interest to note that the control designs for the six mode model attenuate the first torsional model of the structure. In fact, one will notice in figure 8.1 that the nominal additive uncertainty does not completely cover the first torsional mode. Control design $K10n$ takes advantage of the information about the torsional mode to attenuate its peak. A singular value plot of the loop gain for control laws $K10n$ and $K12n$ are shown in figures 8.4 and 8.5. The loop gain of $K10n$ at the first torsional is below one indicating no additional performance will be achieved. Implementing this design on the structure, attenuates the first torsional mode, therefore the damping value associated with this mode in the model must be higher than in the actual structure.

As the additive uncertainty is reduced there is significant attenuation of both the first torsional and higher modes of the structure. Control design $K12n$ attenuates all six flexible modes of the structure as seen in figure 8.11. In the loop gain plot of $K12n$ the higher modes of the structure have loop gain larger than 1, indicating attenuation of these modes by the control design. The three control laws designed based on the six mode model, $K10n, K11n$, and $K12n$, use knowledge of the full model to attenuate not only the first two bending modes but higher frequency modes as the level of additive uncertainty is decreased. Due to the accuracy of the six mode model, the additive uncertainty level isn't critical to the robustness of the control designs.

Control designs $K13n, K14n$, and $K15n$ are based on the two mode model, *air_mod12.sys*. These control laws are not able to take advantage of any knowledge of higher frequency modes because they are not included in the design model. Singular value plots of the loop gain for control laws $K13n$ and $K15n$ are shown in figures 8.6 and 8.7. The loop gain of control law, $K13n$, is above one only, at the set of bending modes. The control design rolls off sufficiently fast to gain stabilize the first torsional and higher modes. This is exactly what is observed in the closed-loop experiment shown in figure 8.12. Notice that the first bending modes are attenuated but that the first torsional mode has the same response level as open-loop. The control law $K13n$ needs to gain stablize these modes since it has no additional knowledge of the system dynamics. Control law $K14n$ is designed for half the level of the nominal uncertainty and its performance weight is increased by a factor of two. Its closed-loop response, shown in figure 8.13, achieved twice the performance of $K14n$. Note that there is no attenuation of the response of the first torsional mode. Control law $K15n$ is designed based on an additive uncertainty level of one-tenth of its nominal value. This level of uncertainty is not sufficient to encompass the peaks of the first torsional and high frequency flexible modes. The loop gain plot of control law $K15n$, figure 8.7, shows a loop gain greater than one at the first torsional and higher modes. Unlike $K12n$, $K15n$ has no phase or gain information about the system response above the first bending modes. One would suspect that $K15n$ would be unstable on the model, which in fact it is. $K15n$ is also unstable when implemented on the structure as shown in figure 8.14.

The control designs achieved their goal of reducing the frequency domain peaks of the first two bending modes. In the case of the three control designs with the full six mode model of the structure, it is seen that as the additive uncertainty weight is scaled down, the torsional mode is attenuated by the control law. Attenuation of the torsional mode by control design $K12n$ is very evident in figure 8.11. However, this is not the case for the control designs synthesized with only a model of the first two bending modes. In fact, when the additive uncertainty weight is reduced to one-tenth its original value in control law $K15n$, the first torsional mode is unstable (figure 8.14). These results imply that the control designs based on the six mode model of the structure rely on information about the higher frequency modes. When these modes are not known sufficiently well, the control design destabilizes them.

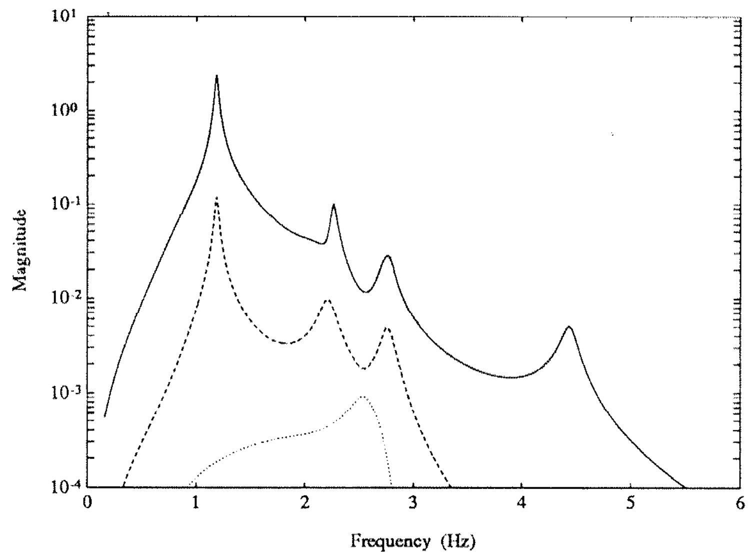

Figure 8.4: Singular Value Plot of Loop Gain for Control Law $K10n$

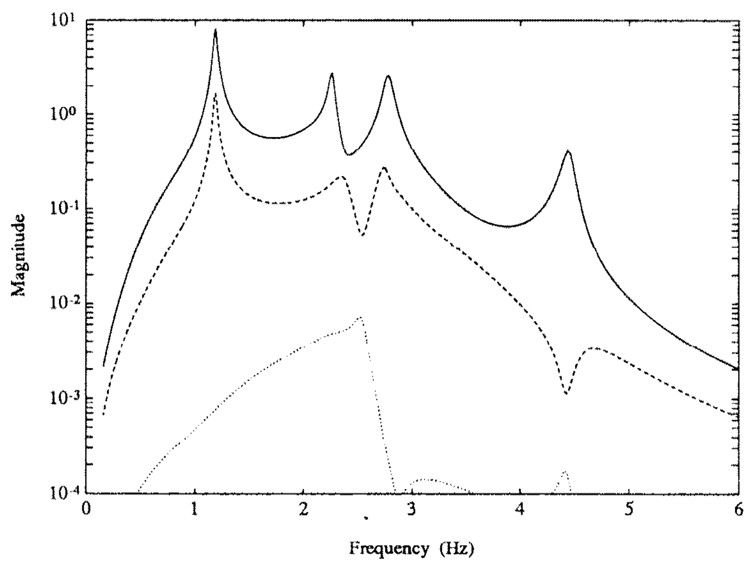

Figure 8.5: Singular Value Plot of Loop Gain for Control Law $K12n$

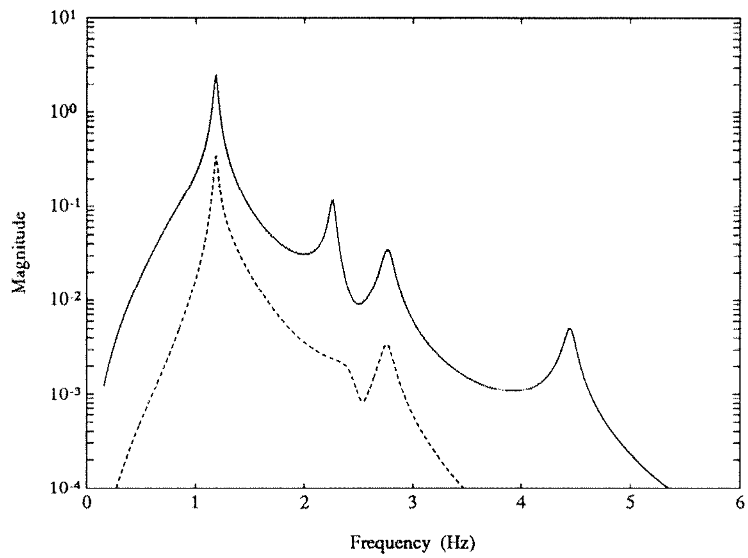

Figure 8.6: Singular Value Plot of Loop Gain for Control Law $K13n$

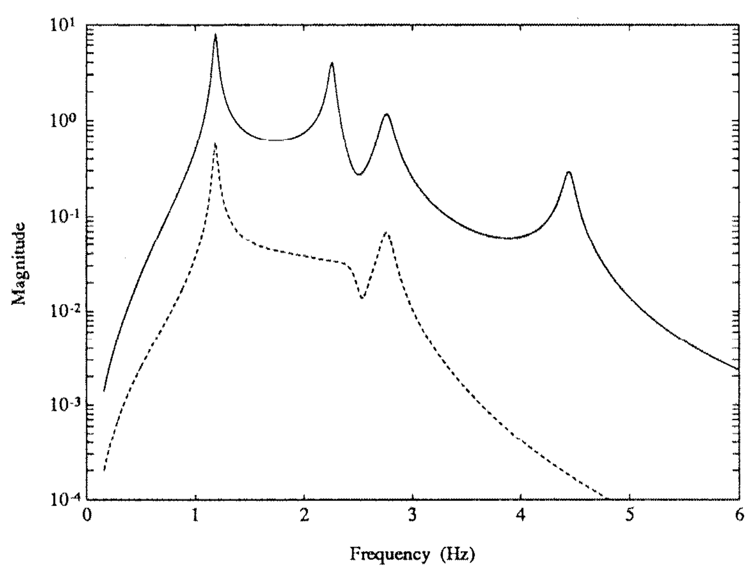

Figure 8.7: Singular Value Plot of Loop Gain for Control Law $K15n$

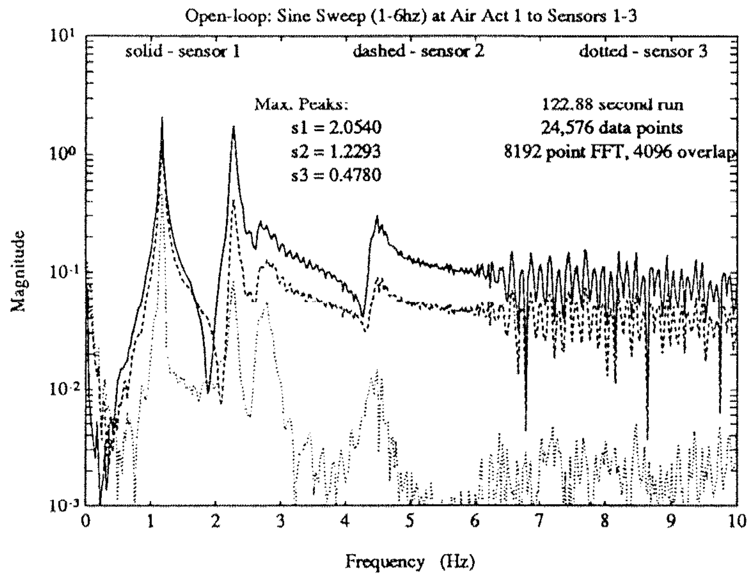

Figure 8.8: Open-loop Frequency Response of Caltech Flexible Structure to Air Actuator 1 Excitation

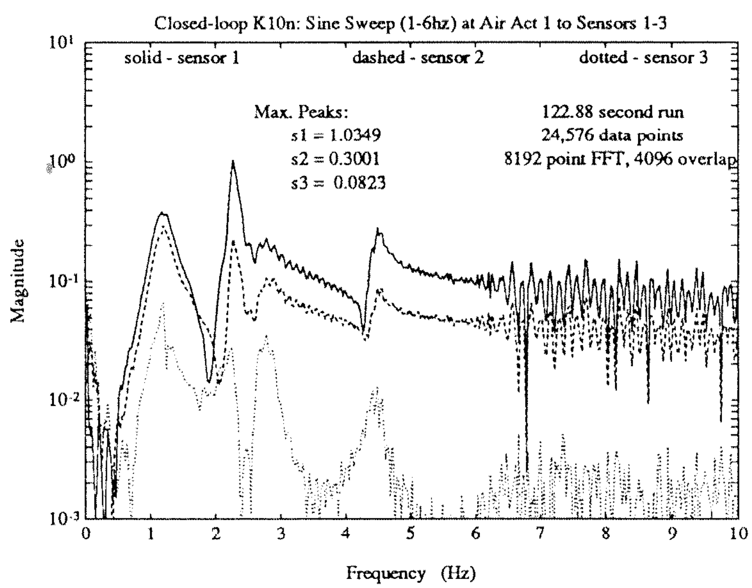

Figure 8.9: Closed-loop Frequency Response of Control Design K10n

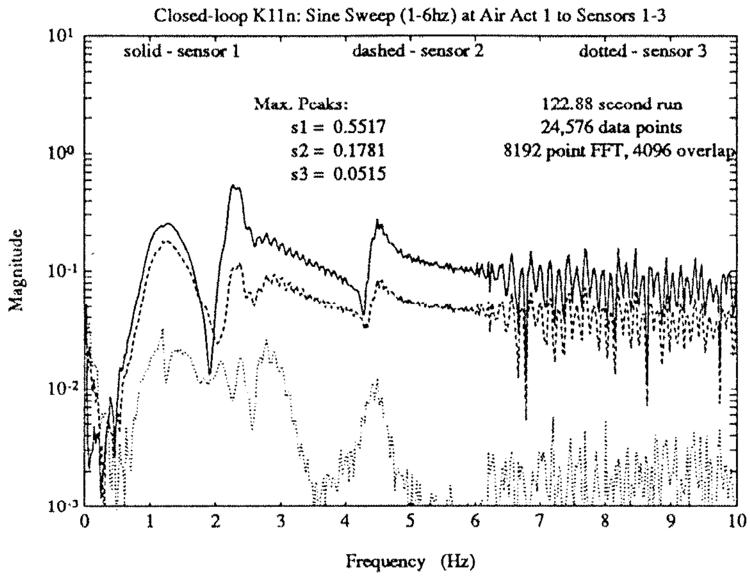

Figure 8.10: Closed-loop Frequency Response of Control Design K11n

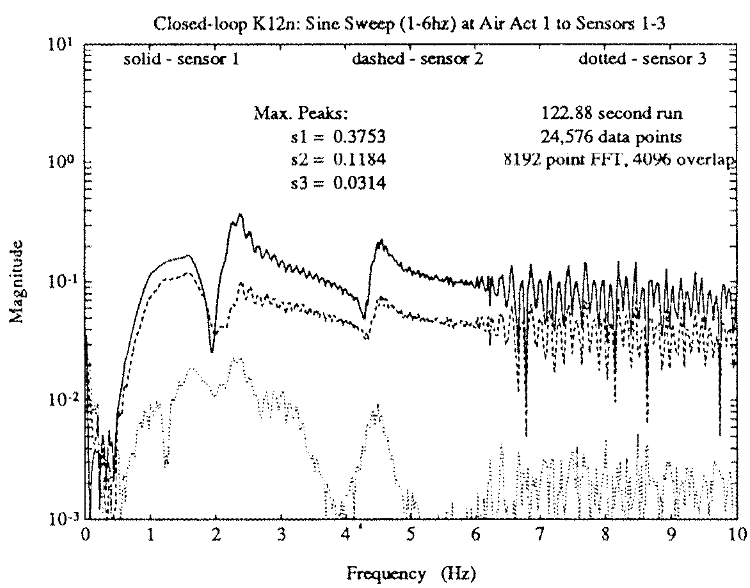

Figure 8.11: Closed-loop Frequency Response of Control Design K12n

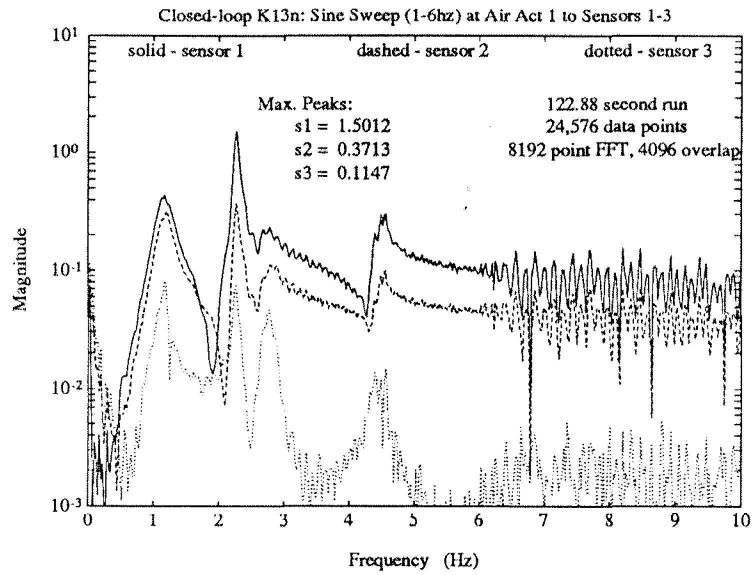

Figure 8.12: Closed-loop Frequency Response of Control Design K13n

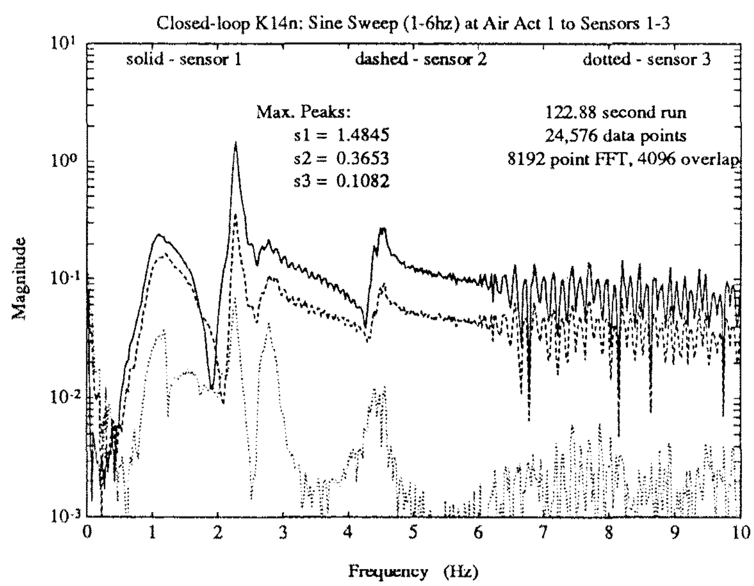

Figure 8.13: Closed-loop Frequency Response of Control Design K14n

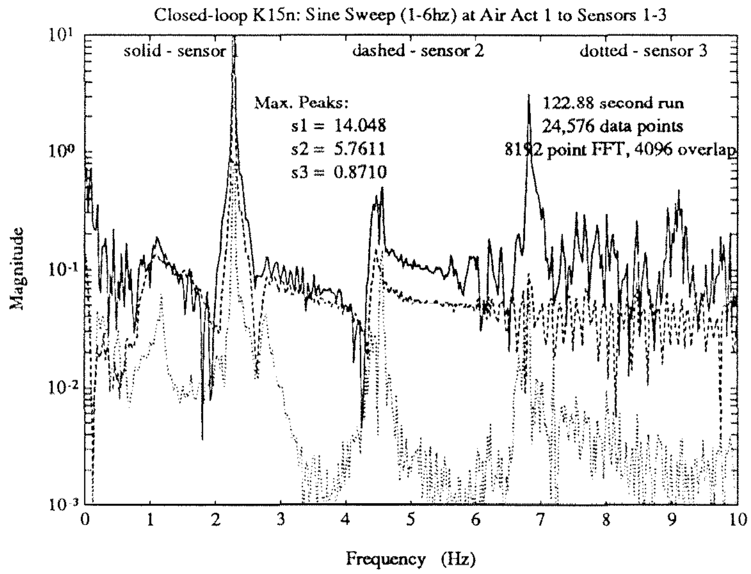

Figure 8.14: Closed-loop Frequency Response of Control Design K15n

8.6 Conclusion

A number of control laws are designed, which roll off in a region that has numerous flexible modes and still achieves some level of vibration attenuation in the modes being controlled. An additive uncertainty weight is used in the problem formulation to require that the control laws gain stabilize the first torsional mode of the experimental structure. The control laws synthesized using the full six mode model, take advantage of the knowledge of these modes to achieve improved vibration attenuation of the first two bending modes along with the first torsional mode. This is very evident as the size of the additive uncertainty weight is reduced.

Control laws synthesized using only the first two bending modes provided significant attenuation of these modes without affecting the first torsional mode. In fact, the first torsional mode has the same frequency domain peak for the open loop and closed loop cases when it is not destabilized. It is seen that inadequate representation of the higher frequency modes by uncertainty, in the case where the additive uncertainty is scaled down by 0.1 (K15n), results in a control design that destabilizes the higher frequency modes.

The importance of accurate uncertainty modeling is noted as the fidelity of the design model is reduced. The uncertainty descriptions must be sufficiently large to require the control design to gain stabilize unmodeled modes. The additive uncertainty level is of lesser importance when models of the higher frequency modes are available to the designer.

It is of interest to note that provided a significant amount of uncertainty is included in the model, the synthesized control design has sufficient robustness for higher levels of uncertainty. The robustness and performance of control design degrades gracefully. However, if too little uncertainty is included in the design model, destabilizing control laws may be synthesized. This is an advantageous property of the μ-synthesis methodology that needs further examination.

Chapter 9

Noncollocated Versus Collocated Control Design: Benefits and Limitations

Collocated control is often taken to be the solution to vibration attenuation in large space structures. One benefit of this approach is that SISO control laws can be synthesized that are robust and significantly attenuate vibration at their location. Collocated control is limited by the amount of force able to be exerted on the structure and its ability to achieve performance objectives at other sensor locations on the structure. Noncollocated control takes advantage of measuring the exact quantity at the sensor locations to be controlled. It is constrained by the actuators having to attenuate vibration at sensor locations through a flexible structure.

Control designs using noncollocated and collocated sensors and actuators are synthesized for the phase II flexible structure to investigate these issues. The first design uses the voice coil actuators to attenuate vibration of the third story of the structure, which is excited by proof mass actuator 1. The proof mass actuator 1 is collocated with sensor 4. This design shows the benefit of measuring the signals to be controlled and limitations of acting through a flexible structure. The second design employs the proof mass actuators to attenuate vibration at collocated sensors. The disturbance to the structure enters through voice coil actuator 1. The achievable performance of the proof mass actuators is constrained by the force it is able to impart on the structure and by its linearity across frequency.

9.1 Control Objective

The performance objective is to attenuate the vibration of sensors 4, 5, and 6 mounted to the third story platform. A diagram of the phase II structure and sensor locations is provided in figure 4.2. The disturbance enters at proof mass actuator 1, which is collocated with sensor 4, for the noncollocated design with the voice coil actuators used for control. The collocated control design is excited by voice coil actuator 1 with the proof mass actuators used for control. The input disturbance signal has all its energy concentrated between 0.2 and 12.7 Hz, with a one pole roll off at 1 Hz. The performance criteria is defined as minimizing the $||\cdot||_\infty$ norm of the transfer function from the input disturbance to sensors 4, 5, and 6.

9.2 Uncertainty Descriptions

An additive uncertainty is included in the problem formulation and performs three functions: it accounts for the unmodeled high frequency modes, limits the control bandwidth and describes model errors inside the control bandwidth. The additive uncertainty weight for the noncollocated control design, using the voice coil actuators for control, is given by

$$W_{additive\_1} = 5\frac{(s+25)^2}{(s+250)^2} \tag{9.1}$$

A plot of the additive uncertainty weight and the phase II transfer functions between voice coil actuator 1 and sensors 4, 5, and 6 is shown in figure 9.1.

The collocated control design employs the proof mass actuators for control. In spite of the local feedback loop on the proof mass actuators, there is considerable variation in the output displacement of the actuators above 5 Hz. The additive uncertainty weight is selected to limit the control bandwidth to 7 Hz to limit high frequency excitation. The weighting function is given by

$$W_{additive\_2} = 1.2\frac{(s+25)^2}{(s+500)^2} \tag{9.2}$$

A plot of the $W_{additive\_2}$ for the proof mass control designs and the transfer function between proof mass actuator 1 and sensors 4, 5, and 6 is given in figure 9.2. Note that the transfer functions between proof mass actuator 1 and sensors 5 and 6 are similar due to the symmetry of the phase II flexible structure.

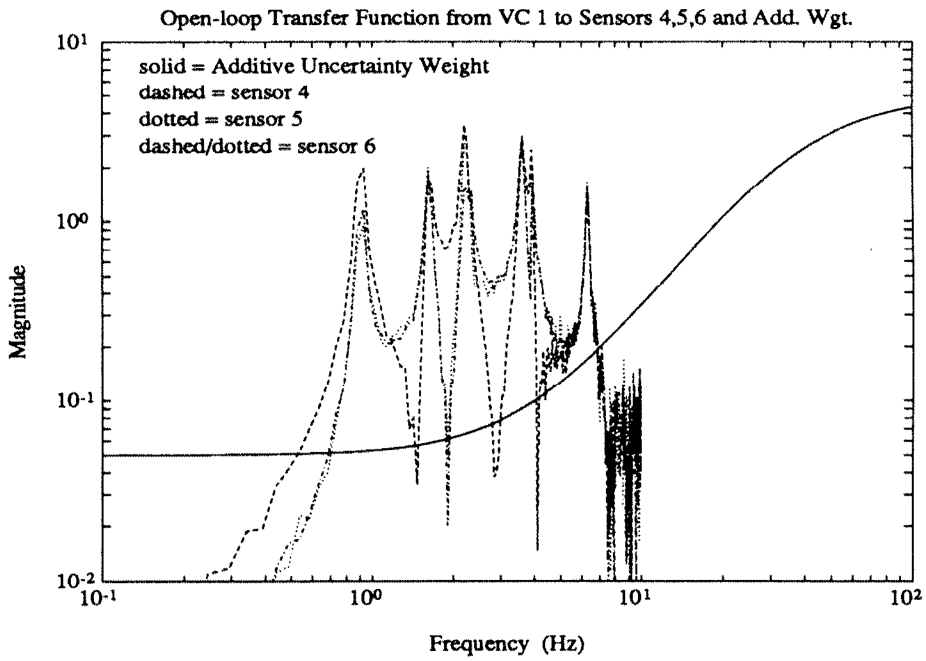

Figure 9.1: Transfer Functions from VC 1 to S4, S5, and S6 and Additive Uncertainty for Noncollocated Control Design

9.3 Problem Formulation

Control designs are formulated using the μ-synthesis methodology to address the issue of noncollocated versus collocated control design. Both control designs employ additive uncertainty to account for model error. The voice coil (VC) actuators are used for control purposes in the noncollocated problem formulation. The magnitude of the VC actuators is constrained to ± 3 lb of force for $\pm 5V$ input signals included in the noncollocated problem formulation. The local feedback loop around the proof mass actuators used in the collocated control design requires the control laws to command displacement of the moving mass. The stroke limit on the moving mass, ± 1.0 in., is translated into a magnitude bound of 1500 on the proof mass actuator commands. These constraints on

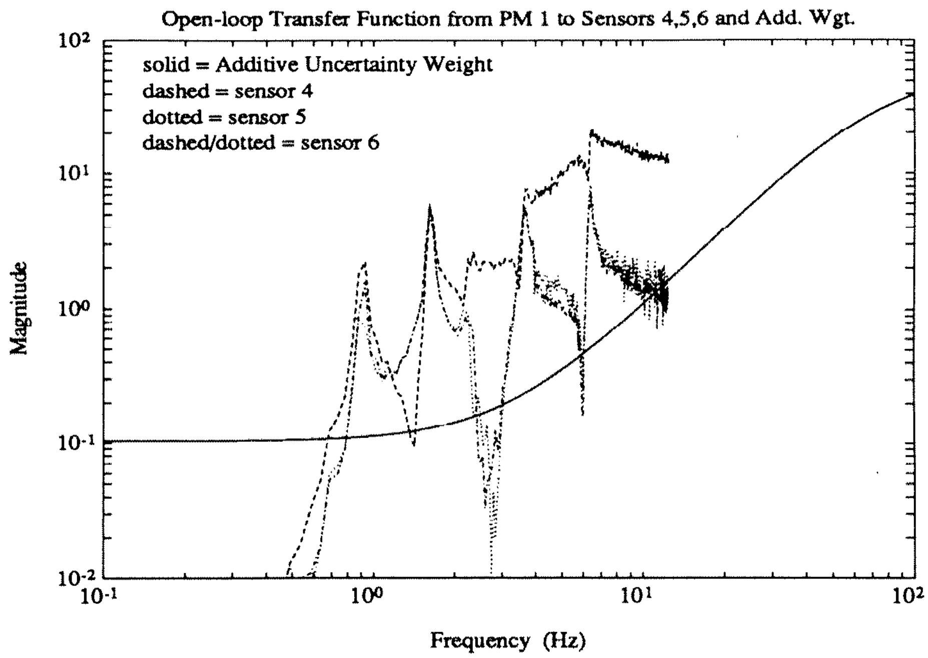

Figure 9.2: Transfer Functions from PM 1 to S4, S5, and S6 and Additive Uncertainty for Collocated Control Design

the actuators are included in the problem formulation as *magwt*.

The input disturbance in both designs is modeled as a white noise signal filtered by $\frac{6.2}{s+6.2}$. The $||\cdot||_\infty$ norm of the transfer function between the disturbance input to the sensor output represents the performance objective in the control problem formulation.

9.3.1 Noncollocated

In the noncollocated control design problem, the transfer function between the input disturbance at proof mass actuator 1 and sensor 4 rolls up like an s^2 response between 1 and 8 Hz. This is seen in figure 9.2. Based on the initial control designs, the voice coil actuators are only able to affect the flexible modes of the structure. These actuators are of limited use at other frequency points within the controller bandwidth. Therefore, only attenuation of the resonant peaks is specified in the performance criteria. Sensors 4, 5, and 6 are filtered by $\frac{225}{(s+15)^2}$ to weigh the resonant peaks of the structure equally and scale them accordingly for performance. These are defined by *perfwt* in the control problem block diagram. A sensor noise level of 2×10^{-3} is included in the design.

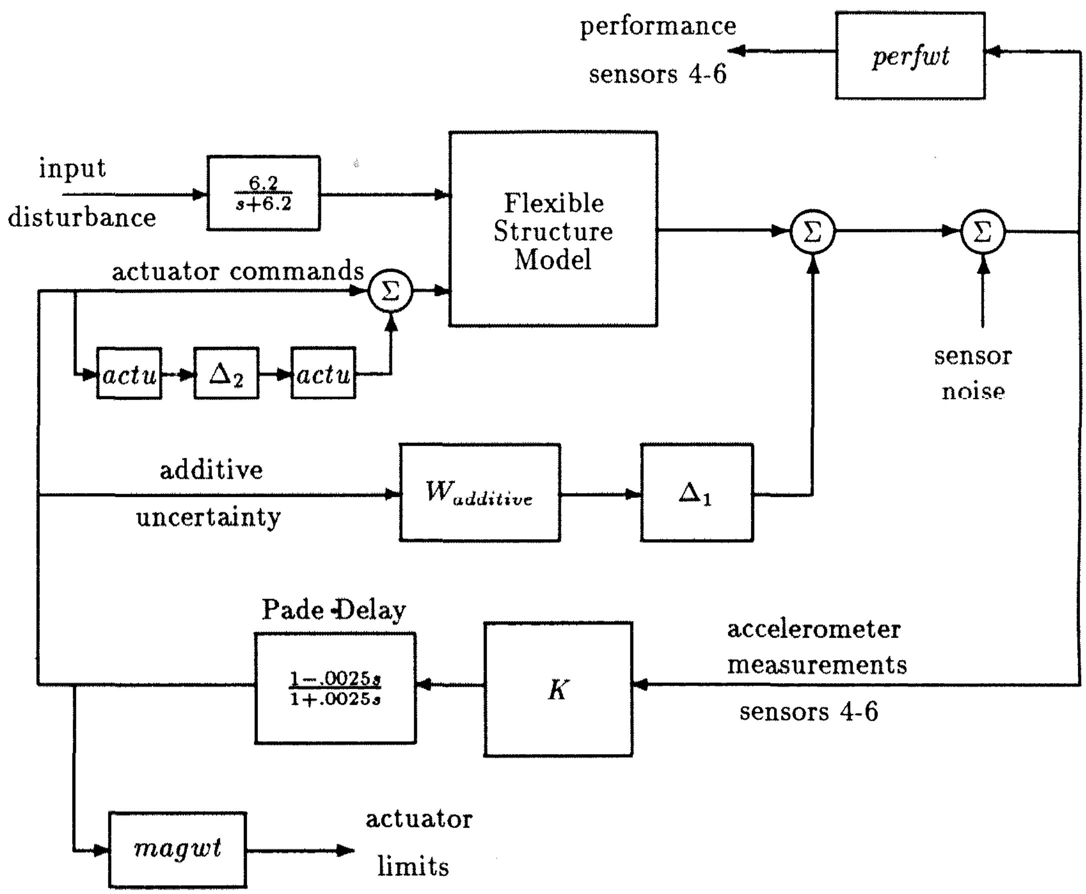

Figure 9.3: Block Diagram of the Noncollocated/Collocated Control Problem

9.3.2 Collocated

The resonant peaks of the transfer function between voice coil actuator 1 and sensors 4, 5, and 6, seen in figure 9.1, are initially scaled to one. A constant performance weight, *perfwt* in the block diagram, is used to select the desired vibration attenuation level. A sensor noise level of 2×10^{-3} is included in the design.

9.3.3 Control Designs

There are a limited number of weights used in the noncollocated and collocated control problem formulations. This is due to the nominal models, which include disturbance excitations, and have on the order of 35 states. The addition of the additive uncertainty weight, input disturbance filter, and performance weight, leads to the design model having approximately 50 states. The current status of the control design software restricts the current design model size to 60 states. A concern is that as the number of states in the problem formulation increases, the accuracy of the numerical solution decreases. This provides a reason to limit the states in the problem formulation. Numerical issues associated with the solution of Ricatti equations, frequency responses, and model reduction are problems restricting the application of μ-synthesis and H_∞ control design methods to large systems. A block diagram of the problem formulation is given in figure 9.3. This diagram is reformulated into the general LFT framework for the application of μ-synthesis techniques.

It is interesting to note that the response of the structure is very symmetric. An input signal into voice coil actuator 1 provides a similar response at sensors 2 and 3 on the second story, and at sensors 5 and 6 on the third structure (see Appendix B). The response at sensors 1 and 4 differ since the excitation is parallel to their sensing direction. The structure exhibits this same feature with the proof mass actuators as inputs. The proof mass actuators apply an inertia force to the structure at their third story locations. The local feedback loop around the proof mass actuators leads to the control law commanding displacement and the actuators applying inertia forces. Hence, they exert increased force as a function of frequency. The transfer function between the input command and collocated accelerometer response has an s^2 slope between 0.2 and 8

Hz corresponding to this fact. The experimental transfer functions between proof mass actuator 1 and sensors 4 and 5 are seen in figures 5.7 and 5.8.

The proof mass actuator local control loop is always turned on during the open-loop and closed-loop experiments. In the open-loop configuration, the local loops keep the moving mass centered. Experimental frequency responses are determined with the local loop on and off with the moving masses fixed to examine the effect of the proof mass actuator local feedback loops. Turning on the local feedback loops adds damping to the torsional modes of the structure as seen in figure 9.4. The local feedback loop increased damping levels by a factor of 2.5 on several of the torsional modes. A detriment in using the local proof mass control loops is that they increase the level of ambient disturbance above 7 Hz by a factor of 10. This is attributed to the stiction/friction in the proof mass actuators vibrating the structure.

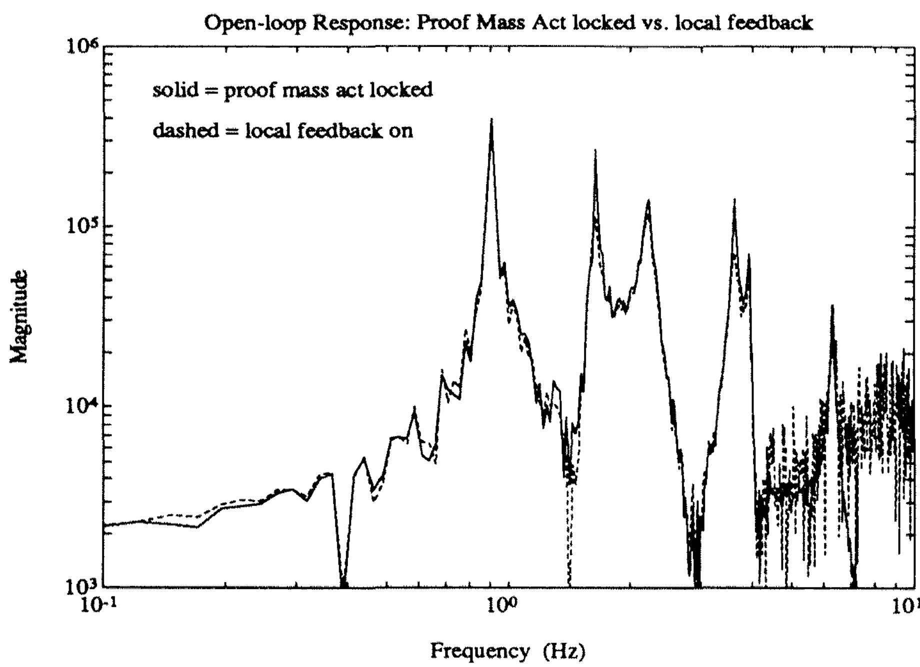

Figure 9.4: Open-loop Response of Sensor 4 with Proof Mass Actuators Locked versus Local Feedback

The behavior of the proof mass actuators limits performance of the control designs for both the collocated and noncollocated case. The proof mass actuators impart large forces at high frequency which translate into large accelerations of the collocated sensors. These accelerations are on the order of the response of the structure due to excitation of a flexible mode, shown in figure 9.2. The voice coil actuators are only able to substantially affect the flexible modes of the structure. Therefore, only minimal vibration attenuation is possible at frequencies that are not associated with flexible modes.

The achievable vibration attenuation using the proof mass actuators as control actuators is limited. The control authority of these actuators is hindered at low frequency by low force levels. The inertial force transmitted to the structure is a function of the moving mass and its acceleration. Acceleration is the second derivative of displacement, hence to achieve the same force at half the natural frequency, the moving mass requires four times the displacement. Given that the moving mass is approximately 0.35 kg (0.8 lb) and the maximum stroke is ± 1.0 in., the proof mass actuator generates 4×10^{-3} lb of force at the first natural frequency of the structure, 0.9 Hz. This is contrasted by the ability of the voice coil actuators to input up to 3 lb of force at this frequency.

The effects of stiction/friction are noticed in the response of the proof mass actuators despite the local feedback loop. The local feedback around the proof mass actuators does not completely eliminate the problems due to the stiction/friction. The output force of proof mass varies considerably above 5 Hz. This is a severe limitation when the proof mass actuators are used for control purposes. This is especially evident at the third torsional mode of the structure. The high frequency forces impacted to the structure from the proof mass actuators limit the performance of the collocated control laws.

9.4 Results

The noncollocated control design emphasized attenuating the response of the nine flexible modes of the phase II experiment between 0.9 and 6.3 Hz, and has minimal or no effect at other frequency points. One can infer from the singular value plot of the loop gain for control design $K5v$, figure 9.5, that the first and second bending and torsional modes will be heavily attenuated and the third bending and torsional modes will have little attenuation. From the μ plot in figure 9.6, the control design can not meet the performance or robustness specifications in the frequency range 3.2 to 20 Hz. Experimental results confirm these observations. Figures 9.7 and 9.8 are experimental transfer function plots of the open-loop and closed-loop system to sensors 4 and 6 with the noncollocated control law, $K5v$, implemented. The control design attenuates the resonance peaks of the first six flexible modes by at least a factor of 4. Above 5Hz, the input disturbance swamps the control authority of the voice coil actuators.

The performance objective is to minimize the acclerations are sensors 4, 5 and 6. The control laws employing the voice coil actuators achieves this by attenuating the vibration of the entire structure. This is seen by the attenuation of the frequency peaks at sensor 1 in figure 9.9. The only mode not attenuated is the third bending mode at 3.97 Hz, due to its small response at the third story sensors.

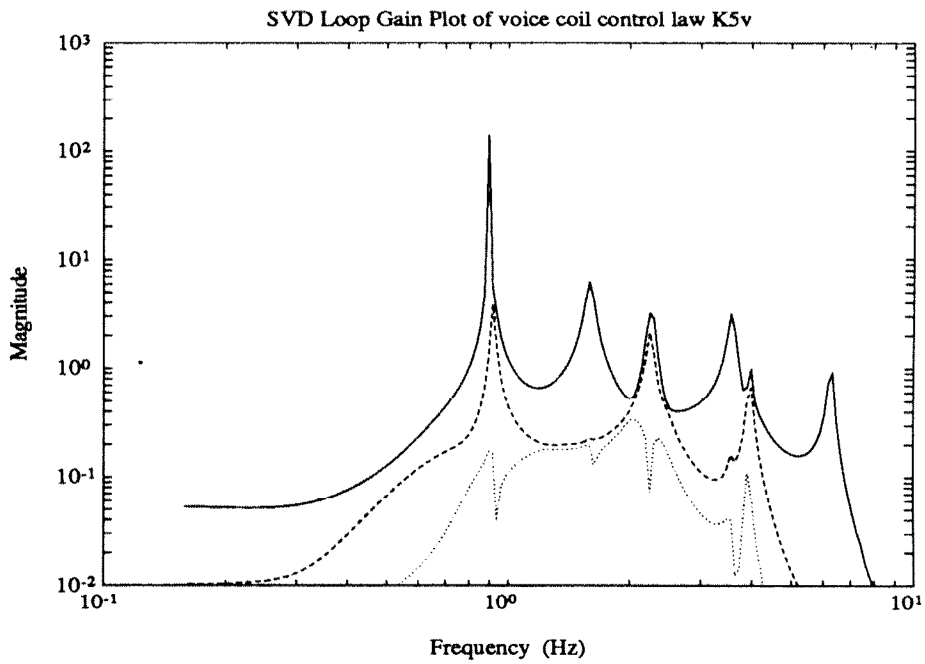

Figure 9.5: Singular Value Loop Gain Plot of Voice Coil Control Law K5v

The proof mass actuators are able to attenuate vibration of the torsional modes the best. This is expected because they exert force perpendicular to a lever arm from the center of the structure. Unfortunately, these actuators are of less assistance in attenuating vibration of the second and third bending modes. The proof mass actuators have little control authority over the response of these modes while the voice coil actuators have their largest influence on these modes.

This is analogous to the situation of a dog wagging his tail. The dog corresponds to the voice coil actuators and the tail is the third story of the structure. The proof

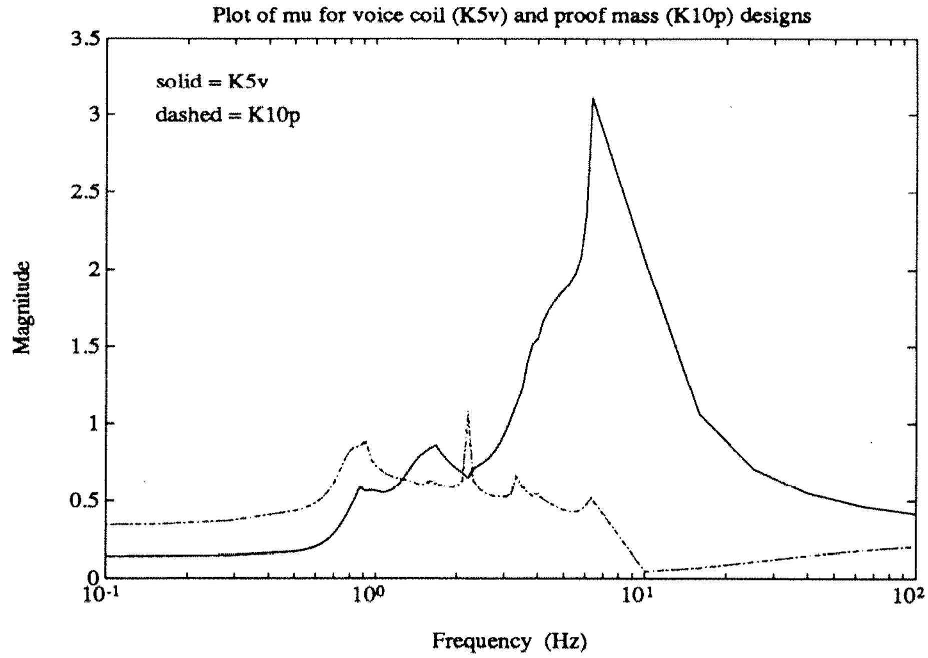

Figure 9.6: μ plot for Voice Coil Control Law (K5v) and Proof Mass Control Law (K10p) Designs

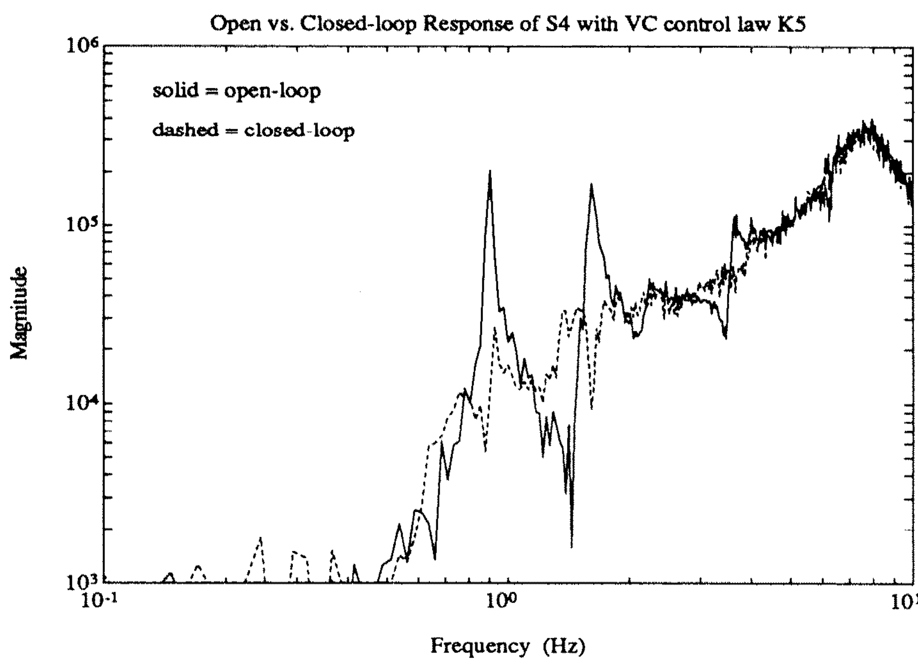

Figure 9.7: Open vs. Closed-loop Response of S4 with VC control law K5v

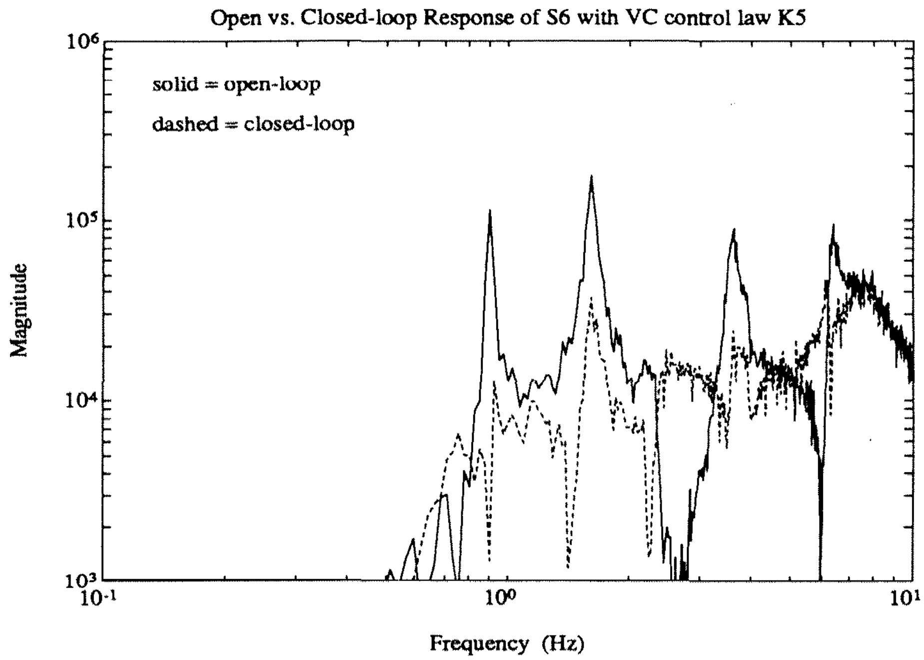

Figure 9.8: Open vs. Closed-loop Response of S6 with VC control law K5v

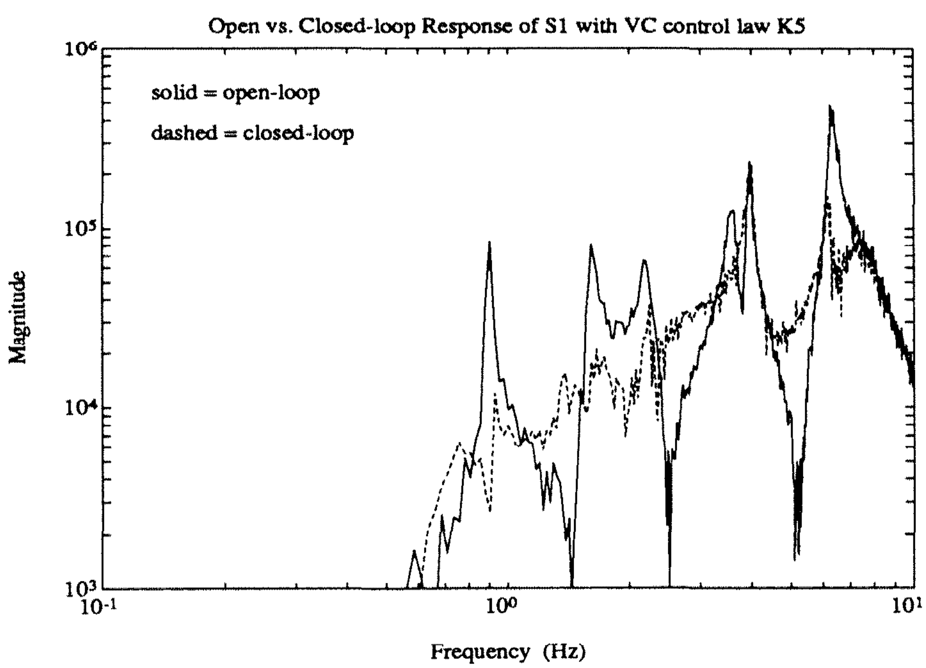

Figure 9.9: Open vs. Closed-loop Response of S1 with VC control law K5v

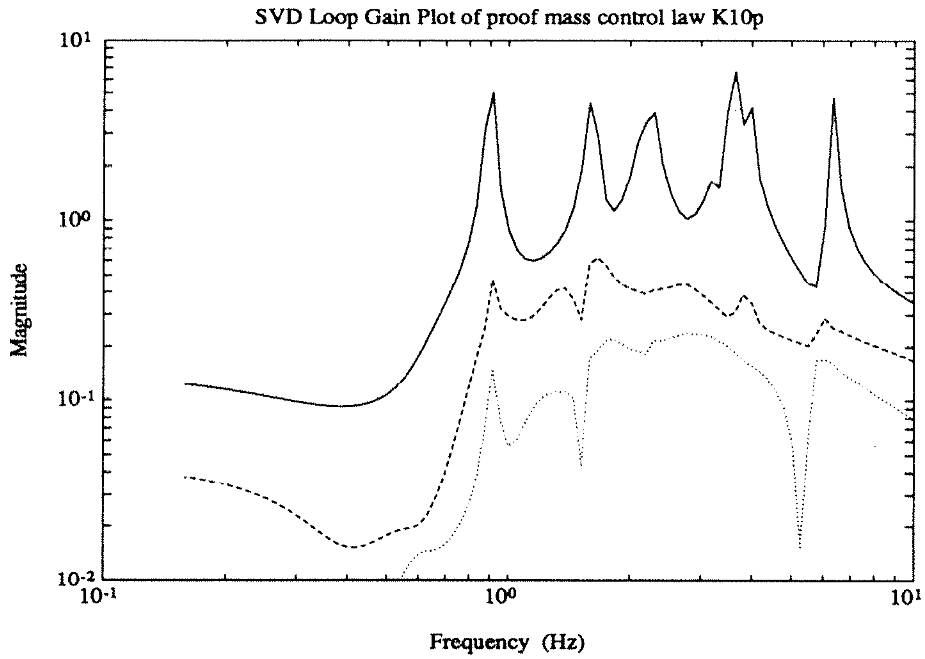

Figure 9.10: Singular Value Loop Gain Plot of Proof Mass Control Law K10p

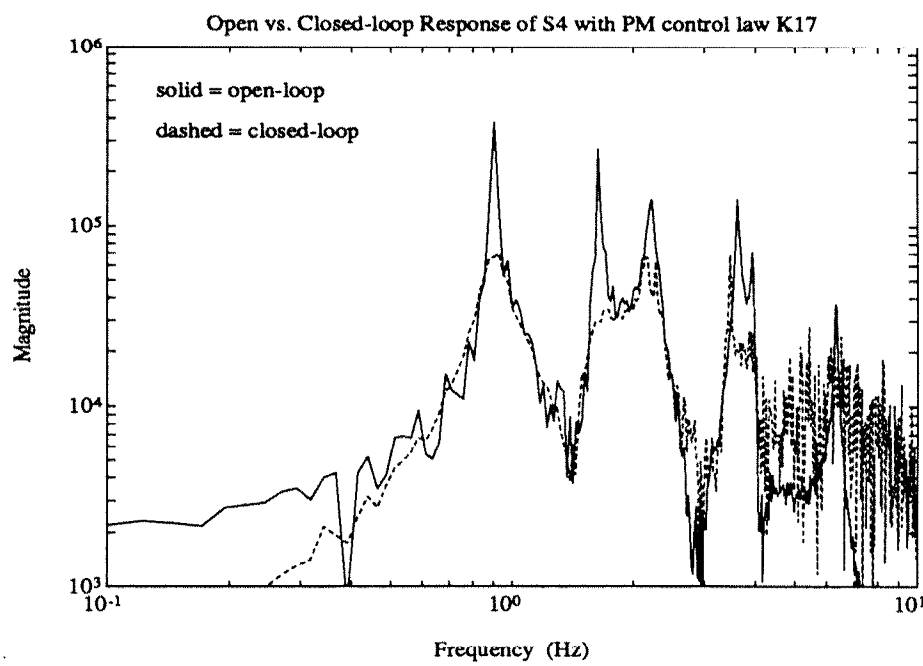

Figure 9.11: Open vs. Closed-loop Response of S4 with PM control law K10p

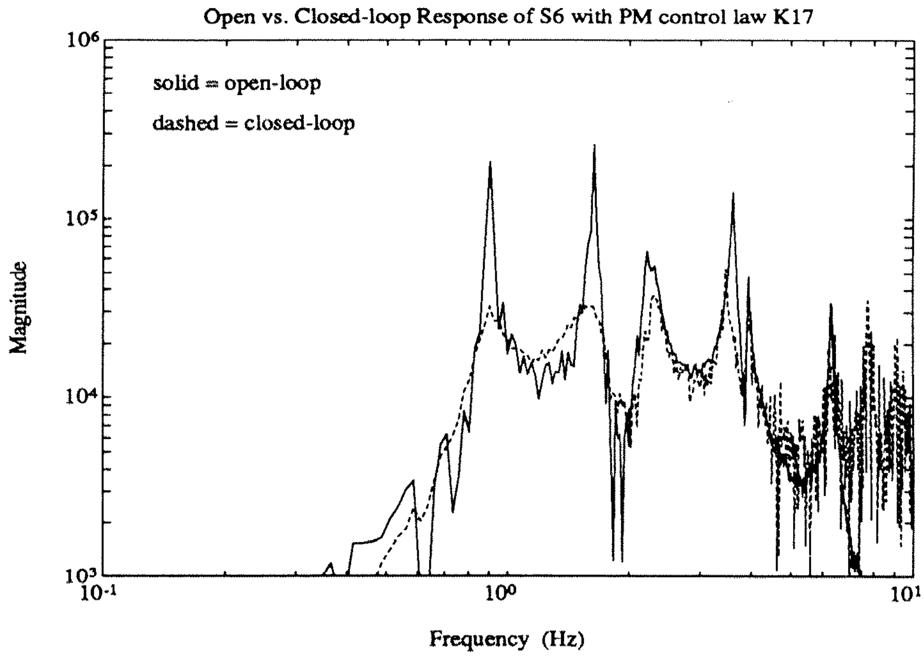

Figure 9.12: Open vs. Closed-loop Response of S6 with PM control law K10p

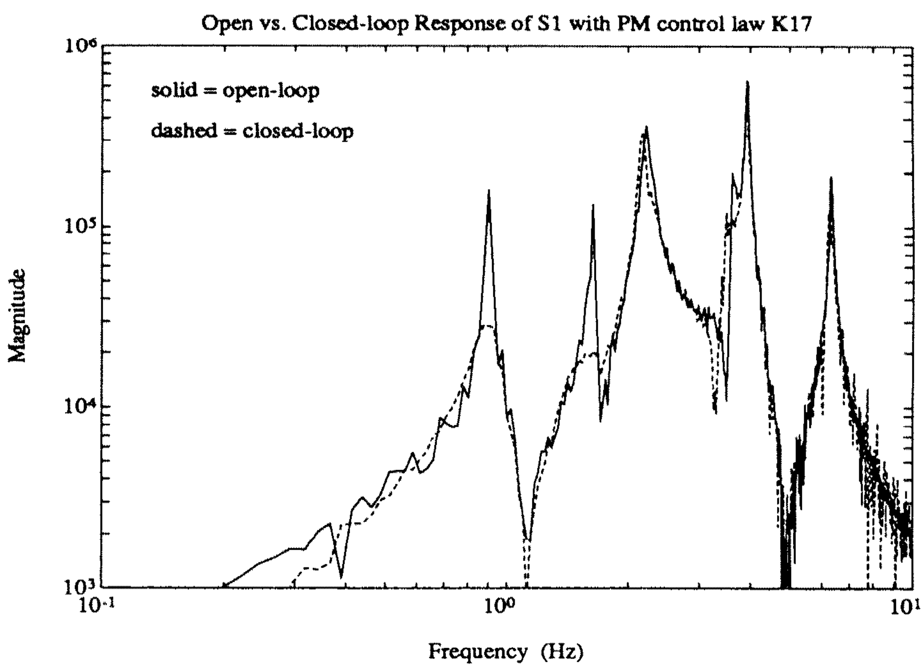

Figure 9.13: Open vs. Closed-loop Response of S1 with PM control law K10p

mass actuators would have to exert enough force to have the tail wag the dog. The stiction/friction of these actuators leads to high frequency forces exciting the structure. These three conditions are the underlying reason for the minimal attenuation of vibration that is achieved with collocated proof mass actuator/sensor pairs.

The performance objective is the same as in the noncollocated design. Notice that the proof mass actuator control laws attenuate vibration only at sensors 4, 5 and 6. Figure 9.13 is a comparison of the open-loop and closed-loop response of sensor 1 with control law $K17$. The first bending and torsional modes are heavily attenuated since their response is coupled to the response of sensors 4, 5 and 6. The higher modes exhibit the same level of response open-loop and closed-loop. Collocated control laws provide minimal vibration attenuation at other locations on the structure not coupled to the collocated sensors.

9.5 Conclusions

Clearly, the performance requirements and locations of the actuators and sensors will dictate the use of collocated or noncollocated control laws. The control engineer needs to understand the advantages and disadvantages of each approach to make an intelligent selection of control strategy. The results presented in this chapter provide insight into the benefits and limitations of each approach to vibration attenuation.

Chapter 10

Summary and Future Directions

Vibration attenuation in large space structures is a difficult control problem due to the stringent requirements on performance and inherent characteristics of such structures. The control design problem is compounded by the discrepancies between the structural model and the physical system. Control laws synthesized to attenuate vibration must be robust to the model error and at the same time achieve the performance objective, i.e., *robust performance.* Robust control design methods, specifically μ-synthesis techniques, are employed to address these issues in the control designs for flexible structures. μ synthesis techniques incorporate robustness and performance measures into a common framework and are ideally suited for the task at hand.

A flexible structure experiment is constructed to investigate control design issues associated with large space structures in the laboratory environment. The experiment has a number of attributes of flexible structures including: closely spaced, lightly damped modes, collocated and noncollocated sensors and actuators and numerous modes in the control crossover region. This research focused on the selection and incorporation of uncertainty descriptions of flexible structures into the control design process to account for model errors. Control designs for the phase I experimental structure highlight the inherent tradeoff between robustness and performance in the control design process. Accurate descriptions of the flexible structure <u>and</u> model errors lead to high performance control laws on the experimental structure. Robustness of the control laws is shown to be directly tied to the selection of uncertainty models. Inaccurate modeling of uncertainty leads to unstable control laws being synthesized for the experimental structure, in spite of an accurate structural model.

Uncertainty weights are used to design control laws that attenuate vibration in one frequency range while being robust-to-unmodeled, closely-spaced modes in the controller crossover region. One is able to achieve performance in one frequency range and be robust to unmodeled flexible modes at crossover. It is of interest to note that as more information about the structural model is included in the control problem formulation, less uncertainty is required to account for the model uncertainty as one would expect.

The benefits and limitations of collocated and noncollocated control for flexible structures is addressed in the last section of this thesis. Collocated control has the benefit of sensing and actuating at the same location that performance is desired. Pairing of the actuators and sensors provides robustness properties that are advantageous to control design. This feature makes them attractive for control of future space missions. This approach is constrained by the allowable locations of collocated actuator/sensor pairs and the control authority of the actuators. Sensor locations void of actuators often see little performance improvement with collocated control laws. Noncollocated control design incorporates sensor information at multiple locations to derive actuator commands used for control. An advantage of this approach is the control design senses exactly what is to be controlled. Noncollocated control design is limited by the response of the flexible structure. The frequency range in which performance is achievable is restricted by the dynamics of the structure. The control authority in the noncollocated design is limited at frequencies other than flexible modes. Results are presented to aid the designer in weighing the advantages and limitations of each method prior to selection of sensor and actuator locations.

This research shows the need of incorporating accurate descriptions of model error into the control problem formulation. The μ-synthesis design methodology proved very applicable to the vibration attenuation control problem in flexible structures. This is due to its ability to incorporate performance and robustness specifications into the control design process. Hopefully the results presented will aid and guide control engineers in the design of control laws using μ-synthesis methods.

Future directions for this research should include:

- Quantification of the role uncertainty plays in the design of high performance collocated and noncollocated control laws. A comparison is performed in this thesis for a specific model and design objective. It is important to understand how the accuracy of the design model and uncertainty descriptions affect the robustness and performance properties of both control laws. These results would aid system designers in the selection of actuator and sensor location on future large space structures.

- Development of systematic methods to identify both nominal models and uncertainty descriptions. Currently, uncertainty descriptions are developed based on the experience of the design engineer. A systematic approach to system identification, which provides both a plant and uncertainty model of the system, would be a major step forward in the control design process. An initial step in this process is model validation, which is determining whether a given model can produce the experimental data. Progress has been made in this area based on the robust control frameworks and hopefully can be expanded to include system identification [Smith].

- Generation of plant models and uncertainty descriptions based on first principle models. An initial model of a flexible structure is usually developed with finite element methods. The control designer is provided this model with little quantitative information as to its accuracy. The structural dynamicist often has information regarding his assumptions and variations in the model parameters which can be beneficial to the control design process. Currently there is no framework for the structural dynamicist to transfer his knowledge to the control engineer. This knowledge needs to be quantified in a common framework compatible with robust control methods.

- Inclusion of real parameter variations into the control design process. Variation in model parameters often takes the form of real perturbations, such as variations in mass and stiffness parameters. State of the art methods take them into account by modeling them as complex parameters. This leads to conservativeness in the control design. The ability to include real parameters in the synthesis process would provide a more physically based approach to control design. Controller synthesis with real parameters will likely improve the achievable performance of control designs.

The above suggestions are a first step in the unification of modeling, system identification, and robust control design. The μ-framework appears well suited for this unification process, with this thesis showing the applicability of μ-synthesis techniques to flexible structures, and Smith's model validation results showing the use of μ in system identification.

Appendices

A State Space Realization of Phase I Experimental Flexible Structure Model

A state space realization of the phase I flexible structure experiment is presented here. Continous time respresentations are of the form

$$P(s) = C(sT - A)^{-1}B + D = \left[\begin{array}{c|c} A & B \\ \hline C & D \end{array}\right] \tag{A.1}$$

The phase I model is given by

$$A = \begin{bmatrix} 0 & 1 & 0 & 0 & 0 & 0 & 0 & 0 & 0 & 0 & 0 & 0 \\ -55.3 & -0.21 & 0 & 0 & 0 & 0 & 0 & 0 & 0 & 0 & 0 & 0 \\ 0 & 0 & 0 & 1 & 0 & 0 & 0 & 0 & 0 & 0 & 0 & 0 \\ 0 & 0 & -55.6 & -0.21 & 0 & 0 & 0 & 0 & 0 & 0 & 0 & 0 \\ 0 & 0 & 0 & 0 & 0 & 1 & 0 & 0 & 0 & 0 & 0 & 0 \\ 0 & 0 & 0 & 0 & -201.8 & -0.33 & 0 & 0 & 0 & 0 & 0 & 0 \\ 0 & 0 & 0 & 0 & 0 & 0 & 0 & 1 & 0 & 0 & 0 & 0 \\ 0 & 0 & 0 & 0 & 0 & 0 & -298.5 & -0.70 & 0 & 0 & 0 & 0 \\ 0 & 0 & 0 & 0 & 0 & 0 & 0 & 0 & 0 & 1 & 0 & 0 \\ 0 & 0 & 0 & 0 & 0 & 0 & 0 & 0 & -304.8 & -0.62 & 0 & 0 \\ 0 & 0 & 0 & 0 & 0 & 0 & 0 & 0 & 0 & 0 & 0 & 1 \\ 0 & 0 & 0 & 0 & 0 & 0 & 0 & 0 & 0 & 0 & -781.0 & -0.60 \end{bmatrix} \tag{A.2}$$

$$B = \begin{bmatrix} 0 & 0 & 0 \\ 0.7789 & 0.4721 & 0.4129 \\ 0 & 0 & 0 \\ -0.4647 & 0.1403 & -0.8743 \\ 0 & 0 & 0 \\ 0.7011 & -0.5797 & -0.4153 \\ 0 & 0 & 0 \\ -0.8117 & -0.3012 & -0.5004 \\ 0 & 0 & 0 \\ -0.5116 & 0.1735 & -0.8415 \\ 0 & 0 & 0 \\ -0.5978 & 0.5462 & 0.5868 \end{bmatrix} \tag{A.3}$$

$$C^T = \begin{bmatrix} 31.684 & 0 & -22.694 \\ 0.121 & 0 & -0.086 \\ 0 & -37.004 & -35.019 \\ 0 & -0.139 & -0.131 \\ 147.652 & 40.353 & 9.087 \\ 0.240 & 0.066 & 0.015 \\ 204.794 & 0 & -152.208 \\ 0.480 & 0 & -0.357 \\ 0 & 205.404 & 240.756 \\ 0 & 0.415 & 0.487 \\ 535.533 & 125.663 & 32.248 \\ 0.415 & 0.097 & 0.025 \end{bmatrix} \tag{A.4}$$

$$D = \begin{bmatrix} 0.0080 & -0.0139 & 0.0086 \\ -0.0086 & 0.0045 & -0.0262 \\ 0.0099 & -0.0052 & 0.0225 \end{bmatrix} \tag{A.5}$$

B State Space Realization of Phase II Experimental Flexible Structure Model

A state space realization of the phase II flexible structure experiment is presented in the form

$$\begin{bmatrix} \dot{\eta} \\ \ddot{\eta} \end{bmatrix} = \begin{bmatrix} x_{real1} & x_{imag1} \\ x_{real2} & x_{imag2} \end{bmatrix} \begin{bmatrix} \eta \\ \dot{\eta} \end{bmatrix} + \begin{bmatrix} b_1 \\ b_2 \end{bmatrix} u \tag{B.1}$$

$$y = \begin{bmatrix} c_1 & c_2 \end{bmatrix} \begin{bmatrix} \eta \\ \dot{\eta} \end{bmatrix} + d_1 u \tag{B.2}$$

The phase II model from the voice coil actuators to sensors 4, 5, and 6 consists of 24 states, with the following frequencies and damping:

State	Real	Imaginary	Frequency (rad/s)	Damping
1	-3.5440E-02	5.6784E+00	5.6785E+00	6.2411E-03
2	-3.5440E-02	-5.6784E+00	5.6785E+00	6.2411E-03
3	-4.8754E-02	5.7685E+00	5.7687E+00	8.4515E-03
4	-4.8754E-02	-5.7685E+00	5.7687E+00	8.4515E-03
5	-4.7607E-02	5.7704E+00	5.7706E+00	8.2499E-03
6	-4.7607E-02	-5.7704E+00	5.7706E+00	8.2499E-03
7	-1.4205E-01	1.0176E+01	1.0177E+01	1.3958E-02
8	-1.4205E-01	-1.0176E+01	1.0177E+01	1.3958E-02
9	-2.3185E-01	1.3906E+01	1.3908E+01	1.6670E-02
10	-2.3185E-01	-1.3906E+01	1.3908E+01	1.6670E-02
11	-1.7091E-01	1.4169E+01	1.4170E+01	1.2061E-02
12	-1.7091E-01	-1.4169E+01	1.4170E+01	1.2061E-02
13	-1.7606E-01	1.4429E+01	1.4430E+01	1.2201E-02
14	-1.7606E-01	-1.4429E+01	1.4430E+01	1.2201E-02
15	-4.1703E-01	2.2594E+01	2.2598E+01	1.8455E-02
16	-4.1703E-01	-2.2594E+01	2.2598E+01	1.8455E-02
17	-1.8374E-01	2.4775E+01	2.4776E+01	7.4163E-03
18	-1.8374E-01	-2.4775E+01	2.4776E+01	7.4163E-03
19	-1.5997E-01	2.4933E+01	2.4934E+01	6.4159E-03
20	-1.5997E-01	-2.4933E+01	2.4934E+01	6.4159E-03
21	-3.7868E-01	3.9591E+01	3.9593E+01	9.5643E-03
22	-3.7868E-01	-3.9591E+01	3.9593E+01	9.5643E-03
23	-6.7448E-03	4.7078E+01	4.7078E+01	1.4327E-04
24	-6.7448E-03	-4.7078E+01	4.7078E+01	1.4327E-04

$$B = \begin{bmatrix} 1.062e+00 & -4.141e-03 & -2.927e-03 \\ -4.501e-01 & -9.927e-04 & 5.185e-04 \\ 8.218e-04 & -1.121e+00 & 5.595e-02 \\ 2.239e-03 & -2.179e-01 & -1.348e-01 \\ 3.040e-03 & -6.333e-02 & -1.079e+00 \\ 3.005e-03 & 1.429e-01 & 1.971e-01 \\ -4.801e-01 & 7.648e-01 & 6.316e-01 \\ 9.215e-01 & -1.132e+00 & -9.141e-01 \\ 2.098e+00 & -1.667e-02 & 1.638e-02 \\ -4.109e-01 & -9.156e-02 & 9.814e-03 \\ 1.258e-03 & 1.870e+00 & 2.308e-03 \\ -5.649e-02 & -8.126e-01 & -3.269e-02 \\ 1.220e-02 & 4.201e-02 & 1.131e+00 \\ -1.045e-02 & 2.749e-02 & -1.847e+00 \\ 2.085e+00 & -2.100e+00 & -2.081e+00 \\ -3.705e-01 & 5.774e-02 & 1.940e-01 \\ -1.520e+00 & -6.662e-01 & -3.443e-01 \\ -4.896e-01 & 1.659e-02 & -1.147e-01 \\ 1.007e-01 & -7.504e-02 & 5.180e-01 \\ -3.950e-02 & 7.069e-01 & -1.499e+00 \\ -1.273e+00 & 8.757e-01 & 1.111e+00 \\ -7.566e-01 & 1.134e+00 & 1.046e+00 \\ -1.340e-03 & 1.530e-01 & -1.362e-04 \\ -1.576e-03 & 2.003e-01 & -2.394e-03 \end{bmatrix} \tag{B.3}$$

$$C^T = \begin{bmatrix} -2.013e-01 & 1.177e-01 & 6.940e-02 \\ -4.463e-01 & 1.940e-01 & 2.378e-01 \\ 2.698e-03 & 9.414e-02 & -1.367e-01 \\ 2.173e-01 & -4.826e-01 & 2.080e-01 \\ 5.700e-02 & 1.023e-01 & -1.231e-01 \\ 2.456e-01 & 2.031e-01 & -4.517e-01 \\ 4.918e-01 & 5.147e-01 & 5.012e-01 \\ 2.767e-01 & 2.694e-01 & 3.643e-01 \\ 2.907e-01 & -2.058e-01 & -9.482e-02 \\ 8.351e-01 & -5.204e-01 & -5.049e-01 \\ 3.099e-01 & -5.475e-01 & -6.707e-03 \\ 3.373e-01 & -7.719e-01 & 2.468e-01 \\ 4.343e-01 & 4.212e-01 & -8.100e-01 \\ 1.821e-01 & 2.667e-01 & -3.168e-01 \\ 2.339e-01 & 1.965e-01 & 2.444e-01 \\ 1.056e+00 & 9.537e-01 & 1.054e+00 \\ -1.653e-03 & -7.765e-03 & 1.573e-02 \\ 6.484e-01 & -4.947e-01 & -3.357e-01 \\ -2.211e-01 & -5.923e-01 & 5.782e-01 \\ -1.263e-01 & -6.152e-02 & 1.744e-02 \\ -4.486e-01 & -3.610e-01 & -3.507e-01 \\ 6.177e-01 & 6.092e-01 & 6.596e-01 \\ 4.245e-02 & -2.653e-02 & -2.337e-03 \\ -1.082e-01 & -1.634e-02 & 3.740e-02 \end{bmatrix} \tag{B.4}$$

$$D = \begin{bmatrix} 1.301e-02 & 1.814e-02 & -9.123e-05 \\ -3.634e-03 & 8.714e-03 & -3.876e-03 \\ 9.150e-03 & -5.663e-03 & -2.274e-03 \end{bmatrix} \quad (B.5)$$

The phase II model from the proof mass actuators to sensors 4, 5, and 6 consists of 35 states, with the following frequencies and damping:

State	Real	Imaginary	Frequency (rad/s)	Damping
1	-4.2600E-02	5.6551E+00	5.6553E+00	7.5327E-03
2	-4.2600E-02	-5.6551E+00	5.6553E+00	7.5327E-03
3	-3.8547E-02	5.7819E+00	5.7820E+00	6.6667E-03
4	-3.8547E-02	-5.7819E+00	5.7820E+00	6.6667E-03
5	-3.0286E-02	5.8031E+00	5.8031E+00	5.2190E-03
6	-3.0286E-02	-5.8031E+00	5.8031E+00	5.2190E-03
7	-1.5639E-01	1.0147E+01	1.0148E+01	1.5411E-02
8	-1.5639E-01	-1.0147E+01	1.0148E+01	1.5411E-02
9	-1.6264E-01	1.0186E+01	1.0187E+01	1.5965E-02
10	-1.6264E-01	-1.0186E+01	1.0187E+01	1.5965E-02
11	-1.7250E-01	1.4295E+01	1.4296E+01	1.2066E-02
12	-1.7250E-01	-1.4295E+01	1.4296E+01	1.2066E-02
13	-1.7430E-01	1.4437E+01	1.4438E+01	1.2073E-02
14	-1.7430E-01	-1.4437E+01	1.4438E+01	1.2073E-02
15	-1.1716E-01	1.7532E+01	1.7532E+01	6.6825E-03
16	-1.1716E-01	-1.7532E+01	1.7532E+01	6.6825E-03
17	-1.0388E+00	2.2463E+01	2.2487E+01	4.6195E-02
18	-1.0388E+00	-2.2463E+01	2.2487E+01	4.6195E-02
19	-6.6576E-01	2.2515E+01	2.2525E+01	2.9556E-02
20	-6.6576E-01	-2.2515E+01	2.2525E+01	2.9556E-02
21	-5.9979E-01	2.2676E+01	2.2684E+01	2.6442E-02
22	-5.9979E-01	-2.2676E+01	2.2684E+01	2.6442E-02
23	-1.8732E+01	2.5350E+01	3.1520E+01	5.9429E-01
24	-1.8732E+01	-2.5350E+01	3.1520E+01	5.9429E-01
25	-1.3906E+01	3.3632E+01	3.6394E+01	3.8210E-01
26	-1.3906E+01	-3.3632E+01	3.6394E+01	3.8210E-01
27	-3.7904E+01	0.0000E+00	3.7904E+01	1.0000E+00
28	-5.9945E-01	3.9549E+01	3.9553E+01	1.5155E-02
29	-5.9945E-01	-3.9549E+01	3.9553E+01	1.5155E-02
30	-5.6856E-01	3.9582E+01	3.9586E+01	1.4362E-02
31	-5.6856E-01	-3.9582E+01	3.9586E+01	1.4362E-02
32	-6.6632E-01	3.9854E+01	3.9859E+01	1.6717E-02
33	-6.6632E-01	-3.9854E+01	3.9859E+01	1.6717E-02
34	-1.5277E+01	4.3715E+01	4.6307E+01	3.2990E-01
35	-1.5277E+01	-4.3715E+01	4.6307E+01	3.2990E-01

$$B = \begin{bmatrix} -1.209E+00 & 3.537E-03 & 2.872E-03 \\ -6.548E-02 & 2.155E-03 & -4.212E-03 \\ 7.491E-04 & -1.115E+00 & -1.927E-03 \\ 2.925E-03 & -4.310E-01 & 2.036E-03 \\ 5.462E-03 & -6.929E-03 & 8.100E-01 \\ -3.162E-03 & -1.149E-02 & 4.882E-01 \\ 6.873E-02 & 6.283E-01 & 6.228E-02 \\ -1.867E-01 & 1.989E+00 & 1.347E-01 \\ -1.482E+00 & 1.693E-01 & -8.110E-01 \\ -2.176E+00 & -5.448E-02 & -1.093E+00 \\ 1.406E+00 & -1.572E-01 & -2.548E-01 \\ 5.297E-01 & -4.173E-02 & 7.244E-03 \\ 8.657E-03 & 1.165E+00 & -3.076E-01 \\ -2.998E-02 & -4.144E-01 & 2.332E-01 \\ 4.618E-03 & 4.372E-01 & -4.092E-02 \\ 8.514E-03 & 8.977E-01 & -1.733E-02 \\ 5.541E-03 & -4.625E+00 & -3.050E-01 \\ 4.425E-01 & -2.521E+00 & -1.560E+00 \\ -1.773E-01 & -3.611E-01 & 4.109E-01 \\ 1.069E+00 & -9.463E-01 & -2.946E+00 \\ -4.584E+00 & -1.633E-01 & -1.416E+00 \\ -2.043E+00 & 4.474E-02 & -7.915E-01 \\ -3.357E-01 & -2.813E+01 & 2.073E-01 \\ -5.393E-02 & -1.913E+00 & -7.575E-01 \\ 1.184E-01 & 7.010E-02 & -1.316E+01 \\ -8.742E-03 & 1.129E-01 & 1.867E+01 \\ -2.767E+01 & -2.838E-01 & 2.817E-01 \\ 1.460E-01 & -8.595E-01 & -3.926E-02 \\ -2.309E-01 & -5.049E+00 & 1.697E-01 \\ -6.297E+00 & 1.635E-01 & 1.623E-02 \\ 1.803E+00 & 3.234E-01 & 1.370E-01 \\ -5.487E-02 & -9.912E-02 & 1.918E+00 \\ -5.609E-02 & -2.148E-02 & 3.130E+00 \\ 3.308E+01 & -9.320E-02 & 1.900E-01 \\ 3.596E+01 & -4.477E-02 & 1.921E-01 \end{bmatrix} \tag{B.6}$$

$$C^T = \begin{bmatrix} -6.164E-02 & 4.910E-03 & -1.189E-02 \\ 4.787E-01 & -2.542E-01 & -2.705E-01 \\ 7.885E-03 & -2.158E-01 & 4.774E-02 \\ -1.993E-01 & 5.047E-01 & -1.803E-01 \\ -1.791E-01 & -5.720E-02 & 1.292E-01 \\ 2.162E-01 & 1.997E-01 & -3.296E-01 \\ 4.929E-01 & 9.883E-01 & 3.583E-01 \\ -3.228E-01 & -4.317E-01 & 8.041E-03 \\ -7.262E-01 & -4.242E-01 & -5.690E-01 \\ 7.248E-01 & 6.529E-01 & 6.747E-01 \\ -2.379E-02 & 1.113E-01 & 3.881E-02 \\ -6.543E-01 & 8.341E-02 & 3.635E-01 \\ 1.047E-01 & -7.312E-02 & 2.641E-01 \\ -4.533E-02 & -4.975E-01 & 2.841E-01 \\ 4.321E-03 & 1.159E-01 & 2.102E-02 \\ -2.949E-02 & 4.784E-01 & 2.607E-02 \\ 7.942E-02 & -2.409E-01 & 4.834E-01 \\ 1.165E+00 & 2.177E+00 & 1.491E+00 \\ 1.568E-02 & -1.797E-01 & -8.008E-01 \\ -1.036E-02 & -7.998E-01 & -1.187E+00 \\ -1.204E-01 & 2.229E-01 & 2.197E-01 \\ 2.093E+00 & 1.354E+00 & 1.219E+00 \\ 1.778E+00 & 1.180E+01 & 2.402E+00 \\ -8.856E-01 & -3.272E+00 & -1.033E+00 \\ -7.974E-01 & -3.503E-01 & -2.306E+00 \\ -5.084E-01 & -1.137E+00 & -1.050E+01 \\ -1.774E+01 & -1.622E+00 & -3.294E-01 \\ 1.882E-01 & 8.870E-01 & 2.556E-01 \\ 1.194E+00 & 2.238E+00 & 1.367E+00 \\ 2.990E+00 & 1.269E+00 & 8.969E-01 \\ 5.809E-03 & -1.531E-01 & -2.329E-01 \\ -1.090E+00 & -9.280E-01 & -5.669E-01 \\ -9.081E-01 & -1.099E+00 & -1.673E+00 \\ -8.436E+00 & -2.591E-01 & -2.123E-01 \\ 1.627E+01 & 1.979E+00 & 1.099E+00 \end{bmatrix} \tag{B.7}$$

$$D = \begin{bmatrix} 1.109E+00 & 1.159E+00 & 5.816E-01 \\ -3.396E-01 & 8.298E+00 & 6.373E-01 \\ 1.195E-01 & 1.841E+00 & 5.960E+00 \end{bmatrix} \tag{B.8}$$

The following are experimental transfer function plots from voice coil actuator 2 to sensors 1, 2, 4, 5, and 6 and from proof mass actuator 2 to sensors 1, 2, 4, 5, and 6.

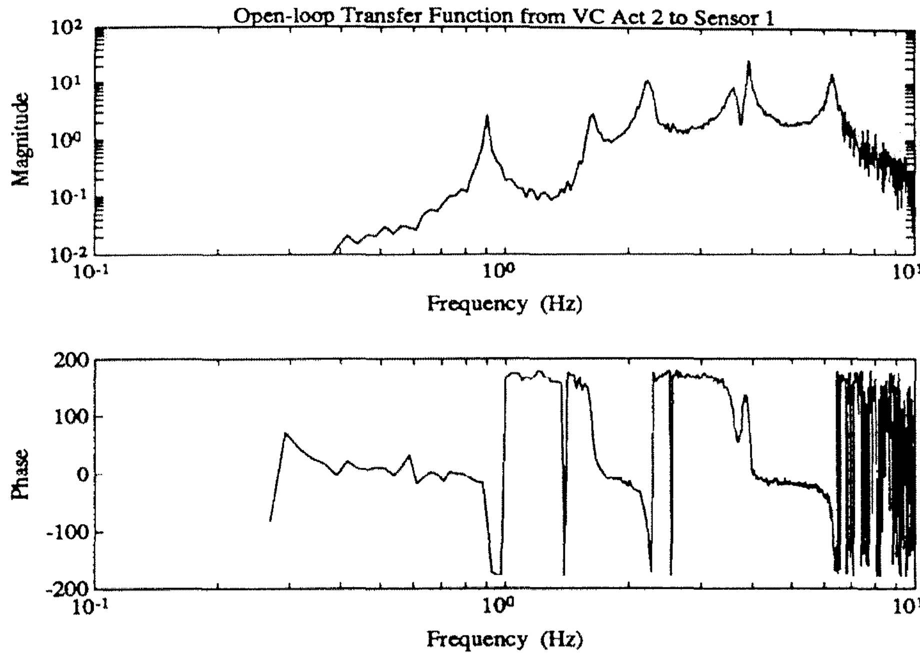

Figure B.1: Open-loop Frequency Response: Voice Coil Actuator 2 to Sensor 1

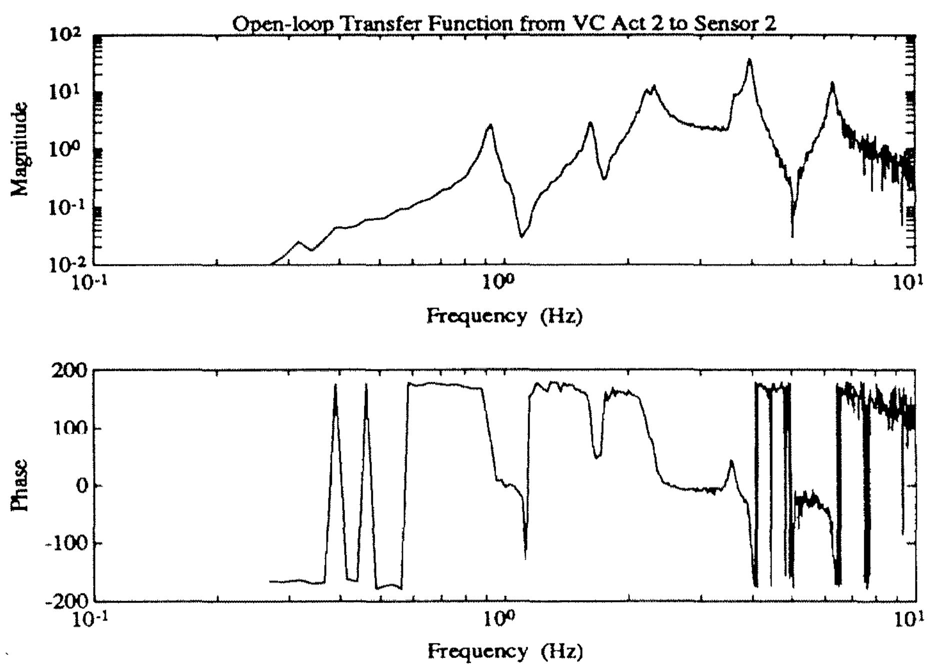

Figure B.2: Open-loop Frequency Response: Voice Coil Actuator 2 to Sensor 2

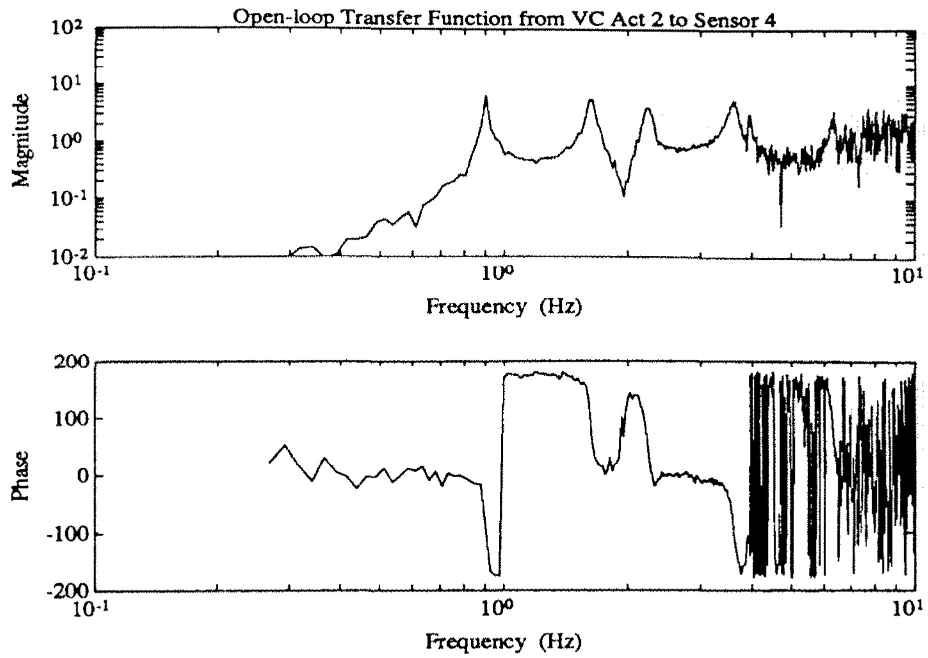

Figure B.3: Open-loop Frequency Response: Voice Coil Actuator 2 to Sensor 4

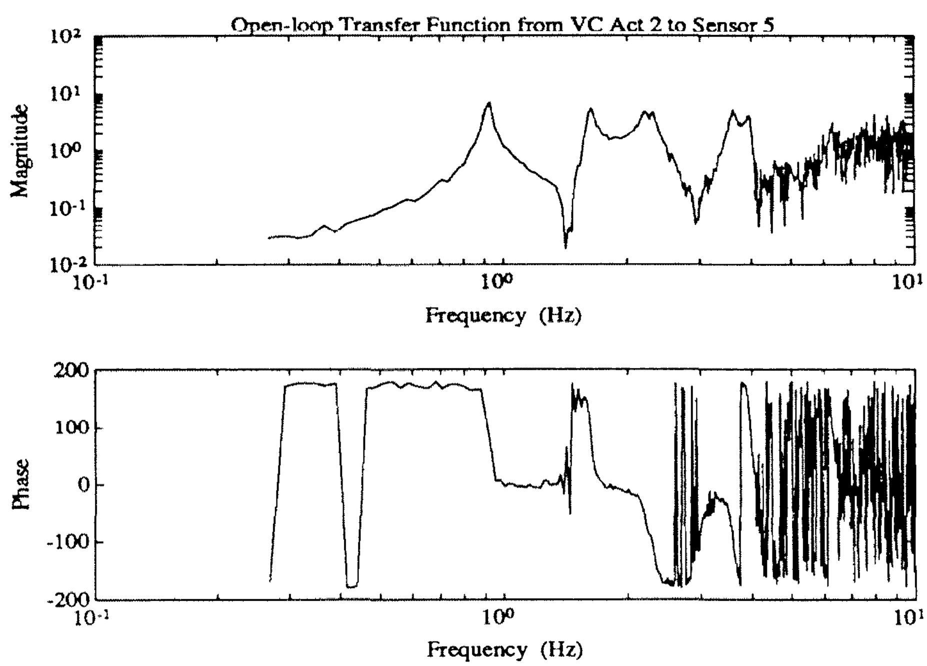

Figure B.4: Open-loop Frequency Response: Voice Coil Actuator 2 to Sensor 5

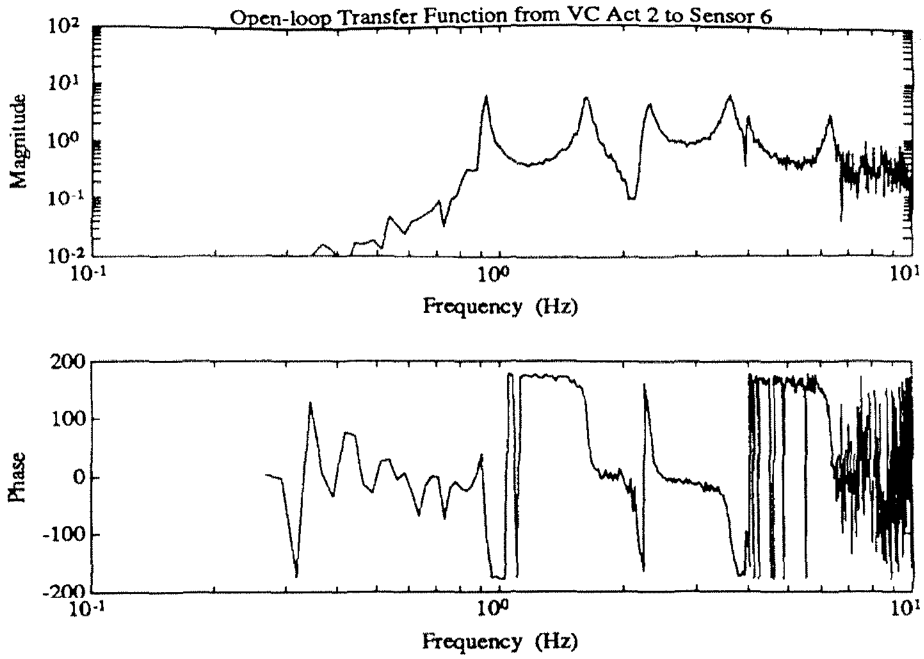

Figure B.5: Open-loop Frequency Response: Voice Coil Actuator 2 to Sensor 6

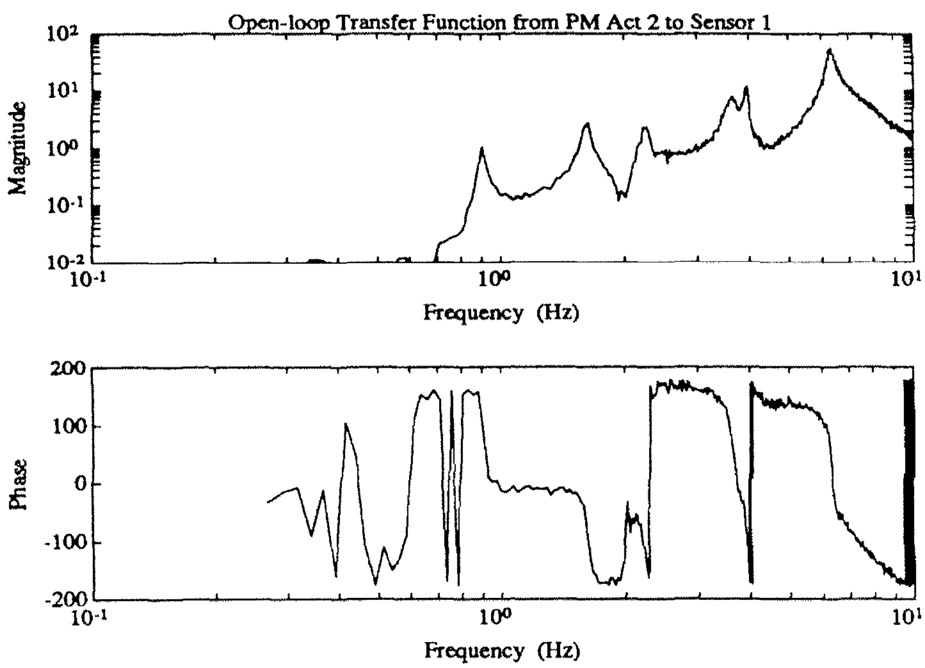

Figure B.6: Open-loop Frequency Response: Proof Mass Actuator 2 to Sensor 1

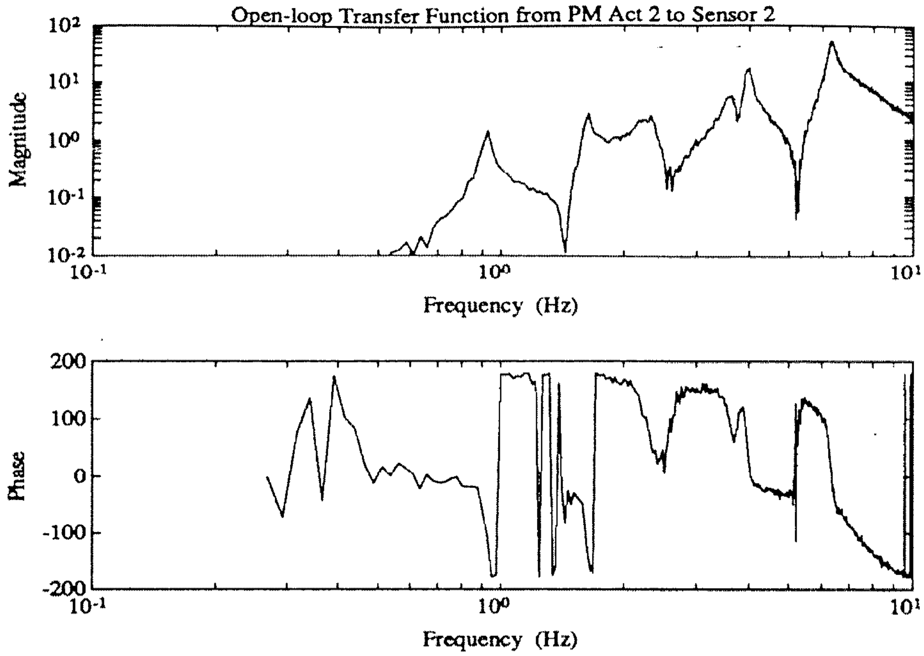

Figure B.7: Open-loop Frequency Response: Proof Mass Actuator 2 to Sensor 2

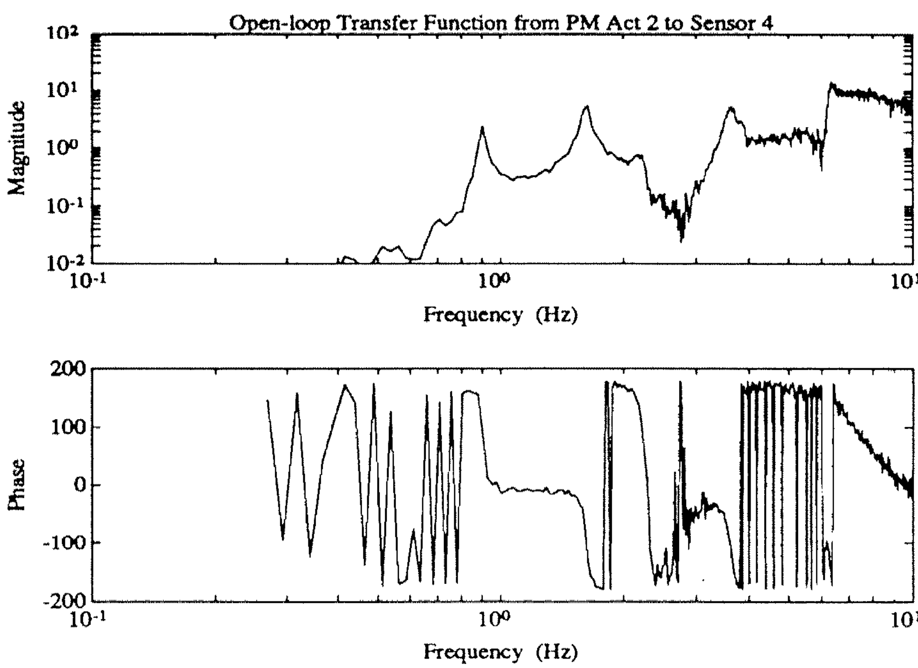

Figure B.8: Open-loop Frequency Response: Proof Mass Actuator 2 to Sensor 4

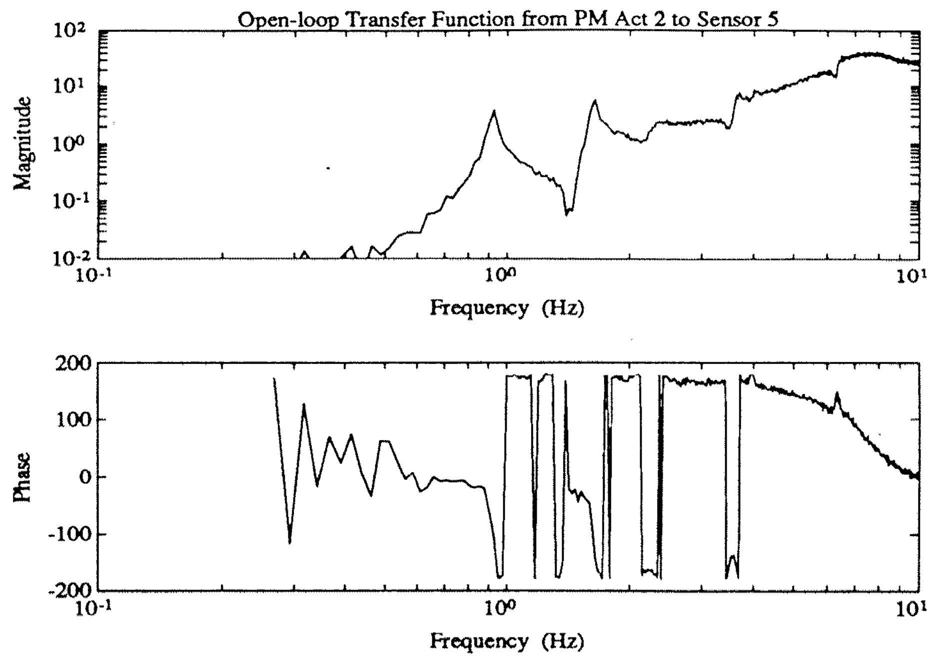

Figure B.9: Open-loop Frequency Response: Proof Mass Actuator 2 to Sensor 5

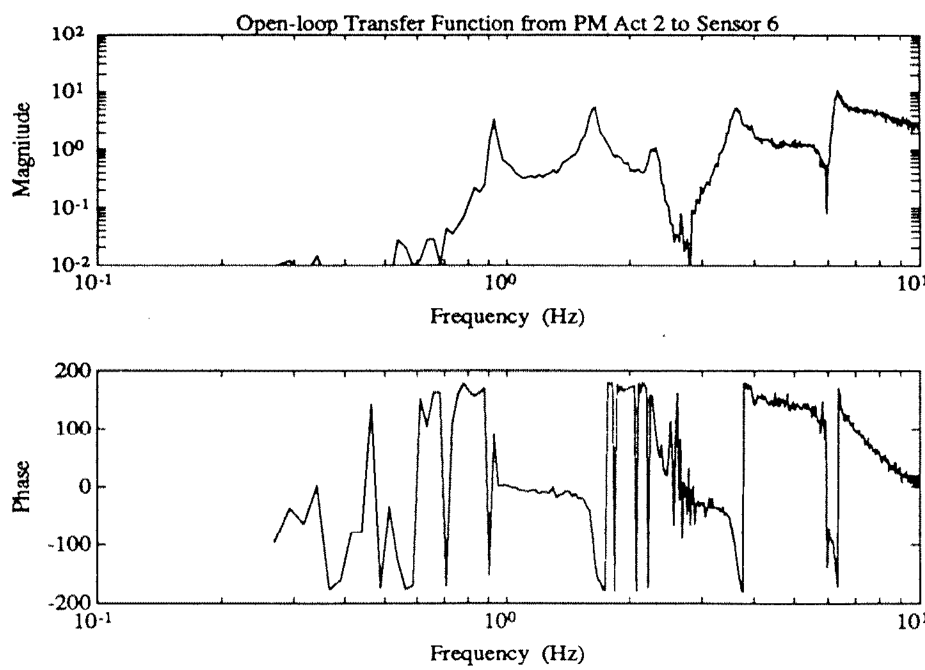

Figure B.10: Open-loop Frequency Response: Proof Mass Actuator 2 to Sensor 6

References

[Adcock] J.L. Adcock, "Curve fitter for pole-zero analysis," Hewlett-Packard Journal, January, 1987.

[BalChuD] G.J. Balas, C.C. Chu and J.C. Doyle, "Vibration Damping and Robust Control of the JPL/AFAL Experiment Using μ-Synthesis," Proceedings of 28^{th} Conference on Decision and Control, Ft. Lauderdale, FL, December, 1989.

[BalDoy1] G.J. Balas and J.C. Doyle, "On the Caltech experimental large space structure," American Control Conference (ACC), Atlanta, GA, June, 1988.

[BalDoy2] G.J. Balas and J.C. Doyle, "Identification for robust control of flexible structures," ACC, Pittsburgh, PA, June, 1989.

[BalDoy3] G.J. Balas and J.C. Doyle, "Robust Control of Flexible Modes in the Controller Crossover Region," ACC89, Pittsburgh, PA, 1989.

[BalLDD] G.J. Balas, M. Lukich, R.L. Dailey and J.C. Doyle, "Robust Control of a Truss Experiment," AIAA Guidance and Control Conference, Minneapolis, MN, August, 1988.

[BalMJ1] M.J. Balas, "Direct Output Feedback Control of Large Space Structures," Journal of Astronautical Sciences, Vol 27, No. 2, 1979 pp 157-180.

[BalMJ2] M.J. Balas, " Feedback Control of Flexible Systems," IEEE Transaction on Automatic Control, Vol. AC-23, No. 4, 1978, pp 673-679.

[CanRos] R.H. Cannon and D.E. Rosenthal, "Experiments in Control of Flexible Structures with Noncolocated Sensors and Actuators," Journal of Guidance, Control and Dynamics, Vol. 7, No. 5, Sept-Oct, 1984, pp 546-553.

[DailLuk1] R.L. Dailey and M.S. Lukich, "Recent Results in Identification and Control of a Flexible Structure," 1988 ACC, Atlanta, GA, pp 1468-1473.

[DailLuk2] R.L. Dailey and M.S. Lukich, "MIMO transfer function curve fitting using Chebyshev polynomials," SIAM 35^{th} Anniv. Meeting, Denver, CO, 1987.

[DesAbel] C.S. Desai and J.F. Abel, *Introduction to the Finite Element Method: A Numerical Method for Engineering Analysis,* Van Norstrand Reinhold Company, 1972.

[DGKF] J.C. Doyle, K. Glover, P. Khargonekar and B.A. Francis, "State-space solutions to standard H_2 and H_∞ control problems," IEEE Transactions on Automatic Control, Vol. 34, No. 8, August, 1989, pp 831-847.

[Doy1] J.C. Doyle, "Analysis of feedback systems with structured uncertainties," Proc. IEE-D 129, 1982, pp 242-250.

[Doy2] J.C. Doyle, *Lecture notes on advances in multivariable control,* ONR/Honeywell Workshop on Advances in Multivariable Control, Minneapolis, MN, October, 1984.

[DoyChu1] J.C .Doyle and C.C. Chu, "Robust control of multivariable and large scale systems," Final Technical Report for AFOSR, Contract No. F49620-84-C-0088, March, 1986.

[DoySt] J.C. Doyle and G. Stein, "Multivariable Feedback Design: Concepts for a Classical/Modern Synthesis," IEEE Transactions on Automatic Control, Vol AC-26, February, 1981, pp 4-16.

[DoyWSt] J.C. Doyle, J. Wall and G. Stein, "Performance and robustness analysis for structured uncertainty," Proceedings of 21^{st} Conference on Decision and Control, December, 1982.

[Enns] D. Enns, "Model reduction for control system design," Ph.D. dissertation, Stanford University, 1984.

[Francis] B.A. Francis, *A Course in H_∞ Control Theory*, Springer-Verlag, Berlin, 1987.

[Glov1] K. Glover, "All optimal Hankel norm approximations of linear multivariable systems and their L_∞ error bounds," Int. Journal of Control, 39, No. 6, 1984, pp 1115-1193.

[GlovDoy1] K. Glover and J.C. Doyle, "State-space formulae for all stabilizing controllers that satisfy an H_∞-norm bound and relations to risk sensitivity," Systems & Control Letters 11, 1989, pp 167-172.

[GlovDoy2] K. Glover and J.C. Doyle, "A state-space approach to H_∞ optimal control," to appear in Systems & Control Letters.

[HornJ] R.A. Horn and C.A. Johnson, *Matrix Analysis*, Cambridge Press, 1985.

[JuangLJ] J.N Juang, K.B. Lim and J.L. Junkins, "Robust Eigensystem Assignment for Flexible Structures," Journal of Guidance, Control and Dynamics, Vol. 12, No. 3, May-June, 1989, pp 381-387.

[KosSE] R.L. Kosut, H. Salzwedel and A, Emami-Naeini, "Robust Control of Flexible Spacecraft," Journal of Guidance, Control and Dynamics, Vol. 9, No. 2, March-April, 1983, pp 104-111.

[LinHK] J.G Lin, Y.H. Hegg and J.E. Keat, "Output Feedback Control for LSS: An Investigation of Four Design Methods," Dynamics and Control of Large Flexible Structures Proceedings of the First VPI & SU/AIAA Symposium, 1977.

[LukTu] M.S. Lukich and F.C. Tung, "Experimental Verification of Control and System Identification Techniques for a Flexible Truss Structure," ACC, Seattle, WA, July, 1986.

[Moore] B.C. Moore, "Principal components analysis in linear systems: controllability, observability and model reduction," IEEE Proceedings on Automatic Control, Vol. AC-26, February, 1981, pp 17-31.

[MorMcA] B. Morton and B. McAfoos, "A Mu-Test for Robustness Analysis of a Real Parameter Variation Problem," ACC85, Boston, June, 1985.

[MorZaf] M. Morari and E. Zafiriou, *Robust Process Control*, Prentice-Hall, N.J., 1989.

[NurRSS] G.S. Nurre, R.S. Ryan, H.N. Scofield and J.L. Sims, "Dynamics and Control of Large Space Structures," Journal of Guidance, Control and Dynamics, Vol. 7, No. 5, Sept-Oct 1984, pp 514-526.

[OppSch] A. Oppenheim and R.W. Schafer, *Digital Signal Processing*, Prentice-Hall, N.J., 1975.

[Pack] A.K. Packard, "What's new with μ: structured uncertainty in multivariable control," Ph.D. Thesis, University of California at Berkeley, 1988.

[PackFanDoy] A. Packard, M.K.H. Fan and J.C. Doyle, "A power method for the structured singular value," Proceedings of 27^{th} Conference on Decision and Control, December, 1988.

[SafChF] M.G. Safanov, R.Y. Chiang and H. Flashner, "H_∞ robust control synthesis for a large space structure," ACC88, Minneapolis, MN, June, 1988, pp 2038-2045.

[Sideris] A. Sideris, "H_∞ Optimal Control as a Weighted Wiener-Hopf Problem," submitted to IEEE Transactions on Automatic Control, September, 1987.

[Smith] R.S. Smith, "Model Validation for Uncertain Systems," Phd Dissertation, California Institute of Technology, Sept., 1989.

[SobelL] K.M Sobel and F.J. Lallman, "Eigenstructure Assignment for the Control of Highly Augmented Aircraft," Journal of Guidance, Control and Dynamics, Vol. 12, No. 3, May-June, 1989, pp 318-324.

[SteinG] G. Stein and C. Greene, "Inherent Damping, Solvability Conditions and Solutions for Structural Vibration Control," Honeywell Systems and Research Report, 1980.

[Stout] D.F. Stout, *Handbook of Operational Amplifiers Circuit Design*, McGraw-Hill, N.Y., 1976.

[SunJA] N. Sundararajan, S.M Joshi and E.S. Armstrong, "Robust Controller Synthesis for a Large Flexible Space Antenna," Journal of Guidance, Control and Dynamics, Vol. 10, No. 2, March-April, 1987, pp 201-208.

[Wonham] W.M. Wonham, "On Pole Assignment in Multiinput Controllable Linear Systems," IEEE Transactions on Automatic Control, Vol. AC-12, 1967, pp 660-665.

[YuanSt] J.S.-C. Yuan and M.E. Stieber, "Robust Beam-Pointing and Attitude Control of a Flexible Spacecraft," Journal of Guidance, Control and Dynamics, Vol. 9, No. 2, March-April, 1986, pp 228-234.

[Zames] G. Zames, "Feedback and optimal sensitivity: model reference transformations, multiplicative seminorms and approximate inverses," IEEE Trans Auto Control, Vol 26, April, 1981, pp 301-320.

[Zien] O.C. Zienkiewicz, *The Finite Element Method*, Third Edition, McGraw-Hill, London, 1977.